

Deformation Mechanisms of Bulk Metallic Glass Matrix Composites

Thesis by
Seung-Yub Lee

In Partial Fulfillment of the Requirements
for the Degree of
Doctor of Philosophy

California Institute of Technology
Pasadena, California
2005
(Defended March 30, 2005)

© 2005

Seung-Yub Lee

All Rights Reserved

To my late grandmother

ACKNOWLEDGEMENTS

Were it not for God's guidance, I would never have been able to stand on such a noble academic stage. The more I learn about the real world, the more I realize the real truth, it was only God's grace that brought me to this point in my life.

Reflecting on the time I spent at Caltech, my appreciation goes first to Dr. Üstündag, my academic advisor, who taught me all about performing good research. Not only was he my academic counselor, but a wonderful consultant on any subject I was concerned about. Sometimes, he had greater expectations of me than my actual ability warranted, but he was never disappointed in me and always encouraged me to move forward little by little. I would like to express my greatest appreciation to him for all of the time we spent together.

I was also very lucky to have such a bright scientist, Dr. Johnson, as my co-advisor. He provided me with a lot of physical insights and guided me in the direction of precisely where I should have been headed. It was a very valuable experience to have been able to discuss random topics with Dr. Johnson, many of which eventually led to deep scientific thought.

I am also grateful to Haein Choi-Yim and Paul Kim at Caltech. Not only did they provide the basis for my research, but also gave valuable advice. Jon Almer and Ulrich Lienert of the APS were very helpful in synchrotron X-ray diffraction experiments, and Bjørn Clausen at the Los Alamos National Laboratory helped to collect neutron diffraction data. I would especially like to give Bjørn special thanks due to his excellent work in finite element and self-consistent modeling.

I would also like to extend my thanks to Boonrat Lohwongwatana and Donghua Xu who came to Caltech at about the same time I did. I really enjoyed our friendship that we built together for more than four years.

Last, but not least, I want to express my love to my fiancée, Youngshin Kim. For the past year during what was the most important stage of my research, she gave me much comfort and joy. Her support allowed me to efficiently focus on what I had to do. Without her encouragement and affection, it would have been so much more difficult to reach this point in my academic career.

This research was supported by the National Science Foundation (MRSEC program, DMR-0080065 and CAREER Award DMR-9985264)

ABSTRACT

Bulk metallic glasses (BMGs) possess a unique set of mechanical properties that make them attractive structural materials: yield strength > 2 GPa, fracture toughness ~ 20 MPa.m^{1/2} and elastic strain limit $\sim 2\%$. BMGs can also be cast into intricate shapes which retain their dimensional integrity and require no further machining. Unfortunately, monolithic BMGs fail catastrophically under unconstrained loading by forming shear bands. To overcome this problem, BMG matrix composites with fiber and dendritic reinforcements were proposed. The former type includes metallic fibers of Ta, Mo and stainless steel. The latter composites develop precipitates during casting and are thus called *in-situ* composites. Here, the reinforcements form an interpenetrating dendritic structure and enhance the ductility of the composite.

This study investigated the deformation behavior of these two types of BMG composites. Loading measurements were performed during neutron or high-energy X-ray diffraction to determine lattice strains in the crystalline reinforcements. The diffraction data were then combined with finite element and self-consistent modeling to deduce the behavior of the amorphous matrix, as well as to understand the effective deformation mechanisms in the composite.

The deformation of the wire composites was studied using an integrated neutron diffraction and finite element (FE) approach. The FE model yielded a reasonable version of *in-situ* stress-strain plots for both reinforcements and the matrix. It was found that the reinforcements yielded first and started transferring load to the matrix which remained

elastic throughout the whole loading experiment. The reinforcements were seen to possess yield strengths lower than their monolithic forms, likely due to annealing during processing. After optimizing material properties to fit experimental data, the FE model developed was reasonably successful in describing both the macroscopic composite deformation and the lattice strain evolution in the reinforcements.

In the case of the *in-situ* composites, a detailed neutron and high energy X-ray diffraction study was conducted combined with a self-consistent deformation model. The compressive behavior of the composite and the second phase (in its monolithic form) were investigated. It was shown that the ductile second phase yields first upon loading the composite followed by multiple shear band formation in the BMG matrix, a process which enhances the ductility of the composite. It was also discovered that the mechanical properties of the reinforcements, and indirectly the composite, are highly variable and quite sensitive to processing conditions. This resulted from the unstable nature of the BCC β phase reinforcements which tend to transform into an ordered phase leading to significant stiffening, but also loss of ductility. An additional heat treatment study confirmed this phase evolution.

The overall conclusion of this study is that BMG composites with high ductility require reinforcements that yield first and induce multiple shear bands in the amorphous matrix, which in turn enhances the latter's ductility. To also retain a high yield point, the reinforcements need to be stiff. These two properties can best be optimized in β phase composites via a judicious combination of microstructure control and heat treatment.

TABLE OF CONTENTS

| | |
|--|-----------|
| ACKNOWLEDGEMENTS | iv |
| ABSTRACT | vi |
| TABLE OF CONTENTS | viii |
| LIST OF FIGURES | xi |
| LIST OF TABLES | xix |
| | |
| CHAPTER 1 INTRODUCTION | 1 |
| 1.1 Metallic Glasses | 1 |
| 1.2 Metallic Glass Composites | 5 |
| 1.3 Overview of the Thesis | 9 |
| References | 11 |
| | |
| CHAPTER 2 EXPERIMENTAL PROCEDURES | 13 |
| 2.1 Synthesis of Metallic Glass Matrix Composites | 13 |
| 2.1.1 Wire Composites | 13 |
| 2.1.2 <i>In-situ</i> Composites | 14 |
| 2.2 Mechanical Tests and Microscopy | 15 |
| 2.2.1 Loading Tests | 15 |
| 2.2.2 Ultrasound Measurements of Elastic Constants | 15 |
| 2.2.3 SEM and Microprobe Analysis | 16 |
| 2.3 Neutron Diffraction of Wire and <i>In-situ</i> Composites | 17 |
| 2.3.1 Experimental Procedure | 17 |
| 2.3.2 Data Analysis | 18 |
| 2.4 Synchrotron X-ray Diffraction of <i>In-situ</i> Composites | 19 |
| 2.4.1 High Energy X-ray Diffraction Procedure | 19 |
| 2.4.2 Data Analysis | 21 |
| References | 22 |

| | |
|--|----|
| CHAPTER 3 RESULTS AND DISCUSSION: MECHANICAL | 23 |
| BEHAVIOR AND MODELING OF WIRE COMPOSITES | |
| 3.1 Compressive Loading of Wire Composites | 23 |
| 3.1.1 Macro Stress-Strain Behavior of Wire Composites | 26 |
| 3.1.2 Fracture Morphology | 28 |
| 3.1.3 Neutron Diffraction and Finite Element Modeling | 30 |
| 3.2 Tensile Loading of Wire Composites | 39 |
| 3.3 Conclusions | 41 |
| References | 43 |
| | |
| CHAPTER 4 RESULTS AND DISCUSSION: MECHANICAL | 44 |
| BEHAVIOR AND MODELING OF <i>IN-SITU</i> β PHASE | |
| COMPOSITES | |
| 4.1 <i>In-situ</i> Composite Development and Characterization | 44 |
| 4.1.1 Background: Development of LM2 <i>In-situ</i> Composites | 44 |
| 4.1.2 System Optimization and Physical Properties of LM2A2 <i>In-situ</i> Composites | 50 |
| 4.2 Tensile and Compressive Stress-Strain Behavior of LM2A2 Composites | 52 |
| 4.2.1 Tension Tests of Heat Treated LM2A2 | 52 |
| 4.2.2 Compression Tests of Heat Treated LM2A2 | 57 |
| 4.2.3 Ultrasonic Sound Velocity Measurement of Elastic Constants | 59 |
| 4.3 <i>In-situ</i> Loading Experiments | 61 |
| 4.3.1 Compressive Loading Behavior during Neutron Diffraction of As-cast Specimens | 61 |
| 4.3.1.1 Introduction | 61 |
| 4.3.1.2 Experimental Procedure | 62 |
| 4.3.1.3 Neutron Diffraction Data | 64 |
| 4.3.1.4 Lattice Strains and Elastic Anisotropy | 65 |
| 4.3.1.5 Self-Consistent Modeling of Plastic Deformation | 68 |
| 4.3.1.6 Texture Evolution in the β Phase | 74 |
| 4.3.1.7 Summary of the Deformation Mechanism in As-cast | 76 |

| | |
|---|-----|
| Composites | |
| 4.3.2 Tensile Loading Behavior of As-cast Specimens during Synchrotron X-ray Diffraction | 78 |
| 4.4 Effect of Heat Treatment on <i>In-situ</i> Composites | 79 |
| 4.5 Conclusions | 82 |
| References | 84 |
| CHAPTER 5 RESULTS AND DISCUSSION: MICROSTRUCTURE AND PHASE EVOLUTION OF <i>IN-SITU</i> β PHASE COMPOSITES | 87 |
| 5.1 Microstructure of <i>In-situ</i> β Phase Composites | 87 |
| 5.1.1 Microstructure of Wedge-Shaped LM2A2 | 89 |
| 5.1.2 Microstructure of Arc-Melted LM2A2 | 93 |
| 5.1.3 Yield Strength vs. Dendrite Size | 98 |
| 5.2 Phase Evolution of <i>In-situ</i> β Phase Composites | 100 |
| 5.2.1 LM2 Composite Phase Evolution | 101 |
| 5.2.2 <i>In-situ</i> Cyclic Heating Experiment of LM2A2 | 104 |
| 5.2.3 Isothermal Heat Treatment of LM2A2 | 106 |
| 5.3 Pseudo Binary Phase Diagram for <i>In-situ</i> β Phase Composites | 116 |
| 5.4 Conclusions | 122 |
| References | 124 |
| CHAPTER 6 SUMMARY AND FUTURE WORK | 127 |
| APPENDIX A | |
| Applied Stress vs. Elastic Strain of Fiber Composites from Neutron Diffraction | 131 |
| APPENDIX B | |
| Validity of Calculating Three-Dimensional Phase Volume Fraction from a Two- Dimensional SEM Image | 135 |
| APPENDIX C | |
| Finite Element Modeling of Heat Transfer in an Arc-melted Button | 138 |

LIST OF FIGURES

| | | |
|----------|---|----|
| Fig. 1.1 | Schematic diagram of volume change with respect to temperature as a liquid is cooled through the glass transition temperature, T_g . | 2 |
| Fig. 1.2 | Equilibrium viscosity as a function of temperature for the undercooled liquid of $Zr_{46.75}Ti_{8.25}Cu_{7.5}Ni_{10}Be_{27.5}$ “Vitreloy 4” alloy. | 2 |
| Fig. 1.3 | Heat capacity of $Zr_{41.2}Ti_{13.8}Cu_{12.5}Ni_{10}Be_{22.5}$ metallic glass as a function of temperature: the point of discontinuity of C_p is the glass transition temperature, T_g . | 3 |
| Fig. 1.4 | Stress strain curve of Vitreloy 106 BMG and some pure metals. All samples were melted and cooled in the arc melter. All pure metals show low yield strength and large ductility while BMG exhibits very high yield strength but no plasticity. | 5 |
| Fig. 1.5 | Compression and tension tests of various kinds of particulate composites. | 6 |
| Fig. 1.6 | Compression data of W wire reinforced Vitreloy 1 composites. (20 ~ 80%). | 8 |
| Fig. 1.7 | Compressive stress-strain curves of an <i>in-situ</i> β phase composite compared with those from a monolithic matrix and a monolithic β phase. M: Amorphous matrix; H: Composite made at Howmet; B: Monolithic β phase alloy. | 9 |
| Fig. 2.1 | Experimental setup and schematic diagram for the wire composite casting procedure. | 14 |
| Fig. 2.2 | SEM images of an 80% W wire composite (left) and an <i>in-situ</i> β composite. (Unlike Vit 1-W composites, there is no reaction layer between Vit 106 and W). | 15 |
| Fig. 2.3 | Schematic of sample geometry with respect to beam and loading direction. | 18 |
| Fig. 2.4 | Refined diffraction pattern of Mo (BCC) wire composites. (Top: Longitudinal, Bottom: Transverse). | 19 |
| Fig. 2.5 | APS <i>in-situ</i> tensile loading experimental setup in beam line 1-ID. The dotted lines represent synchrotron beams and the load cell frame is located in the middle. | 20 |

| | | |
|----------|---|----|
| Fig. 2.6 | A captured image of Cu mold casting β phase composite during FIT 2D analysis. | 21 |
| Fig. 3.1 | Macro stress-strain curves in uniaxial compression of Vit. 106 matrix, 80% wire reinforced composites. The tests were performed at Caltech by Instron 4204 with a cross head speed of 0.1 mm/min. | 27 |
| Fig. 3.2 | Fracture morphology of 80% wire composites in top and side view. Wire diameter is 0.25 mm. | 29 |
| Fig. 3.3 | Mesh used in the FEM calculations for a 40% fiber model. The light gray elements represent the fibers while the dark gray elements represent the matrix. The surfaces in the 1-2 planes (perpendicular to the fiber axis) are constrained to remain planar, effectively imposing a plane strain behavior. Loading is applied along direction 3. | 31 |
| Fig. 3.4 | <i>In-situ</i> stress-strain behavior for each phase as calculated by the finite element model. These plots were deduced by comparing the experimental data with model predictions. | 33 |
| Fig. 3.5 | Neutron (a) and macroscopic composite data (b) of the 40% Mo - Vit. 106 matrix composite compared with the predictions of the FEM model. | 36 |
| Fig. 3.6 | Neutron (a) and macroscopic composite data (b) of the 40% SS (type 302) - Vit. 106 matrix composite compared with the predictions of the FEM model. Two versions of the model are shown: the first version (“TRS”) includes thermal residual stresses while the second one assumes there are no thermal residual stresses (“no TRS”). | 37 |
| Fig. 3.7 | Neutron (a) and macroscopic composite data (b) of the 40% Ta - Vit. 106 matrix composite compared with the predictions of the FEM model. | 38 |
| Fig. 3.8 | Macro uniaxial tensile stress-strain curves for Mo and Ta 80% wire composites. | 40 |
| Fig. 3.9 | Fracture images of Mo and Ta 80% composites after the tension test. Fiber pull-out and necking are observed in Mo and Ta, respectively. | 41 |
| Fig. 4.1 | Ternary phase diagram that shows phase partitioning between | 45 |

crystalline and amorphous phases: C: composite made at Caltech; H: composite made at Howmet; M: amorphous matrix; B: BCC β phase.

- | | | |
|-----------|---|----|
| Fig. 4.2 | Microstructure of two <i>in-situ</i> β phase composites. (C: made at Caltech; H: made at Howmet). Bright spots are the BCC dendrite, while dark areas belong to the glassy matrix. Note that the magnification is the same in both micrographs, indicating a much finer dendrite size in the Howmet material which had been subjected to a higher cooling rate. | 45 |
| Fig. 4.3 | Tensile stress-strain curves of two <i>in-situ</i> composites compared to that of Vit. 1. C represents the composite made at Caltech, and H labels the composite made by the Howmet Corporation. The finer dendrite size in the latter composite leads to a higher yield strength. | 46 |
| Fig. 4.4 | Neutron diffraction data of monolithic β phase before and after CTE measurement up to 350°C. The Young's modulus jumps from 64 to 100 GPa while the material becomes brittle. The neutron diffraction patterns are shown in Fig. 5.9. | 49 |
| Fig. 4.5 | Compressive tests of LM2 (~8% total strain) and LM2A2 (~14% total strain) <i>in-situ</i> composites (courtesy of Liquid Metal Technology). | 50 |
| Fig. 4.6 | Tensile stress-strain plots of monolithic β phase heat treated at 300°C. | 52 |
| Fig. 4.7 | Tensile stress-strain plots of β phase composite heat treated at 300°C. | 52 |
| Fig. 4.8 | Tensile sample geometry and fracture image of an as-cast β phase composite after necking in the middle of sample. | 54 |
| Fig. 4.9 | Successive SEM images taken from the same region of the tensile test sample shown in Fig. 4.8. Shear bands are visible as dark lines. | 55 |
| Fig. 4.10 | Surface displacement field in the deformed β phase composite shown in Fig. 4.9 obtained from digital image processing (in collaboration with Rockwell Scientific). Although the resolution is limited, the image suggests a general tendency of vertical deformation (along the loading direction) and some Poisson effect. | 56 |

- Fig. 4.11 Compressive stress-strain curves of monolithic β phase heat treated at 340°C. Note that the as-cast specimen did not fracture during the test. 57
- Fig. 4.12 Compressive stress-strain plots of β phase composites heat treated at 340°C. Here the as-cast specimen did not fracture in the duration of the test. 58
- Fig. 4.13 Compressive stress-strain curves of monolithic glass heat treated at 340°C. 58
- Fig. 4.14 Compression samples (6mm diam. x 14.4 mm length) after testing (left to right): as-cast monolithic β phase, same material after 16 hr HT, as-cast composite and the same material after 16 hr HT. 59
- Fig. 4.15 Diffraction patterns parallel to the loading axis for: (a) the composite sample and (b) the monolithic β phase sample. The raw data are shown as crosses fit with the Rietveld model. The lower curve exhibits the difference between the two. The sharp Bragg reflections in both patterns are from the BCC β phase (with a lattice constant of about 3.50 Å). In the composite (a), the presence of the amorphous BMG matrix is apparent from the undulating background. 64
- Fig. 4.16 Measured and calculated response of the monolithic β phase sample to applied compressive stress: (a) macroscopic strain along the loading axis; and (b) lattice plane specific elastic strain (symbols designate neutron data while lines are SCM predictions; here, “L” and “T” indicate longitudinal and transverse directions, respectively). The difference between measured and calculated macroscopic stiffness shown in (a) is likely due to extensometer problems. This claim is supported by the fact that the diffraction data in the elastic region is in good agreement with model calculations as shown in (b). 67
- Fig. 4.17 (a) Comparison of measured (by extensometer) and calculated (SCM) macroscopic stress-strain curve for the composite sample. (b) Comparison of measured (symbols) and calculated (lines) lattice specific stress-strain curves for the β phase in the composite sample (“L” and “T” indicate longitudinal and transverse directions, respectively). 68
- Fig. 4.18 Calculated *in-situ* behavior (phase stress vs. phase strain) for the composite. The arrows indicate the yield points in the β phase (about -650 MPa) and the BMG matrix (around -1350 MPa). The solid line (“macro”) designates the composite behavior. The *in-* 74

situ Young's moduli for each phase are also shown.

- | | | |
|-----------|--|----|
| Fig. 4.19 | Development of peak intensity parallel to the loading axis as a function of applied stress in the β phase for: (a) the composite, and (b) the monolithic β phase. | 76 |
| Fig. 4.20 | Macro stress-strain curve (left) and synchrotron X-ray diffraction data (lattice strain in the β phase - right) from an as-cast composite under cyclic tensile loading. | 78 |
| Fig. 4.21 | Schematic of dislocation width for a ceramic or ordered metal (top) and a typical ductile metal (below). | 80 |
| Fig. 4.22 | Self-consistent model calculation of composite (top) and phase-specific stress-strain plots (bottom) by varying the relative Young's moduli of the amorphous matrix and the β phase reinforcements. In the as-cast composites, $E_{\text{matrix}} / E_{\text{beta phase}} \sim 1.5$. The calculations employed the constitutive relations shown in Fig. 4.18 and assumed 25 vol.% dendrites. In the top figure, a clear trend is observed towards lower ductility (as quantified by the area under the stress-strain curve) when the β phase reinforcements become stiffer. | 81 |
| Fig. 5.1 | Backscattered SEM images of the microstructure of the wedge-shaped LM2A2 sample along its vertical axis. Here, the bright regions belong to the β phase while the dark area is the amorphous matrix. Numbers indicate distance from the bottom corner (magnification: x 1000). Slow cooling regions show large dendrite size as expected. | 91 |
| Fig. 5.2 | Backscattered SEM images of the microstructure of the wedge-shaped LM2A2 sample along its horizontal axis. Here, the bright regions belong to the β phase while the dark area is the amorphous matrix. Numbers indicate distance from the central line (magnification: x 1000). | 92 |
| Fig. 5.3 | Backscattered SEM images of the microstructure of the arc-melted, as-cast LM2A2 sample along its vertical axis. Here, the bright regions belong to the β phase while the dark area is the amorphous matrix. Numbers indicate distance from the bottom (magnification: x 1000). | 95 |
| Fig. 5.4 | Backscattered SEM images of the microstructure of the arc-melted, as-cast LM2A2 sample around its edges. Here, the bright regions belong to the β phase while the dark area is the amorphous matrix. Numbers indicate horizontal distance from | 96 |

the center (magnification: x 1000).

| | | |
|-----------|---|-----|
| Fig. 5.5 | Contour lines (not to scale) of the dendrite size distribution (left) and corresponding typical microstructure images (backscattered SEM) from the arc-melted sample. | 97 |
| Fig. 5.6 | Vickers indents (marked as white arrows) and the corresponding hardness and yield strength data for different regions within an arc-melted button. | 99 |
| Fig. 5.7 | Tensile yield strength calculated from Vickers hardness data vs. average dendrite size compared to tension tests of earlier composites from Caltech (5 μm dendrite size average) and Howmet (2 μm average) materials. | 100 |
| Fig. 5.8 | DSC scans for the $\text{Zr}_{56.2}\text{Ti}_{13.8}\text{Nb}_{5.0}\text{Cu}_{6.9}\text{Ni}_{5.6}\text{Be}_{12.5}$ (LM2) composite and amorphous matrix under a constant heating rate of $20^\circ\text{C}/\text{min}$. (T_g : $\sim 350^\circ\text{C}$, 1 st T_x : $\sim 400^\circ\text{C}$, 2 nd T_x : $\sim 450^\circ\text{C}$, $T_L(\text{matrix})$: $\sim 750^\circ\text{C}$). | 102 |
| Fig. 5.9 | 2-D diffraction images (top row - from a digital image plate) and their azimuthal integration (bottom row) of LM2 monolithic β phase samples. Experiments were performed at APS using a beam energy of 80 KeV and a beam size of $250\mu\text{m} \times 250\mu\text{m}$. The coarseness of the diffraction patterns (also called graininess) suggests a large grain size, especially in the as-cast sample. | 103 |
| Fig. 5.10 | Azimuthally integrated 2-D diffraction patterns during the <i>heating</i> of an <i>in-situ</i> β phase composite. Experiments were performed with high energy synchrotron XRD using a beam size of $100 \times 100 \mu\text{m}$. | 104 |
| Fig. 5.11 | Same as in Fig. 5.10, except the patterns were taken during the <i>cooling</i> stage of the experiment. | 105 |
| Fig. 5.12 | Azimuthally integrated diffraction patterns of an <u>as-cast</u> <i>in-situ</i> composite (top) and sample 2-D patterns before (lower left) after its heat treatment at 300°C for 18 hours (lower right). The diffraction data were collected using high energy XRD at APS (see Chapter 2 for details). | 109 |
| Fig. 5.13 | Azimuthally integrated diffraction patterns of a <u>water-quenched</u> <i>in-situ</i> composite (top) and sample 2-D patterns before (lower left) after its heat treatment at 300°C for 18 hours (lower right). The diffraction data were collected using high energy XRD at APS (see Chapter 2 for details). | 110 |

- Fig. 5.14 Evolution of LM2A2 monolithic β phase diffraction patterns during long term HT at 300°C (top) and 600°C (bottom). The data were collected *ex-situ* using a laboratory X-ray machine with Cu $K\alpha$ radiation at Caltech. Note that more peak broadening and splitting is observed at 300°C while no appreciable changes are seen after HT at 600°C. 111
- Fig. 5.15 Azimuthally integrated diffraction patterns of an as-cast (top) and a water-quenched (bottom) *in-situ* composite heat treated at 600°C for 1 hour. The experiments were conducted *in situ* using high energy XRD at APS. 113
- Fig. 5.16 Phase distribution in the LM2A2 composite after a 1 hr HT at 600°C. (One major difference from other crystallization studies was to have Nb in the alloy). 115
- Fig. 5.17 Synchrotron X-ray diffraction data used in determining phase volume fraction. The areas of crystalline peaks and amorphous background were calculated through image analysis. 116
- Fig. 5.18 Pseudo binary phase diagram for *in-situ* β phase composites. **M** and **B** represent the glassy matrix and the β phase, respectively. The Vitreloy 1 alloy, $(Zr_{75}Ti_{25})_{55}(Be_{50}(Cu_{55}Ni_{45})_{50})_{45}$ and the monolithic β phase, $Zr_{75}(TiNb)_{25}$ are chosen as binary axes. The *in-situ* composite, $(Zr_{75}(TiNb)_{25})_{75}(Be_{50}(Cu_{55}Ni_{45})_{50})_{25}$ falls on $x=0.424$ as indicated by the arrow. The composition of **M** ($Zr_{42.2}Ti_{9.4}Nb_{3.2}Cu_{13.7}Ni_{10.7}Be_{20.8}$) and **B** ($Zr_{71.1}Ti_{13.1}Nb_{13.4}Cu_{1.6}Ni_{0.8}$) were measured via electron microprobe analysis. **M** sits on $x=0.076$ based on Be content of 20.8% compared with 22.5% of Vit 1, while **B** occupies $x=0.947$ according to the ZrTiNb content $(97.6-55.0)/(100-55)$. The melting temperature of Vit 1 (720°C) and the $Zr_{75}(TiNb)_{25}$ β phase (1600°C) were deduced from literature. 117
- Fig. 5.19 Processing map for the Vit 1 and BCC β phase alloys. **M** represents the solubility limit of the β phase alloy within the glass forming region. Blue dashed line indicates the onset of dendritic phase under homogenous nucleation conditions. Materials shaded with yellow decompose into glass (**M**) and the BCC crystalline (**B**) phase when they cool down. The overall Nb content for the composite varies from 5.0 % to 7.5 % at the expense of Ti, yet bulk glass forming region extends further to the red dashed line, $(Zr_{75}Ti_{25})_{70}(Be_{50}(Cu_{55}Ni_{45})_{50})_{30}$, if Nb is not present in the alloy. 118
- Fig. A.1 Applied stress vs. elastic strain data of W reinforced BMG 131

composites from neutron diffraction. Both longitudinal and transverse strains are plotted.

| | | |
|----------|---|-----|
| Fig. A.2 | Applied stress vs. elastic stain data of Fe reinforced BMG composites from neutron diffraction. Both longitudinal and transverse strains are plotted. | 132 |
| Fig. A.3 | Applied stress vs. elastic stain data of Ta reinforced BMG composites from neutron diffraction. Both longitudinal and transverse strains are plotted. | 133 |
| Fig. A.4 | Applied stress vs. elastic stain data of Mo reinforced BMG composites from neutron diffraction. Both longitudinal and transverse strains are plotted. | 134 |
| Fig. B.1 | SEM image of an <i>in-situ</i> β phase composite: White area represents the BCC crystalline (β) phase while the black area is the amorphous matrix. Despite the dendritic nature of the BCC second phase, it is often observed in sphere-like or ellipsoidal shapes in many regions of two-dimensional images. | 135 |
| Fig. B.2 | Sphere-cube model for second phase area and volume fraction calculation: The sphere inside of the cube represents the BCC crystalline phase inside the amorphous matrix, and radius of the sphere, r' is an arbitrary value between 0 and r . The cube is the reference volume over which integration is performed, and the thin slice with a thickness dx is the integral element. | 136 |
| Fig. C.1 | Backscattered SEM images of the microstructure of the arc-melted <i>in-situ</i> β phase button along its vertical axis. The radius of the sample is 7.8 mm, and dendrite size varies from 1 ~ 12 μm along the vertical axis. (Modified from Fig. 5.3, magnification: x 1,000). | 138 |
| Fig. C.2 | Temperature profile calculated by FEM around the dendrite forming temperature range: 1000 $^{\circ}\text{C}$ ~ 1050 $^{\circ}\text{C}$. (Here, temperature scale is given in Kelvin.) The modeling was done in collaboration with Marios Demetriou at Caltech. | 139 |
| Fig. C.3 | C.3 Transient temperature distribution for different Biot numbers in a plane wall symmetrically cooled by convection. Note that a small Biot number (high heat transfer rate inside the materials) induces isothermal cooling and a large Biot number (high heat transfer rate at the interface) causes significant temperature gradients within the solid. Reproduced from Frank P. Incropera and David P. De witt "Introduction to Heat Transfer" p. 231. | 142 |

LIST OF TABLES

| | | |
|-----------|---|-----|
| Table 3.1 | Properties of reinforcement wires and two BMG matrices: $Zr_{57}Nb_5Al_{10}Cu_{15.4}Ni_{12.6}$ (Vit. 106) and $Zr_{41.2}Ti_{13.8}Cu_{12.5}Ni_{10.0}Be_{22.5}$ (Vit. 1). | 25 |
| Table 3.2 | Properties of 40% wire reinforced BMG composites in uniaxial compression <i>calculated</i> using FEM in comparison with neutron diffraction data. The data in the last row were obtained in a previous study. | 25 |
| Table 4.1 | Composition and elastic constants of LM2 <i>in-situ</i> composites. C: composite made at Caltech; H: composite made at Howmet; M: amorphous matrix; B: BCC dendrite. (E: Young's modulus, G: shear modulus, ν : Poisson's ratio). | 47 |
| Table 4.2 | Composition and elastic constants of LM2A2 <i>in-situ</i> composites and the corresponding monolithic versions of its components. (C: composite; M: monolithic matrix glass; B: monolithic β phase alloy). | 51 |
| Table 4.3 | Ultrasonic sound velocity measurement of the elastic constants of monolithic β phase as a function of heat treatment at 340°C. | 60 |
| Table 4.4 | Ultrasonic sound velocity measurement of the elastic constants of <i>in-situ</i> composites as a function of heat treatment at 340°C. | 60 |
| Table 4.5 | Ultrasonic sound velocity measurement of the elastic constants of monolithic glass as a function of heat treatment at 340°C. | 60 |
| Table 4.6 | Elastic constants for the β phase monolith determined from neutron diffraction data. Subscript "R" refers to Rietveld refinements and indicates elastic constants obtained from changes in lattice constants as a function of applied stress. Here, the error bars are based on linear fits to the neutron data. Subscript "S" refers to data from single peak fits which also employed the self-consistent model. The errors in this case are based on the least squares fitting routine. A is the anisotropy ratio: $2C_{44}/(C_{11}-C_{12})$. | 67 |
| Table 5.1 | Heat of mixing among matrix elements (a) and diffusivity data (b) at 350°C. Tracer self diffusivity data except for Be, which was measured in Zr solvent atmosphere. Real Be diffusivity: $D_{Be}(T_g) = 1.5 \times 10^{-15} \text{ cm}^2/\text{s}$, $D_{Be}(T_e) = 2.0 \times 10^{-6} \text{ cm}^2/\text{s}$ [24]. Considering diffusivity and heat of mixing Be_2Zr phase should form first and it agrees with other results. | 114 |

CHAPTER 1

INTRODUCTION

1.1 Metallic Glasses

It has been known that there are three major thermodynamic states: gas, liquid and solid, according to independent experimental variables such as temperature and pressure. The degrees of freedom among atomic bonds determine each state and there exists a first order transition between each state.

Glass is defined as vitrified liquid or a non-crystalline solid that demonstrates characteristics of both solid and liquid in terms of viscosity and structure. In other words, glass is a solid at room temperature (R.T). based on the definition of a solid [1] because viscosity exceeds $10^{14.6}$ poise, but is still a liquid because the structure of a liquid is maintained, whereas most of the solid turns into crystalline phases. A crystal is a periodic array of atoms which occupy each lattice point with 3-D translational symmetry. However, liquid is a more random array of atoms without long range periodicity. Therefore, a glass is considered to be an amorphous solid whose atomic structure is similar to that of liquid.

The most important characteristic of glass besides amorphous structure is the glass transition phenomenon. The glass transition T_g is the temperature where atomic configuration is frozen while viscosity keeps increasing with a decrease in temperature. Since thermodynamically metastable metallic glass formation is subject to kinetic processes, T_g is the function of the cooling rate as shown in Fig. 1.1. A non-crystalline solid below T_g is called a “glass”, and is referred to as a “supercooled liquid” above T_g [2].

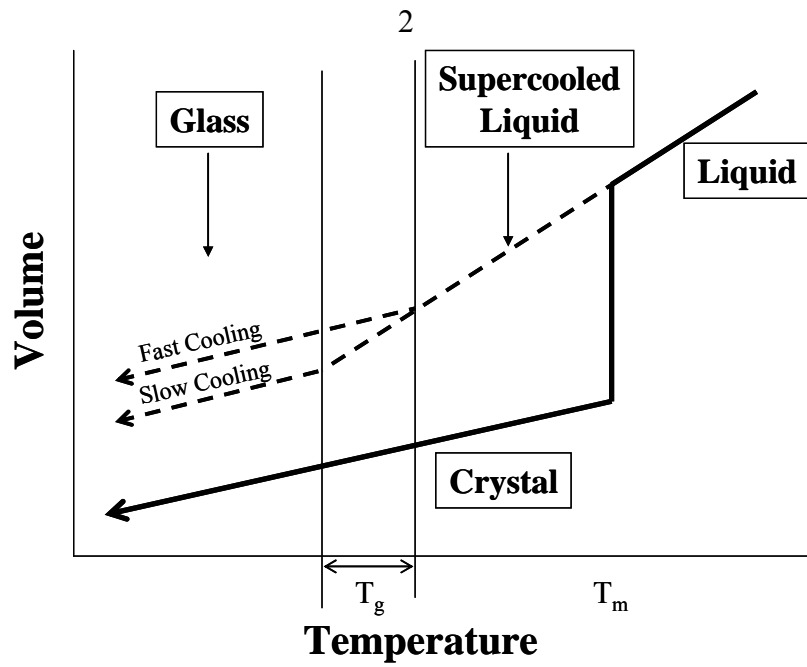


Fig. 1.1 Schematic diagram of volume change with respect to temperature as a liquid is cooled through the glass transition temperature, T_g .

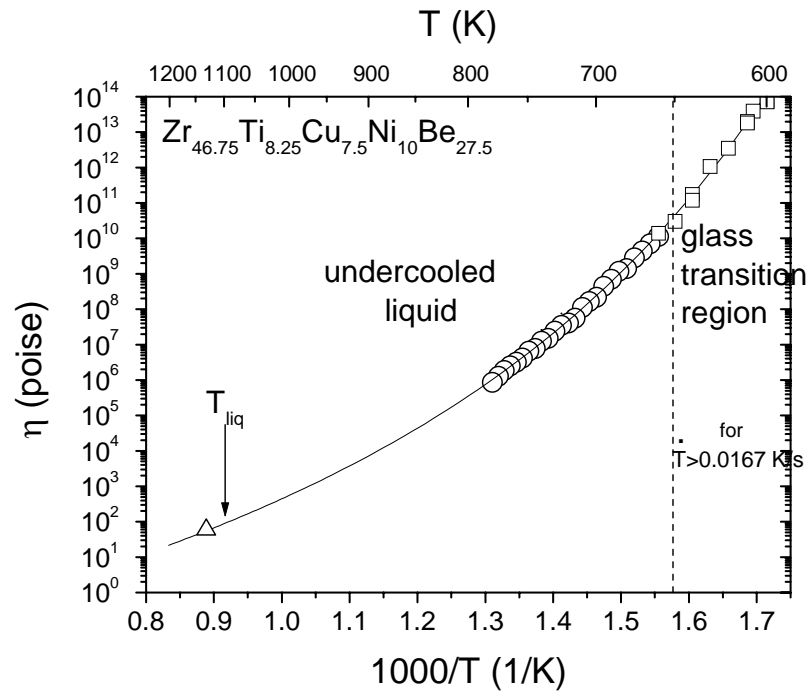


Fig. 1.2 Equilibrium viscosity as a function of temperature for the undercooled liquid of $Zr_{46.75}Ti_{8.25}Cu_{7.5}Ni_{10}Be_{27.5}$ "Vitreyloy 4" alloy. Reproduced from [3].

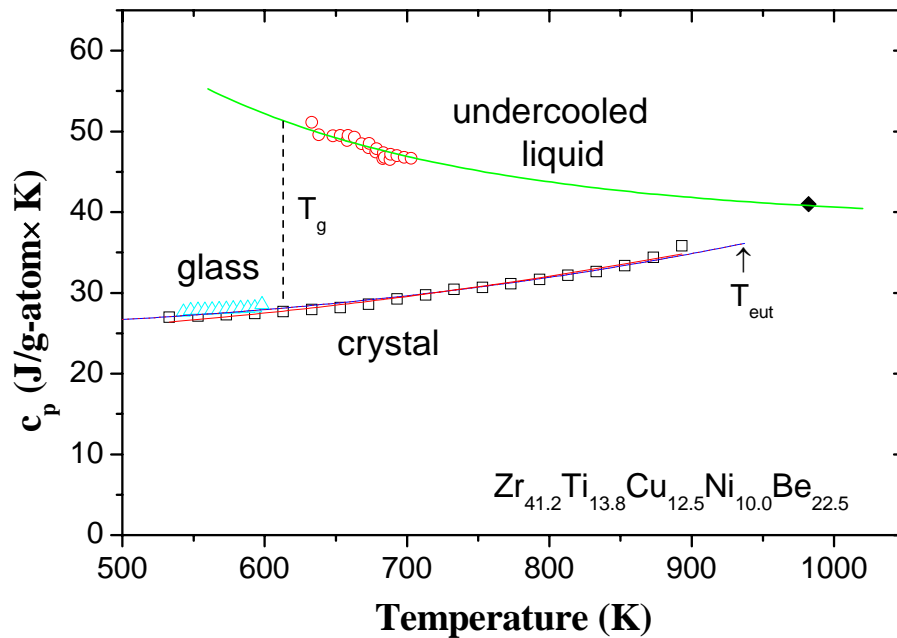


Fig. 1.3 Heat capacity of $Zr_{41.2}Ti_{13.8}Cu_{12.5}Ni_{10}Be_{22.5}$ metallic glass as a function of temperature: the point of discontinuity of C_p is the glass transition temperature, T_g . Reproduced from [4].

The easiest way to differentiate a glass from a crystalline phase is to monitor changes in volume (Fig. 1.1) as a function of temperature. An abrupt volume change during cooling is related to crystallization while glass transition is accompanied with a continuous change in volume and other thermodynamic variables such as entropy and enthalpy. Although the first order thermodynamic variables remain continuous with respect to temperature, their derivatives give rise to discontinuity or abrupt changes due to their slope difference around the transition interval. Therefore, heat capacity and thermal expansion vary very rapidly as shown in Fig. 1.3. Due to the fact that glass transition takes place within a certain temperature range, it is conventional to determine T_g at the onset of ΔH slope rise (C_p jump) in the DSC heating curve.

The quenching rate required to make glass out of a pure metal was estimated to be around 10^{10} K/s [5], and it was not possible to achieve such a high cooling rate in the laboratory. The first metallic glass, $\text{Au}_{75}\text{Si}_{25}$, was discovered by Klement, Willens, and Duwez at Caltech in 1960 by a rapid gun quenching technique that produced up to a 10^7 K/s cooling rate [6]. Many other metallic glass systems have been developed since then, but the critical cooling rate for glass forming was still too high to form bulk specimens. A breakthrough came in the late 1980's and early 1990's in two research groups at Tohoku University and Caltech. Inoue investigated a large variety of alloy systems [79] with a critical cooling rate of $10^1 \sim 10^2$ K/s. In 1993, Pecker and Johnson at Caltech developed $\text{Zr}_{41.2}\text{Ti}_{13.8}\text{Cu}_{12.5}\text{Ni}_{10}\text{Be}_{22.5}$ (Vitreloy 1) bulk metallic glass with a critical cooling rate of 1 K/s, which means that up to a 5 cm diameter rod could be processed by the conventional casting method without any crystallization [10]. Lin and Johnson found a new Cu-based metallic glass ($\text{Cu}_{47}\text{Ti}_{34}\text{Zr}_{11}\text{Ni}_8$, Vitreloy 101) and other Zr-based glass systems ($\text{Zr}_{52.5}\text{Ti}_5\text{Cu}_{17.9}\text{Ni}_{14.6}\text{Al}_{10}$, Vitreloy 105; $\text{Zr}_{57}\text{Nb}_5\text{Cu}_{15.4}\text{Ni}_{12.6}\text{Al}_{10}$, Vitreloy 106) with a critical cooling rate of 10 K/s were also developed [11]. While Vitreloy 1 has been known as the best metallic glass forming alloy up to now, Vitreloy 106 is regarded as the best non-Be metallic glass forming alloy.

Bulk metallic glass (BMG) formation provided many opportunities to investigate various mechanical properties, including constitutive behavior, flow criteria, fracture and fatigue, as well as thermodynamic and kinetic characteristics [12]. BMGs have attracted attention as promising structural materials due to their high elastic limit (2%), high strength (around 2 GPa), and good fracture toughness ($20\text{-}55 \text{ MPa}\cdot\text{m}^{1/2}$) [13-15]. Fig. 1.4 shows the difference in strength between pure metals and a metallic glass.

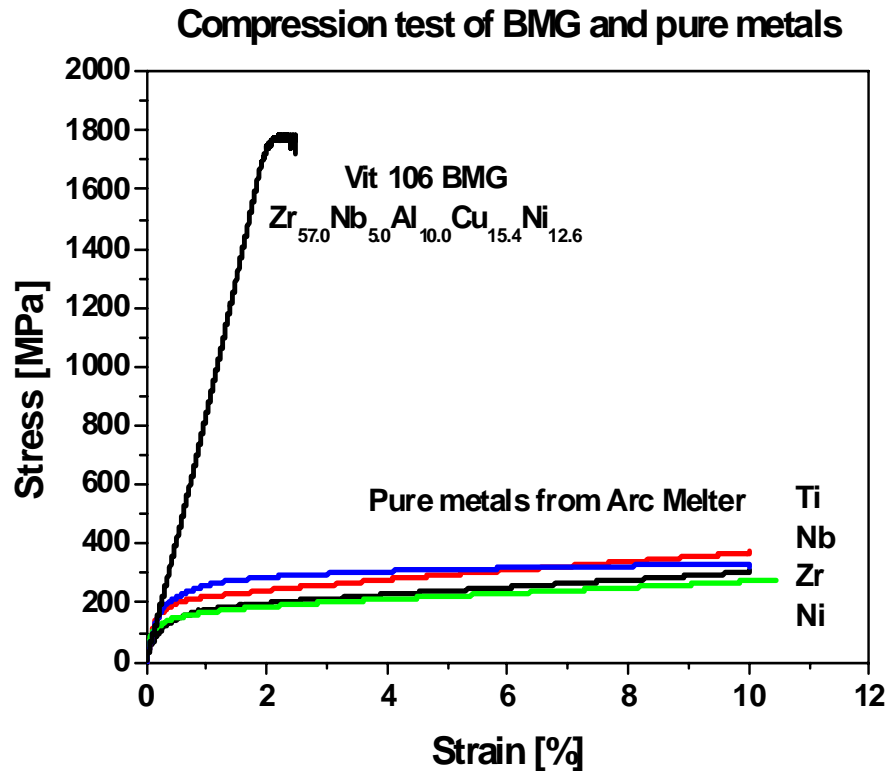


Fig. 1.4 Stress strain curve of Vitreloy 106 BMG and some pure metals. All samples were melted and cooled in the arc melter. All pure metals show low yield strength and large ductility while BMG exhibits very high yield strength but no plasticity.

1.2 Metallic Glass Composites

The deformation mechanism of metallic glass is different from that of crystalline materials. Plastic deformation of crystalline phases is carried out by the movement of dislocations, and the interactions between dislocations themselves and other defects such as inclusions and grain boundaries introduce work hardening behavior in typical crystalline alloys. However, due to its unique structural characteristics, the only plastic deformation mechanism in amorphous alloys at low temperatures is shear band formation. (it should be noted that at sufficiently high temperatures, metallic glasses can

deform via viscous flow.) Once a shear band starts to propagate, it usually penetrates all the way through the sample, leading to catastrophic failure in a monolithic metallic glass.

It has been determined that the main toughening mechanism of a BMG is to introduce second phase materials in order to prevent single shear band propagation and by forming multiple shear bands instead. Several kinds of BMG matrix composites were suggested by Choi-Yim and Conner at Caltech, and they exhibit significantly improved damage tolerance [16-20].

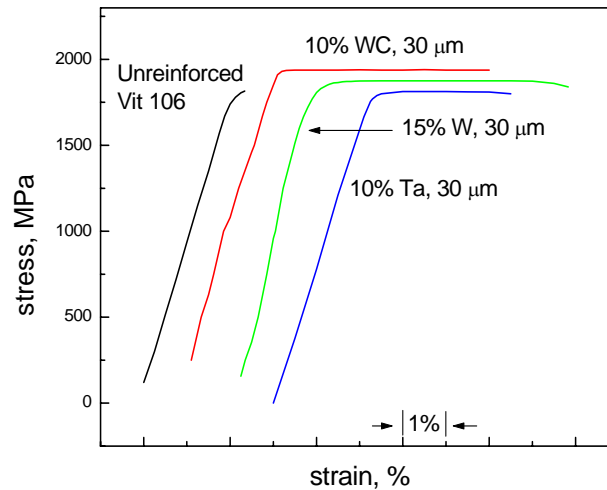


Fig. 1.5 Compression tests of various kinds of particulate composites. (Reproduced from Choi-Yim Ph.D. thesis [21])

To date, there are two major *ex-situ* composites: particulate and wire composites. Fig. 1.5 shows that the ductility of particulate composites is enhanced significantly in compression, but no practical improvement is found in tension [21]. The optimum particulate composite is yet to be determined but it seems that the particulate reinforcements are more effective with larger volume fraction and/or bigger size. Another important factor is the interface strength between the matrix and reinforcements. It is

known that carbide particles tend to form ZrC at the interface in a Vitreloy 106 matrix, and in general, interface strength can be aided or deteriorated by such a third phase [18]. The constitutive behavior of W particulate composites was recently investigated by X-ray diffraction and Eshelby modeling and it was found that the W particles yield first and then transfer load to the BMG matrix [22].

As W particles lead to a considerable toughening in the BMG matrix composites, W wires have also shown the best performance among many wire reinforced systems. Fig. 1.6 shows the compression test data from a series of W reinforced Vitreloy 1 composites exhibiting an outstanding increase in toughness without sacrificing compressive strength at all. Clausen and Üstündağ investigated *in-situ* behavior of these composites using neutron diffraction and finite element modeling (FEM), and showed that the W wires yield first and start to transfer load to the matrix at around 1300 MPa, whereas the matrix yielded at 1900 MPa by multiple shear band formation [23]. Thermal residual stress also plays an important role here. For instance, the 20% W composites yield first due the largest thermal residual stress, which can be as high as -500 MPa in the W [24]. The source of these residual stresses is the thermal expansion mismatch between the matrix and the wires. The “freezing” temperature below which residual stress buildup starts during cooling down turns out to be near the glass transition temperature of the glass matrix.

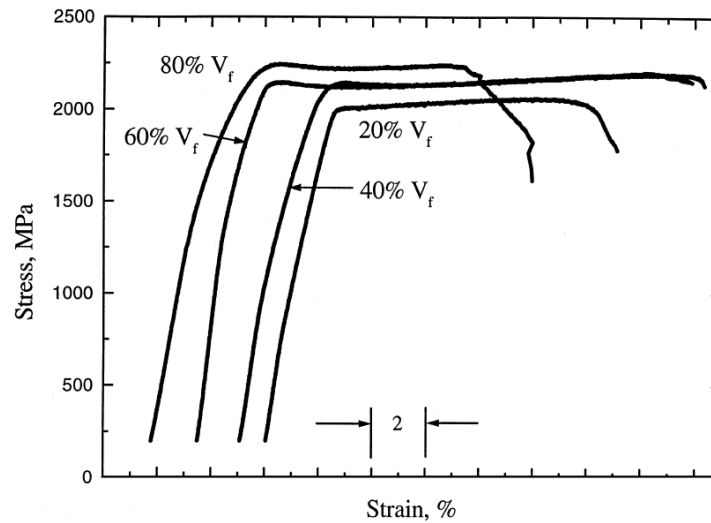


Fig. 1.6 Compression data of W wire reinforced Vitreloy 1 composites. (20 ~ 80%). (Reproduced from Conner et al. [17]).

The most attractive BMG composites are obtained *in-situ* as the reinforcements precipitate out during casting [25-27]. This phase has a BCC crystal structure, consisting primarily of Zr and Ti, and hence, is referred to as the “ β phase” since it is reminiscent of the β allotrope of both Ti and Zr (their “ α phase” at room temperature has an HCP crystal structure). Upon cooling from the high temperature melt, the initial alloy undergoes partial crystallization by nucleation and dendritic growth of the β phase. The remaining liquid subsequently freezes to an amorphous solid producing a two-phase microstructure containing β phase dendrites in a glassy matrix. The dendritic structure of the β phase has been shown to inhibit the formation of macroscopic shear bands in the matrix which cause catastrophic failure in monolithic BMGs. It was found that the β phase leads to the formation of multiple shear bands in the glass matrix with a similar spacing to that of the secondary dendrites in the β phase. However, neither the underlying deformation

mechanisms nor the load sharing in the composite could be determined in previous studies.

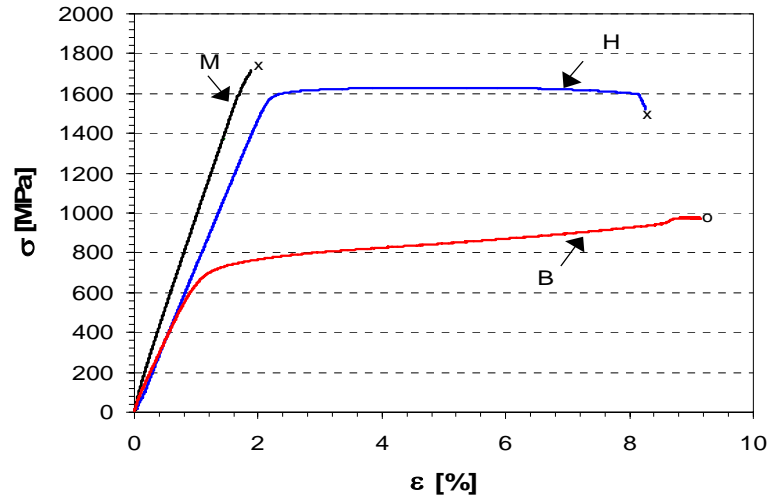


Fig. 1.7 Compressive stress-strain curves of an *in-situ* β phase composite compared with those from a monolithic matrix and a monolithic β phase. (Reproduced from Kim, Ph.D. thesis [28]) M: Amorphous matrix; H: Composite made at Howmet; B: Monolithic β phase alloy.

1.3 Overview of the Thesis

The brief overview of the BMG composite studies described above makes it clear that various metallic glass composite systems have been developed with enhanced ductility compared to monolithic BMG alloys. However, all the mechanical tests conducted previously were macroscopic and only measured the overall, bulk-averaged response of the composite. For this reason, important details about the deformation mechanisms and load sharing between the matrix and reinforcements were lacking. Without a good appreciation of the effective deformation mechanisms in BMG composites, it will be impossible to further improve their properties and obtain the

“ideal” composite with high strength and ductility. The present study integrated advanced diffraction methods such as neutron and high energy X-ray diffraction to monitor the *in-situ* lattice strain evolution in the crystalline reinforcements and mechanics modeling to reach conclusions about the deformation of BMG matrix composites.

Based on the previous work on W reinforced composites, other wire composite systems were investigated using neutron diffraction and FE modeling. The overall mechanical behavior and modeling results are discussed in Chapter 3.

An extended study on *in-situ* β phase composites is described in Chapter 4 and Chapter 5. Here, the deformation mechanisms were studied by combining neutron diffraction and self-consistent modeling. An unexpected stiffening behavior of the monolithic β phase was discovered and led to a systematic heat treatment study to demonstrate the effects of processing conditions on the mechanical properties of composites. Compressive and tensile properties are summarized, along with ultrasound measurements of elastic constants in Chapter 4.

Due to the fact that the mechanical properties were discovered to be highly sensitive to processing conditions and phase evolution according during heat treatment, Chapter 5 is dedicated to phase analysis and microstructure evolution. The pseudo binary phase diagram (of Vitreloy 1 - β phase) was constructed from a high temperature experiment and is also presented in this chapter.

Finally, Chapter 6 presents an overall summary and lists some future directions for further research on BMG composites.

References

- [1] S. R. Elliott (1983). *Physics of Amorphous Materials*.
- [2] X. H. Lin (1997). Bulk glass formation and crystallization of Zr-Ti based alloys. Caltech Ph.D Thesis.
- [3] E. Bakke, R. Busch and W. L. Johnson (1995). *Applied Physics Letters* **67**(22): 3260-3262.
- [4] R. Busch, Y. J. Kim and W. L. Johnson (1995). *Journal of Applied Physics* **77**(8): 4039-4043.
- [5] H. S. Chen (1976). *Materials Science and Engineering* **23**(2-3): 151-154.
- [6] W. Klement, R. H. Willens and P. Duwez (1960). *Nature* **187**(4740): 869-870.
- [7] A. Inoue, T. Nakamura, N. Nishiyama and T. Masumoto (1992). *Materials Transactions Jim* **33**(10): 937-945.
- [8] T. Zhang, A. Inoue and T. Masumoto (1991). *Materials Transactions Jim* **32**(11): 1005-1010.
- [9] A. Inoue, T. Zhang and T. Masumoto (1990). *Materials Transactions Jim* **31**(5): 425-428.
- [10] W. L. Johnson (1996). Fundamental aspects of bulk metallic glass formation in multicomponent alloys. *Metastable, Mechanically Alloyed and Nanocrystalline Materials, Pts 1 and 2*. **225**: pp. 35-49.
- [11] X. H. Lin and W. L. Johnson (1995). *Journal of Applied Physics* **78**(11): 6514-6519.
- [12] J. Lu (2002). Mechanical behavior of a bulk metallic glass and its composites over a wide range of strain rates and temperature. Caltech Ph.D Thesis.
- [13] W. L. Johnson (2002). *Jom-Journal of the Minerals Metals & Materials Society* **54**(3): 40-43.
- [14] R. D. Conner, A. J. Rosakis, W. L. Johnson and D. M. Owen (1997). *Scripta Materialia* **37**(9): 1373-1378.
- [15] C. J. Gilbert, R. O. Ritchie and W. L. Johnson (1997). *Applied Physics Letters* **71**(4): 476-478.

- [16] R. D. Conner, H. Choi-Yim and W. L. Johnson (1999). *Journal of Materials Research* **14**(8): 3292-3297.
- [17] R. D. Conner, R. B. Dandliker and W. L. Johnson (1998). *Acta Materialia* **46**(17): 6089-6102.
- [18] H. Choi-Yim, R. Busch, U. Koster and W. L. Johnson (1999). *Acta Materialia* **47**(8): 2455-2462.
- [19] H. Choi-Yim and W. L. Johnson (1997). *Applied Physics Letters* **71**(26): 3808-3810.
- [20] H. Choi-Yim, R. D. Conner, F. Szuecs and W. L. Johnson (2002). *Acta Materialia* **50**(10): 2737-2745.
- [21] H. Choi-Yim (1999). Synthesis and characterization of bulk metallic glass matrix composites. Caltech Ph.D Thesis.
- [22] D. K. Balch, E. Ustundag and D. C. Dunand (2003). *Metallurgical and Materials Transactions a-Physical Metallurgy and Materials Science* **34A**(9): 1787-1797.
- [23] B. Clausen, S. Y. Lee, E. Ustundag, C. C. Aydiner, R. D. Conner and M. A. M. Bourke (2003). *Scripta Materialia* **49**(2): 123-128.
- [24] D. Dragoi, E. Ustundag, B. Clausen and M. A. M. Bourke (2001). *Scripta Materialia* **45**(2): 245-252.
- [25] C. C. Hays, C. P. Kim and W. L. Johnson (2000). *Physical Review Letters* **84**(13): 2901-2904.
- [26] C. C. Hays, C. P. Kim and W. L. Johnson (2001). *Materials Science and Engineering a-Structural Materials Properties Microstructure and Processing* **304**: 650-655.
- [27] F. Szuecs, C. P. Kim and W. L. Johnson (2001). *Acta Materialia* **49**(9): 1507-1513.
- [28] C. P. Kim (2001). Ductile phase reinforced bulk metallic glass composites formed by chemical partitioning. Caltech Ph.D Thesis.

CHAPTER 2

EXPERIMENTAL PROCEDURES

2.1 Synthesis of Metallic Glass Matrix Composites

2.1.1 Wire Composites

Ingots of the Vit.106 alloy were prepared by arc-melting elemental metals with a purity of 99.7% or higher in a Ti-gettered Ar atmosphere. Tungsten, stainless steel (type 302) and Mo reinforcement wires were purchased from Thermionic, Inc. (North Plainfield, NJ 07060) and Alfa Aesar (Ward Hill, MA 01835) supplied the Ta wire. All wires were 0.25 mm in diameter and were straightened before processing the composites using the melt infiltration procedure [1]. Specifically, a stainless steel tube containing the wire bundle at the bottom was evacuated to about 3×10^{-2} torr and flushed with Ar gas several times. While still under vacuum, it was heated to 975°C and held there for 10 min to melt the Vit. 106 alloy. After melting the metallic glass, the temperature was lowered to 875°C and held for another 15 min during which 100 psi Ar gas pressure was applied to force the molten alloy into the tube. This was followed by quenching the tube in water at room temperature. Since Vit 106 can be processed up to 10 mm in diameter, an 8 mm inner diameter stainless tube was used. Compression test samples were machined into a cylindrical geometry of 6 mm diameter and 14.4 mm length with the fiber axes parallel to the sample axis for neutron diffraction experiment. In order to have uniform distribution of wires in low volume fractions such as 40%, wire bundles were slightly bent in the middle to attain a uniform increase distribution within the tube. Each sample was characterized by X-ray diffraction before machining to ensure a glassy matrix.

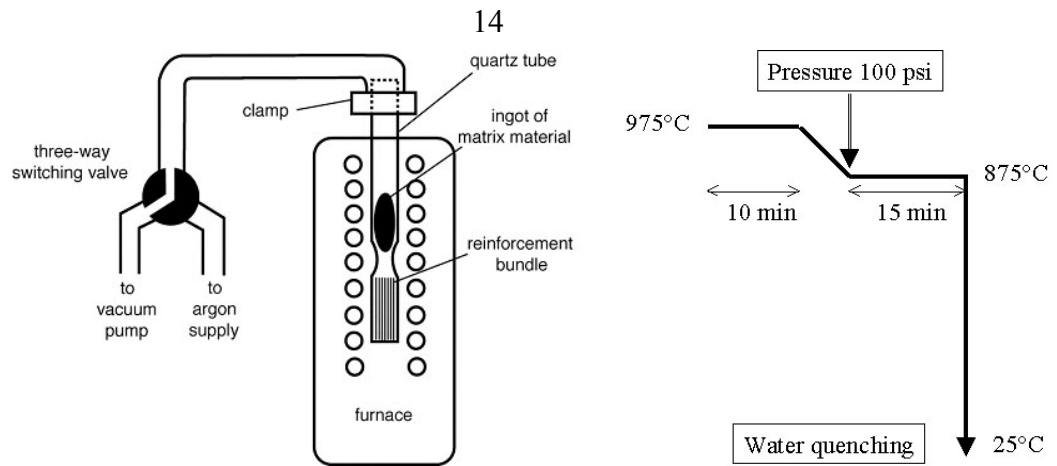


Fig. 2.1 Experimental setup and schematic diagram for the wire composite casting procedure. (reproduced from [1])

2.1.2 *In-situ* Composites

Specimens were prepared by alloying high purity Cu (99.999 %), Ni (99.995 %), and Ti (99.995 %), all from Cerac, Inc., Milwaukee, WI 53201; Nb (99.8 %) from Alfa Aesar, Ward Hill, MA 01835; Zr with less than 300 ppm oxygen content from Teledyne Wah-Chang Inc., Albany, OR 97321; and Be (99.99 %) from Electronic Space Products International, Ashland, OR 97520. The alloys were prepared in the form of 25 g or 40g rods of roughly cylindrical geometry by plasma arc melting in a Ti-gettered argon atmosphere on a water-cooled Cu plate. The molten alloy was then undercooled to a temperature range between the liquidus and solidus for a given composition [2]. This led to the chemical partitioning of the undercooled liquid into a solid (crystalline metal dendrites - the β phase) and a liquid phase with a different composition. The liquid phase was depleted of the elements going into the β phase which shifted its composition to that of a bulk metallic glass forming alloy. Cooling of the remaining liquid thus resulted in the formation of an amorphous matrix around the crystalline phase. In addition to the composite, a monolithic β phase sample with the same chemical composition found in the

dendrites of the composites was prepared by the arc melting procedure described above, except that there was no high-temperature hold used in the chemical partitioning step.

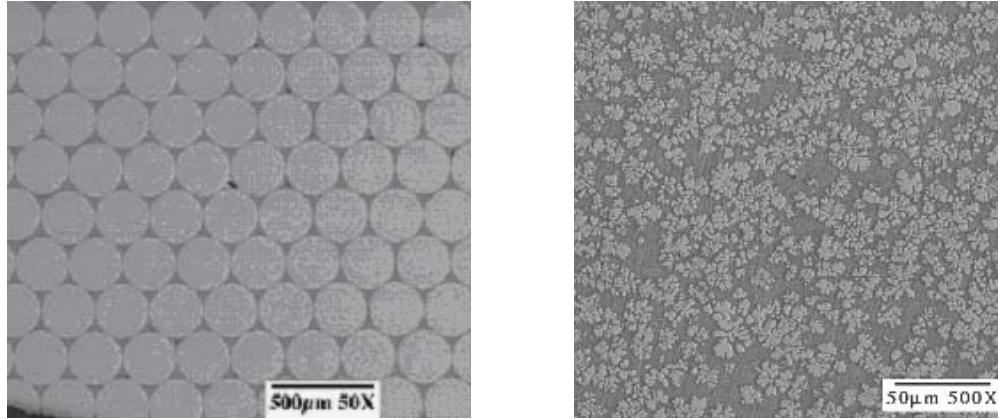


Fig. 2.2 SEM images of an 80% W wire composite (left) and an *in-situ* β composite. (Unlike Vit 1-W composites [1], there is no reaction layer between Vit 106 and W).

2.2 Mechanical Tests and Microscopy

2.2.1 Loading Tests

Mechanical test specimens were machined into a cylindrical shape with 3 mm diameter x 6 mm height (aspect ratio of 2.0), or ingots were cast by 3 mm diameter Cu mold for compressive loading test at Caltech by Instron 4204. The crosshead speed was 0.1mm per minute with a corresponding strain rate of $2.8 \times 10^{-4}/s$ for a 6mm high sample. The maximum of 10,000 lbs. for the load cell allows up to 5 mm diameter in metallic glass samples. However, neutron diffraction samples were machined into 6mm diameter x 14.4 mm height (aspect ratio of 2.4) due to the large sampling volume associated with neutron scattering factor.

2.2.2. Ultrasound Measurements of Elastic Constants

The ultrasonic sound velocity was measured to calculate elastic modulus, shear modulus and Poisson's ratios of the specimens, and the mass densities were measured according to the hydrostatic weighing technique [3]. Measurements were made using a Parametrics Model 5052UA ultrasonic analyzer connected to an oscilloscope for data analysis. Transmission and reflection modes were used, depending upon sample conditions, and the typical error range of sound velocity measurement was about 5% of total values. The basic equations for shear modulus G , Young's modulus E , and Poisson's ratio ν are given below as a function of density ρ , normal sound velocity v_l , and shear sound velocity v_s .

$$G = \rho (v_s)^2$$

$$E = \rho (v_s)^2 \frac{3 - 4 \left(\frac{v_s}{v_l} \right)^2}{1 - \left(\frac{v_s}{v_l} \right)^2}$$

$$\nu = \frac{E}{2G} - 1$$

2.2.3 SEM and Microprobe Analysis

Samples were cut into small pieces to be mounted in a BUEHLER SIMPLIMET 1000 mounting machine and were polished by a BUEHLER ECOMET 3 polisher down to 1 μm level. LEO 1550 VP Field Emission Scanning Electron Microscopy (FE SEM) was used to observe microstructures. The significant contrast between the matrix and reinforcement in wire composites did not require surface etching under RBSD

(Rutherford back scattering detector) mode, but *in-situ* composite surface was etched with a solution of 40% HF, 20% HNO₃, and 40% HCl [4].

The chemical composition of the monolithic matrix and β phase was determined using a JEOL JXA-73 electron microprobe analyzer with the elements of Zr, Ti, Nb, Cu and Ni used as standards, whereas the Be content was calculated by difference. Both the matrix and β phase were randomly selected by six data points each, after which a mean value of six data points was selected. Since Be was not detected within the instrument resolution in β phase, all of Be was assumed to be in the matrix. Based on these data, monolithic β phase and monolithic glass samples were prepared.

2.3 Neutron Diffraction of Wire and *In-situ* Composites

2.3.1 Experimental Procedure

Neutron diffraction experiments were conducted under uniaxial compression using the SMARTS diffractometer [5] at the Lujan Neutron Science Center, Los Alamos National Laboratory. The geometric setup of SMARTS allows simultaneous measurements in longitudinal and transverse directions (Fig. 2.3). The diffraction data were collected using the time-of-flight technique. Elastic strain in the wires or β phase was calculated from changes in their lattice parameters as a function of applied stress. Strains are reported relative to the initial strain state at a -5 MPa applied stress (which was needed to hold samples in a horizontal loading geometry). Each composite was subjected to several loading-unloading cycles while the longitudinal macroscopic strain was measured with an extensometer. Neutron data were collected under load control in

15-20 minute runs at approximately 25-100 MPa stress intervals. A compressive strain rate of about 10^{-4} /sec was employed between load levels.

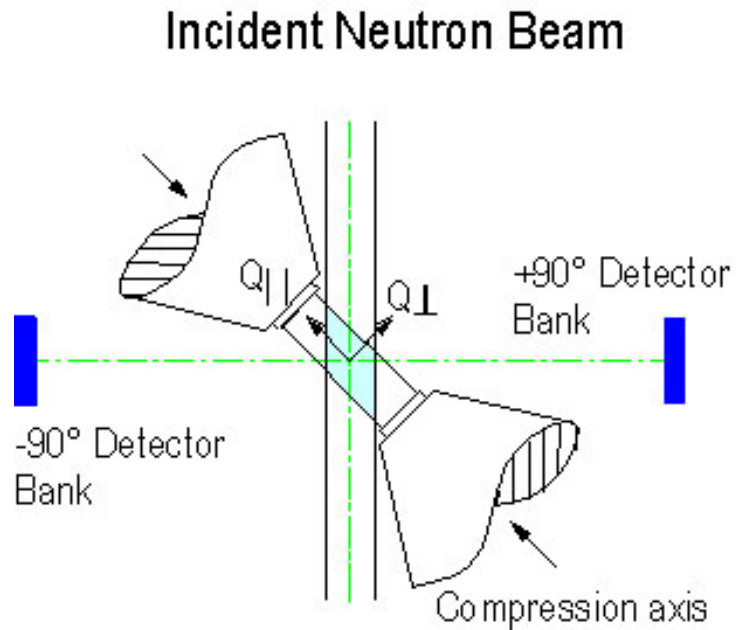
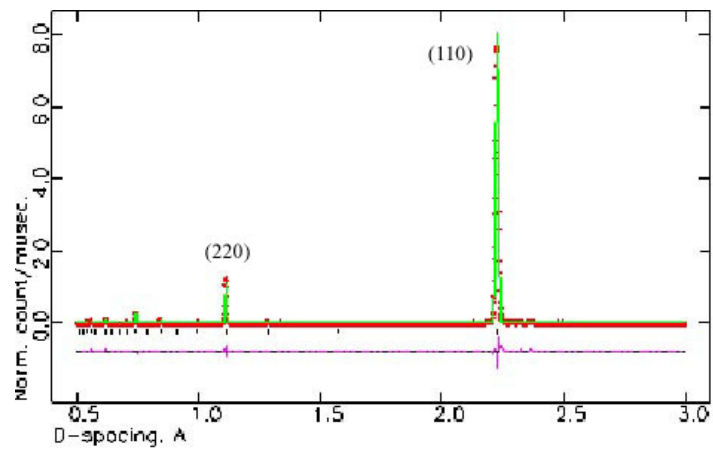


Fig. 2.3 Schematic of sample geometry with respect to beam and loading direction.

2.3.2 Data Analysis



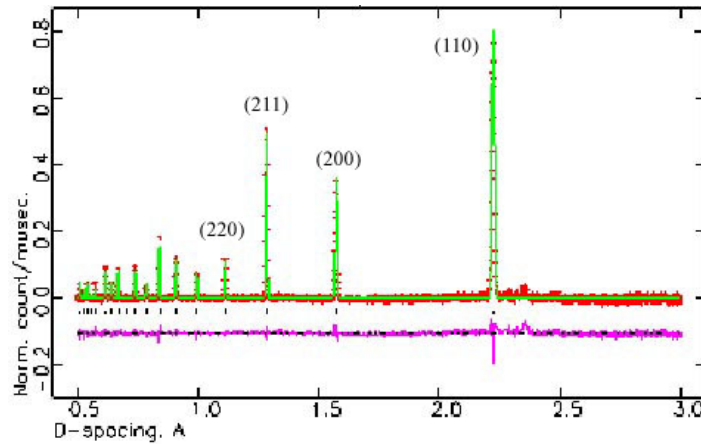


Fig. 2.4 Refined diffraction pattern of Mo (BCC) wire composites. (Top: Longitudinal, Bottom: Transverse).

Fig. 2.4 shows diffraction data of Mo wires (textured along $\langle 110 \rangle$ direction) with refinement using the Rietveld method [6-7]. The refined parameters through GSAS (General Structure Analysis System) are background, histogram scale factor, lattice parameter, orientation distribution, absorption, and isotropic atomic displacement, U_{iso} . The lattice parameters were determined from the entire diffraction pattern to within a 5×10^{-5} fitting error in wire composites and 15×10^{-5} in β phase composite.

It must be remembered that the strain information is elastic strain from the crystalline phase, and total strain is given by extensometer attached to the sample. Since neutron reveals only reinforcement behavior due to a lack of diffraction information from the amorphous phase, mechanical modeling (Finite Element Modeling in wire composites and Self Consistent Modeling in *in-situ* β phase composite) has to be applied to account for glass matrix behavior. The final output would be the *in-situ* phase stress-strain curve of each phase. More details on modeling will be described in Chapters 3 and 4.

2.4 Synchrotron X-ray Diffraction of *In-situ* Composites

2.4.1 High Energy X-ray Diffraction Procedure

Two kinds of experiments utilized high energy X-ray diffraction at beam line 1-ID in Advanced Photon Source (APS): *in-situ* tensile loading of *in-situ* β phase composite, and phase evolution experiments according to heat treatment. The energy of the beam was 80 KeV ($\lambda=0.1536\text{\AA}$), and beam & detector size were adjusted on a case by case basis. The beam size varied from $100\ \mu\text{m} \times 100\ \mu\text{m}$ to $250\ \mu\text{m} \times 250\ \mu\text{m}$, and original detector size ($500\ \text{mm} \times 500\ \text{mm}$) was reduced to $300\ \text{mm} \times 300\ \text{mm}$ for speedy data collection in the heat treatment experiment. X-ray recording took less than 15 seconds, but one minute had to be used for erasing image plate which delays overall time resolution down to two minutes. Silicon or Alumina was used as a standard for correcting diffraction peaks.

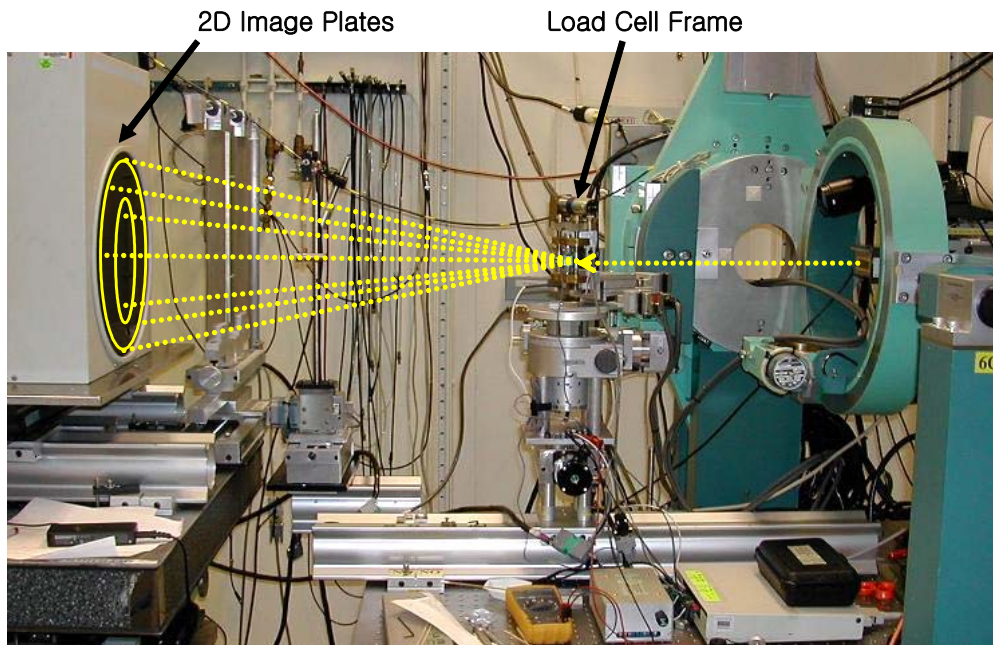


Fig. 2.5 APS *in-situ* tensile loading experimental setup in beam line 1-ID. The dotted lines represent synchrotron beams and the load cell frame is located in the middle.

2.4.2 Data Analysis

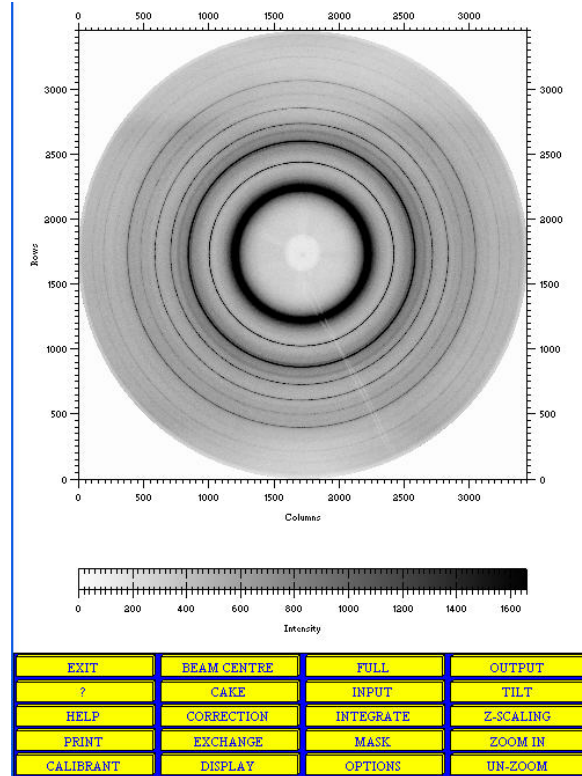


Fig. 2.6 A captured image of Cu mold casting β phase composite during FIT 2D analysis.

By using Si and Al_2O_3 as standards, sample to detector distance, beam center, and tilt angle were determined, followed by integration of diffraction peaks from samples. Azimuth angle for integration can be varied according to the purpose: the 10° integration was done in a vertical and horizontal direction in the case of loading experiment in order to deduce normal and shear strain, and the whole 360° integration was suitable for phase analysis. Once output files are generated in the form of GSAS, the rest of the refinement steps and modeling part will be the same as the neutron data as explained above.

References

- [1] R. B. Dandliker, R. D. Corner, W. L. Johnson, *J. Mater. Res.* 13 (1998) 2896.
- [2] Hays, C. C.; Kim, C. P.; Johnson, W. L. *Physical Review Letters* **2000**, *84*, 2901-2904.
- [3] ASTM (1998). Standard Test Method for Density of Glass by Buoyancy.
- [4] C. P. Kim (2001). Ductile phase reinforced bulk metallic glass composites formed by chemical partitioning. Caltech Ph.D. Thesis
- [5] M. A. M. Bourke, D. C. Dunand, E. Üstündag, *Appl. Phys. A*, 74 (2002) S1707.
- [6] H. M. Rietveld, *Acta Cryst.* 22 (1967) 151.
- [7] A. C. Larson, R. B. Von Dreele, GSAS-General Structure Analysis System, LAUR 86-748: Los Alamos National Laboratory; 1986.

CHAPTER 3

RESULTS AND DISCUSSION:

MECHANICAL BEHAVIOR AND MODELING OF WIRE COMPOSITES

3.1 Compressive Loading of Wire Composites

Bulk metallic glasses (BMGs) are attractive structural materials due to their unique mechanical properties: large elastic strain limit (about 2%), high strength (above 2 GPa), good fracture toughness ($\sim 20 \text{ MPa m}^{1/2}$), good specific strength, high corrosion resistance, and so on [1-3]. However, they exhibit poor ductility at room temperature as they usually fail catastrophically under unconstrained loading due to unstable shear band formation. Several BMG composites have been produced to mitigate this failure mode [4-7]. Among different kinds of composites developed, those with continuous unidirectional metallic wire reinforcements have exhibited enhanced mechanical properties. For instance, composites with Vitreloy 1 ($\text{Zr}_{41.2}\text{Ti}_{13.8}\text{Cu}_{12.5}\text{Ni}_{10.0}\text{Be}_{22.5}$) matrix and 20-80 vol.% W wires have nearly preserved the high yield strength of the BMG, but have added significant ductility (total strain to fracture reaching 15-20% in compression) [5].

Recent work by Üstündag and co-workers using neutron diffraction (ND) and finite element modeling (FEM) has elucidated the bulk deformation mechanisms in the W wire composites [8-9]. It was shown that significant thermal residual stresses develop in these composites due to the coefficient of thermal expansion (CTE) mismatch between the matrix and reinforcements [8]. Specifically, these stresses are generated during

cooldown starting around the glass transition temperature of the matrix and can exceed -500 MPa in the axial direction of the W wires [8]. When the W composites are loaded in compression, these compressive thermal residual stresses induce yielding in the W wires at applied stresses lower than those expected in a residual-stress-free composite [9]. This investigation also showed that it is always the W wires that first experience plastic deformation followed by “yielding” in the BMG matrix in the form of multiple shear band formation [9]. The presence of the W wires stabilizes the production of multiple shear bands in the BMG, thereby enhancing the overall ductility of the composite.

A similar combined ND-FEM methodology was followed in the present study. A different BMG alloy, Vitreloy 106 ($Zr_{57}Nb_5Al_{10}Cu_{15.4}Ni_{12.6}$), was chosen as the matrix. Vit.106 is among the best glass forming alloys, i.e., it can be cast into large dimensions and is Be-free, an important environmental advantage. Three different materials were considered for reinforcement: type 302 stainless steel, Mo, and Ta. The reinforcement volume fraction was kept at 40% for ND and FEM, and similar to the W composites, the wires were unidirectional. These reinforcements have different properties compared to W (Table 3.1). For instance, their yield strengths and Young’s moduli are lower than those of W, and one of them (steel) has a higher CTE than that of the matrix. The purpose of the present study was to quantify the effects of the different reinforcement properties on the deformation of the BMG composites. This section begins by presenting macroscopic data and fracture morphology. It proceeds with results from ND and FEM studies.

| | Elastic modulus E (GPa) | Poisson's ratio (ν) | Yield strength σ_Y (MPa) | CTE ($10^{-6}/K$) |
|------------------------------|---|---|---|---|
| Vit. 106 | 85 ^[13] | 0.38 ^[13] | 1800 ^[13] | 8.7 ^[13] (at 293 K) |
| Type 302 SS | 193 ^[11] | 0.25 ^[11] | 250 ^[11] | 17.2–18.4 ^[11] (at 293-800 K) |
| Mo | 330 ^[14] | 0.38 ^[14] | 400 ^[14] | 4.8–5.7 ^[12] (at 293-800 K) |
| Ta | 186 ^[13] | 0.35 ^[13] | 350 ^[13] | 6.3–7.2 ^[12] (at 293-800 K) |
| Vit. 1 ^[9] | 96 | 0.36 | 1900 | 9.0 (at 293 K) |
| W ^[9] | 410 | 0.28 | 1300 | 4.5 (at 293 K) |

Table 3.1 Properties of reinforcement wires and two BMG matrices:

$Zr_{57}Nb_5Al_{10}Cu_{15.4}Ni_{12.6}$ (Vit. 106) and $Zr_{41.2}Ti_{13.8}Cu_{12.5}Ni_{10.0}Be_{22.5}$ (Vit. 1).

| | Wire yield strength (von Mises stress) σ_Y (MPa) | Wire axial thermal residual stress (MPa) | Composite axial yield stress (MPa) |
|-------------------------|---|---|---|
| Type 302 SS | 175 | ~0 | – 120 |
| Mo | 350 | – 160 | – 140 |
| Ta | 80 | – 90 | – 20 |
| W ^[9] | 1300 | – 300 | – 600 |

Table 3.2 Properties of 40% wire reinforced BMG composites in uniaxial compression calculated using FEM in comparison with neutron diffraction data. The data in the last row were obtained in a previous study [9].

3.1.1 Macro Stress-Strain Behavior of Wire Composites

Even though the more detailed ND and modeling analysis was performed on 40% Mo, Fe, and Ta wire-reinforced Vitreloy 106 composites (and presented in Section 3.1.3), the first wire composites had 80% wires due to processing convenience. Such a high volume fraction allowed a close packed configuration of wires and a uniform morphology. Low volume fraction composites sometimes suffer from a nonuniform wire distribution.

Fig. 3.1 illustrates the uniaxial compressive behavior of four 80% wire composites in comparison with that of a monolithic Vit. 106 alloy. (Additional macro curves are presented in Section 3.1.3). It is clear that all composites exhibit enhanced ductility compared to the monolithic Vit. 106. However, this comes at a price of lower yield point, except for the W reinforced composites. The higher yield point of W wires offers a partial explanation for why the W composites exhibit the highest yield point, even higher than that of monolithic Vit. 106. However, a more detailed analysis is necessary to appreciate the subtleties in the behavior of all wire composites. This is presented below, starting with an investigation of the fracture morphology in composites.

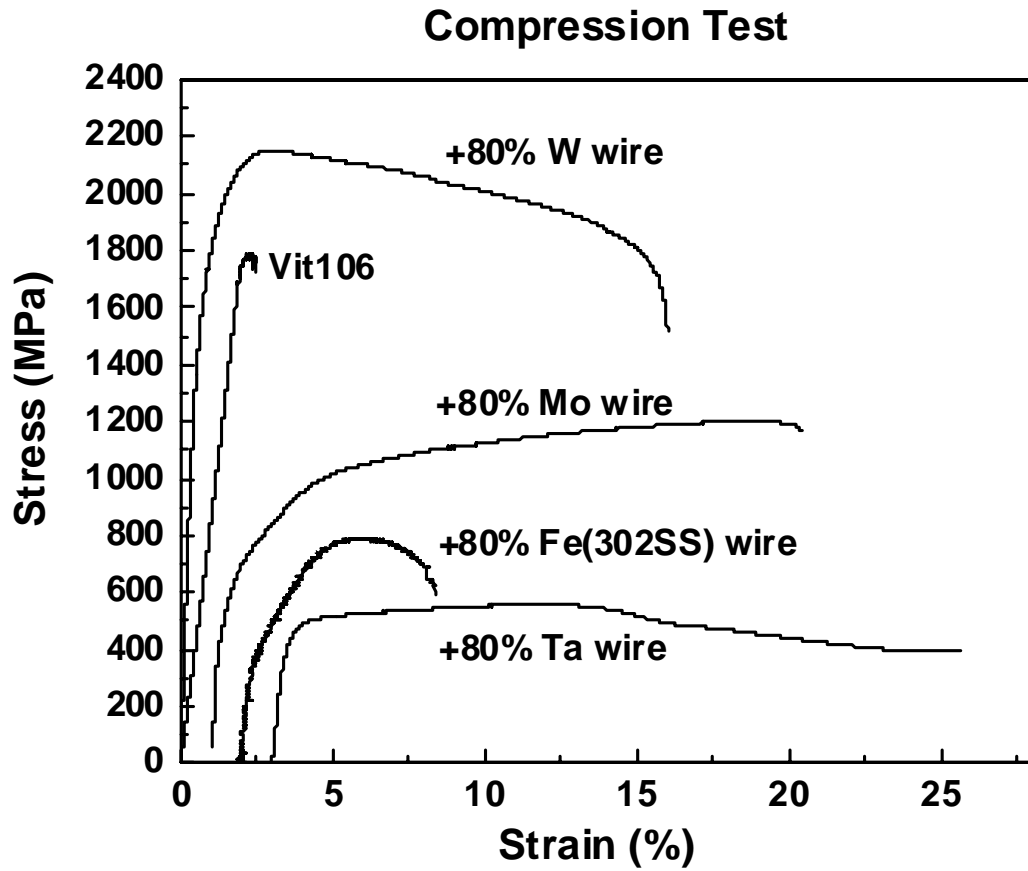
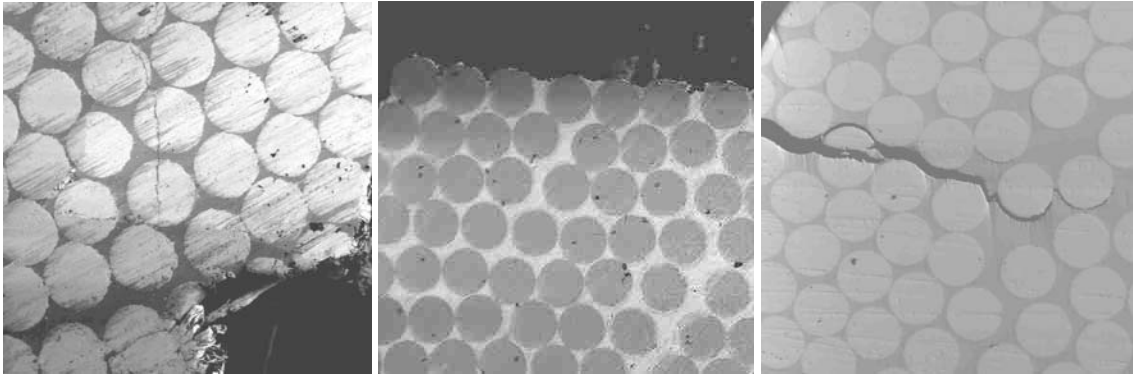


Fig. 3.1 Macro stress-strain curves in uniaxial compression of Vit. 106 matrix, 80% wire reinforced composites. The tests were performed at Caltech by Instron 4204 with a cross head speed of 0.1 mm/min.

3.1.2 Fracture Morphology

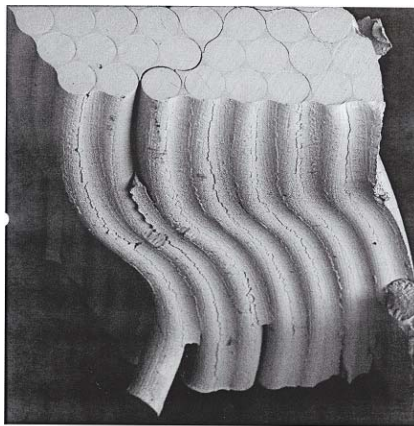
Fig. 3.2 shows the top and side views of composites after fracture or buckling. Based on these images, W wire composite shows the strongest interface strength and it never fails at the boundary, but rather, a crack passes through the wires. On the other hand, the interface of Fe (302 SS) is the weakest and cracks always follow that interface. The weakness of this interface is also proven in processing since it is very difficult to make Fe wire samples because they debond in many cases during machining. Mo seems to be in the middle range because cracks follow mainly the fiber-matrix interface, but it sometimes penetrates the fibers as well. Mo and Ta show buckling, which means large toughness, but also a low yield strength. Based on these qualitative observations, one can conclude that although the Ta composite shows the best performance in cyclic loading without any interface debonding, overall, the W composite is the best choice from a practical point of view due to its high yield strength, relatively high ductility (up to 15%) and strong fiber-matrix interfaces.



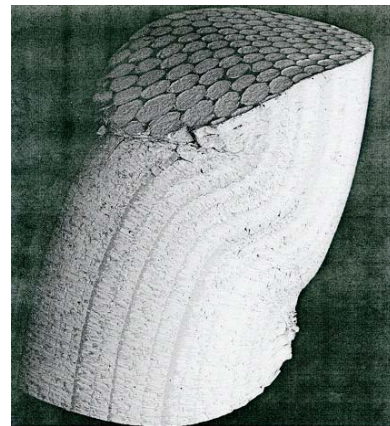
a) W (top view)

b) Fe (SS) (top view)

c) Mo (top view)

600 μ m 37X

d) Mo (side view)



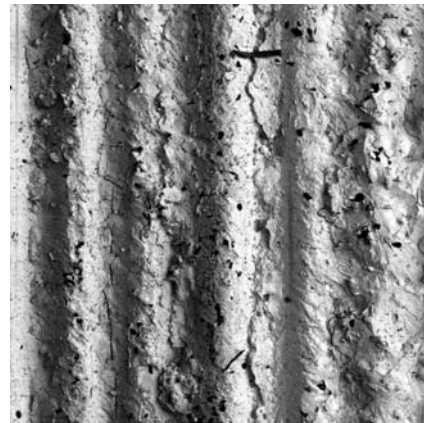
1mm 21X

e) Ta (side view)



1mm 20X

f) W (side view)

400 μ m 60X

g) Fe (SS) (side view)

Fig. 3.2 Fracture morphology of 80% wire composites in top and side view.
Wire diameter is 0.25 mm.

3.1.3 Neutron Diffraction and Finite Element Modeling

Neutron diffraction measurements only record the elastic (lattice) strains; therefore, for a comprehensive interpretation of the composite's deformation, a mechanics model is required. This model is especially essential in this study because the diffraction data are limited to the crystalline wires and measurement of the BMG matrix is not possible due to its amorphous structure. A finite element model was developed for this purpose using the commercial software ABAQUS™ [10]. A three-dimensional mesh was employed to allow loading parallel to the fiber axis (Fig. 3.3). The plane strain assumption was utilized in the model by constraining planes that are perpendicular to the fiber axis to remain planar (Fig. 3.3). Therefore, the model addresses behavior deep beneath the surface of the sample and does not account for surface effects. The calculations employed a unit cell model, and symmetry boundary conditions were imposed on all outer surfaces. Due to the cylindrical shape of the fiber, second order, 20 node, brick elements were used in the mesh, and reduced integration points were employed for speedy calculations. For comparison with the diffraction data which average across the sample cross section, the volume average of elastic strains were calculated for the two phases using the element volume and the “element centroid” value [10] of the elastic strain at each element.

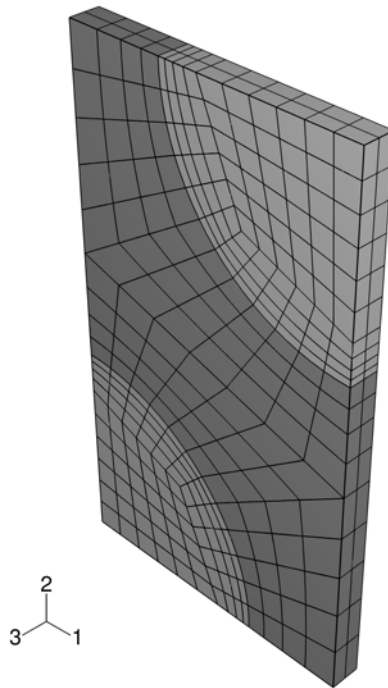


Fig. 3.3 Mesh used in the FEM calculations for a 40% fiber model. The light gray elements represent the fibers while the dark gray elements represent the matrix. The surfaces in the 1-2 planes (perpendicular to the fiber axis) are constrained to remain planar, effectively imposing a plane strain behavior. Loading is applied along direction 3.

The material parameters used in the calculations are shown in Table 3.1. Table 3.2 exhibits the information obtained from the FE calculations. The thermal residual stresses were calculated assuming they are generated starting at the glass transition of Vit. 106 ($\sim 414^{\circ}\text{C}$) [15]. Previous work on W wire composites [9] has shown that in a BMG composite, both the reinforcements and the matrix usually exhibit a different constitutive behavior than in their monolithic forms. Therefore, the *in-situ* yielding and hardening behavior were treated as variables to optimize the agreement between the model and the

experimental data (both lattice strain in the wires from ND, and macroscopic strain in the composite from the extensometer). The FE model employed the kinematic hardening assumption [10] for the wire constitutive behavior to recalculate their hardening during unloading and to account for the reversed yielding observed in the reinforcements upon unloading. The BMG appeared to remain elastic throughout the whole experiment for all three composites and its yield point was determined to be the same as that in the literature (1800 MPa). The fitted values for the *in-situ* yield strengths of the wires, however, did change inside composites and are shown in Table 3.2. The estimated error bars for these fits are about 5%. The resulting phase dependent, *in-situ* stress-strain plots are shown in Fig. 3.4. The reader should note that these plots represent a reasonable solution based on the available data and the assumptions employed in the FEM, but are not necessarily unique in a strict mathematical sense.

Figs. 3.5-3.7 exhibit the experimental data in comparison with model predictions. The stress-strain plots shown in Fig. 3.4 for each phase were deduced as a result of this comparison. As shown in the Table 3.1, since the thermal expansion coefficients of Mo and Ta are smaller than that of the matrix, the Mo and Ta wires are expected to be under compressive stress following sample processing while the BMG experiences tensile axial and hoop stress and compressive radial stress. This residual stress state is predicted to be reversed in the stainless steel composite because of an opposite CTE mismatch between the wires and matrix.

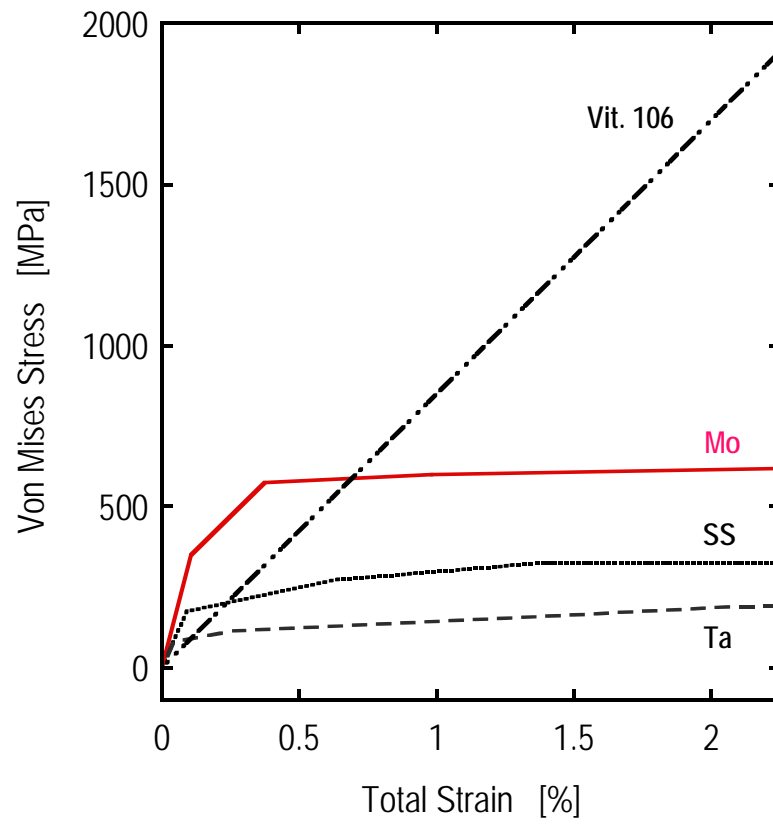


Fig. 3.4 *In-situ* stress-strain behavior for each phase as calculated by the finite element model. These plots were deduced by comparing the experimental data with model predictions.

Due to a lack of proper stress-free reference wires, the thermal residual stresses could not be measured in this study. However, the values calculated (see Table 3.2) based on the assumption that stress buildup starts at the BMG glass transition temperature [8-9] provided reasonable approximations when ND data from loading experiments were compared to model predictions except for the SS composite. The model fits for this composite that included calculated thermal residual stresses were not as satisfactory as those that disregarded such stresses (Fig. 3.6). It was therefore concluded that the thermal residual stresses were largely relaxed in the SS/BMG composite. One possible explanation for this behavior is that the SS/BMG interface in these composites has generally been observed to be weaker than that found in W, Mo and Ta reinforced BMG composites as explained earlier. The predicted tensile radial residual stress at the SS/BMG interface may have aided the relaxation process and even experienced debonding during cooling.

A comparison of FE model predictions and the experimental data suggests that the model is successful in describing the early part of the deformation of all composites and is especially satisfactory for the SS/BMG composite (Figs. 3.5-3.7). In all composites, the wires appear to yield first while the BMG matrix remains elastic throughout the whole deformation (Fig. 3.4). The wires also yield during unloading as indicated by the non-linear unloading curves. Another interesting observation based on the constitutive behaviors presented here (see Fig. 3.4) is that, compared to literature data, the *in-situ* yield strength of the wires has decreased in all three composites (Table 3.2). The decrease is especially pronounced in the Ta wires whose yield strength dropped from 350 MPa to about 80 MPa (compare Tables 3.1 and 3.2). This can be attributed to a probable

annealing of the wires during composite processing, a phenomenon also seen in W/BMG composites [9].

Compared to W reinforced BMG composites, those reinforced with SS, Mo and Ta wires exhibit much lower yield strengths in compression. 40% W/BMG composites started yielding at around -600 MPa [9] (see Table 3.2). In comparison, the axial yield stress in the present composites is -120 MPa for SS, -140 MPa for Mo and -20 MPa for Ta composites (Table 3.2). These values are quite low and suggest that the present composites are not as attractive as those with W wires. Nevertheless, they do enhance the ductility of the BMG matrix and prevent the formation of unstable shear bands. It is also worth noting that due to their much higher Young's modulus (Table 3.1), the SS, Mo and Ta wires carry a higher proportion of the applied stress compared to the BMG matrix and delay the latter's yielding.

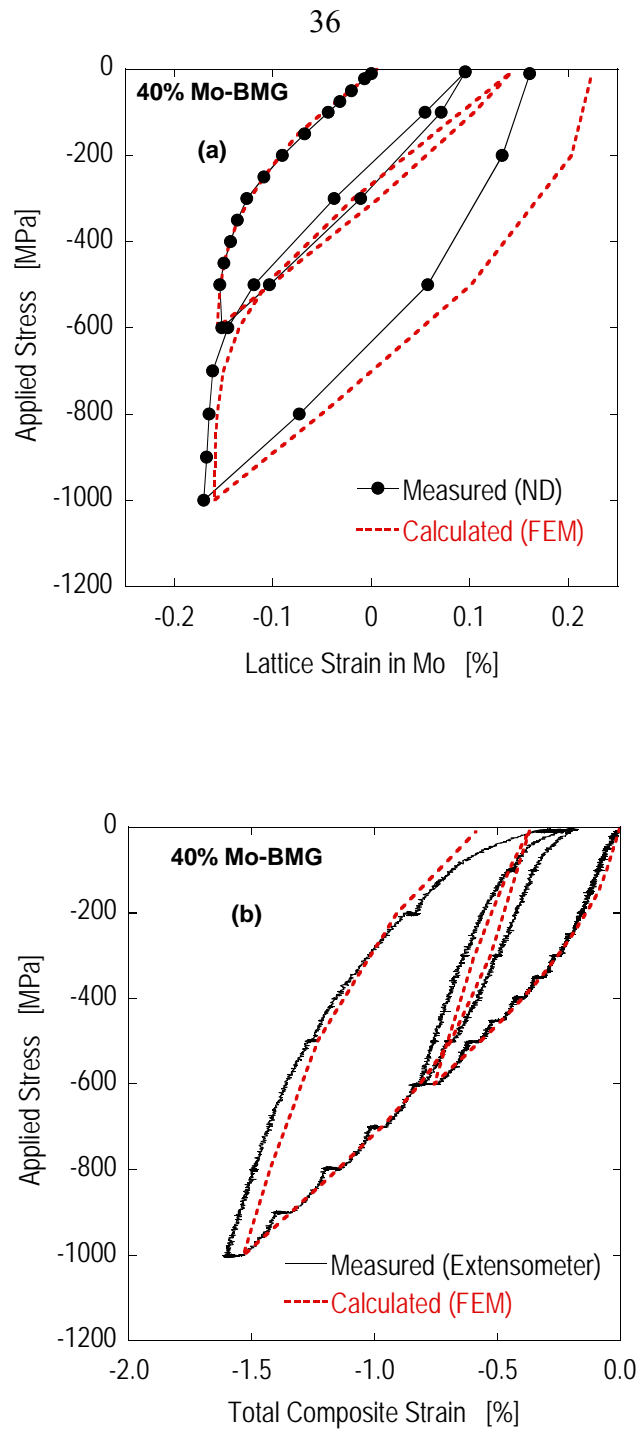


Fig. 3.5 Neutron (a) and macroscopic composite data (b) of the 40% *Mo* - Vit. 106 matrix composite compared with the predictions of the FEM model.

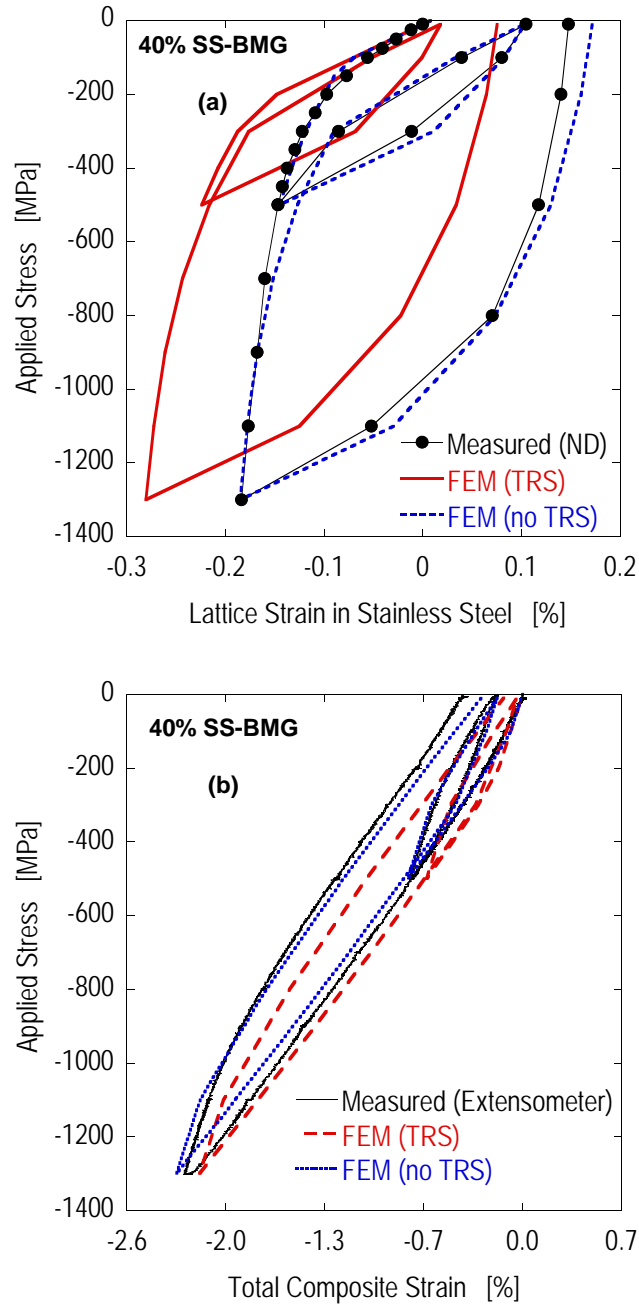


Fig. 3.6 Neutron (a) and macroscopic composite data (b) of the 40% SS (type 302) - Vit. 106 matrix composite compared with the predictions of the FEM model. Two versions of the model are shown: the first version (“TRS”) includes thermal residual stresses while the second one assumes there are no thermal residual stresses (“no TRS”).

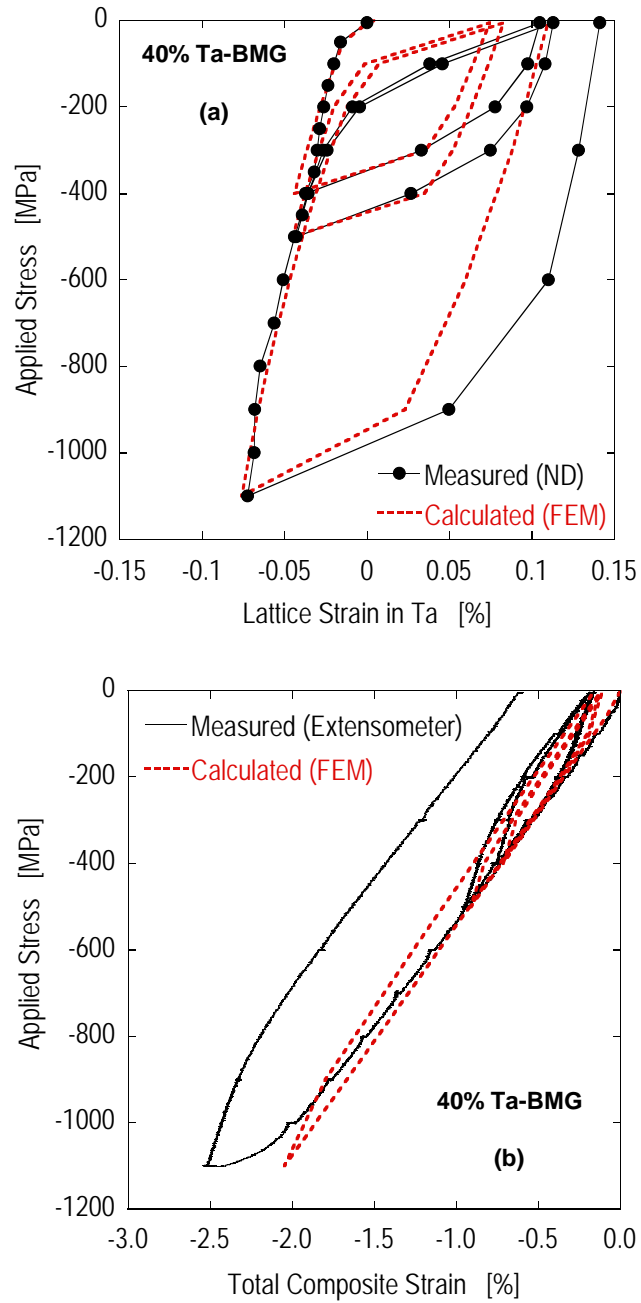


Fig. 3.7 Neutron (a) and macroscopic composite data (b) of the 40% *Ta* - Vit. 106 matrix composite compared with the predictions of the FEM model.

3.2 Tensile Loading of Wire Composites

Tensile test samples of 80% Mo and Ta composites were prepared to compare with their compressive behavior. Those composites showed more than 20% overall ductility in compression with yield strength of about -400 MPa (Fig. 3.1). Referring to data presented in Tables 3.1 and 3.2, one would expect compressive thermal residual stresses in Mo and Ta wires after casting due to their lower CTE compared to that of the BMG matrix. As a result, a tension test would normally exhibit a higher yield strength as applied tensile stress has to first overcome the compressive residual stresses in the wires before initiating yielding in them. Before reviewing the results of the tension tests on 80% composites, it is important to note that the thermal residual stress in the wires of these composites would be lower (due to the higher wire fraction) than that found in the 40% composites.

The results of the tension tests performed on 80% Mo and Ta composites are exhibited in Fig. 3.8. Both composites yielded at lower stresses compared to those seen in the compression tests (see Fig. 3.1). Fig. 3.8 also shows an interesting phenomenon called “fiber pull out” in the Mo composites. Specifically, Mo wires appear to pull out of the matrix due to the relatively weak interface between the two. This is seen as stress drops in the stress-strain curve and is further illustrated in the sample images shown in Fig. 3.9 (a). Fiber pull out is a well known toughening mechanism in brittle matrix composites as it significantly increases the fracture energy. Unfortunately, fiber pull out might lower the probability of multiple shear band formation in the BMG matrix, hence, preventing any further enhancement of the composite ductility. This result, therefore, suggests once

again the need for a relative strong interface between the reinforcements and BMG matrices to attain high ductility and toughness.

Fig. 3.9 (b) shows the Ta composite after the tension test. Here, necking around fracture region is observed and plastic deformation of the matrix can be inferred, but Ta composites are not attractive for structural applications due to their low yield strength despite their relatively strong fiber-matrix interfaces.

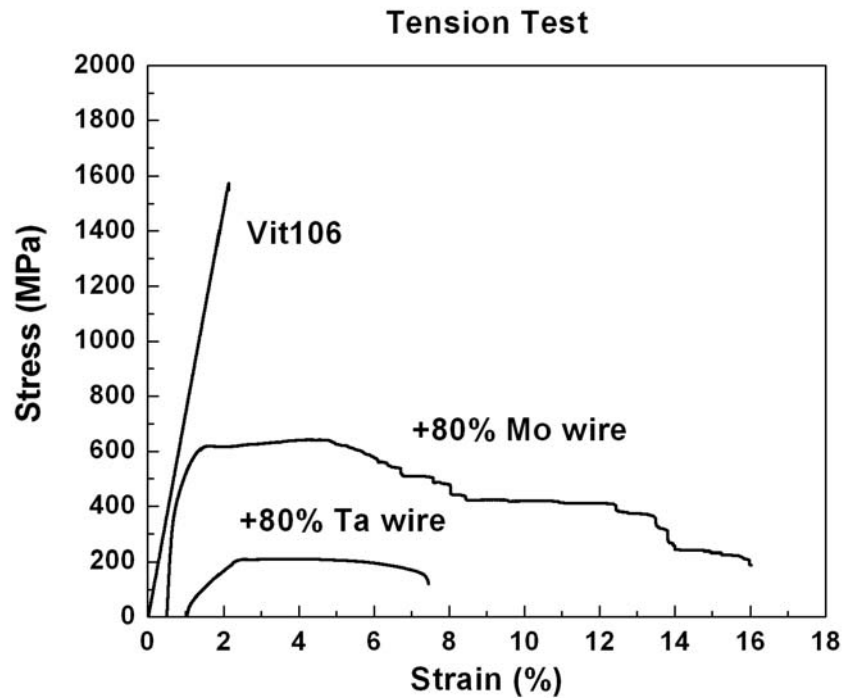


Fig. 3.8 Macro uniaxial tensile stress-strain curves for Mo and Ta 80% wire composites.



(a) Mo 80%



(b) Ta 80%

Fig. 3.9 Fracture images of Mo and Ta 80% composites after the tension test. Fiber pull-out and necking are observed in Mo and Ta, respectively.

3.3 Conclusions

In an attempt to develop bulk metallic glass (BMG) composites with enhanced ductility, stainless steel (SS), Mo and Ta wires were incorporated in a BMG matrix via a melt infiltration process. The deformation of the three composites under uniaxial compression was studied using an integrated neutron diffraction and finite element (FE) approach. The FE model yielded a reasonable version of *in-situ* stress-strain plots for both reinforcements and the matrix. It was found that the reinforcements yielded first and started transferring load to the matrix which remained elastic throughout the whole experiment. The reinforcements were seen to possess yield strengths lower than their monolithic forms, likely due to annealing during processing. After optimizing material properties to fit experimental data, the FE model developed was reasonably successful in describing both the macroscopic composite deformation and the lattice strain evolution in the reinforcements.

Additional experiments were performed in tension using 80% Ta and Mo composites. Both materials exhibited lower yield points in tension compared to those in compression. Furthermore, the Mo composite underwent extensive fiber pull out due to the relatively weak fiber-matrix interface. These results, combined with an analysis of the fracture morphology of all composites, allow the following conclusions re. the “optimum” wire reinforcement for BMG composites: (i) high yield strength (but preferably lower than that of the matrix); (ii) high stiffness (so that it can carry most of the applied load); (iii) good ductility (so that it can experience significant plastic deformation and trigger multiple shear banding in the BMG matrix); and (iv) relatively strong fiber-matrix interface (to allow effective load transfer). Based on these criteria, the W wires appear to be the closest to approach the “ideal” wire reinforcement; however, they still suffer from inadequate ductility. In this regard, the β phase found in *in-situ* composites described in the next chapter offer more options in terms of both microstructure control and reinforcement property optimization.

References

- [1] C. J. Gilbert, R. O. Ritchie, W. L. Johnson, *Appl. Phys. Lett.* 71 (1997) 476.
- [2] W. L. Johnson, *JOM-J. Miner. Met. Mater. Soc.* 54 (2002) 40.
- [3] H. A. Bruck, T. Christman, A. J. Rosakis, W. L. Johnson, *Scr. Metall.* 30 (1994) 429.
- [4] R.D. Conner, R. B. Dandliker, V. Scruggs, W. L. Johnson, *Int. J. Impact. Eng.* 24 (2000) 435.
- [5] R. D. Conner, R. B. Dandliker, W. L. Johnson, *Acta Mater.* 46 (1998) 6089.
- [6] H. Choi-Yim, W. L. Johnson, *Appl. Phys. Lett.* 71 (1997), 3808.
- [7] H. Choi-Yim, R. Busch, U. Köster, W. L. Johnson, *Acta Mater.* 47 (1999) 2455.
- [8] D. Dragoi, E. Üstündag, B. Clausen, M. A. M. Bourke, *Scripta Mater.* 45 (2001) 245.
- [9] B. Clausen, S.-Y. Lee, E. Üstündag, C. C. Aydiner, R. D. Conner, M. A. M. Bourke, *Scripta Mater.* 49 (2003) 123.
- [10] ABAQUS, Standard User's Manual, version 6.3, Hibbitt, Karlsson & Sorensen, Inc. 2002.
- [11] H. E. Boyer, T. L. Gall, *Handbook of Stainless Steels*, American Society for Metals, New York, NY, 1977, pp. 19-7.
- [12] Y. S. Touloukian, R. K. Kirby, R. E. Taylor, P. D. Desai, *Thermophysical Properties of Matter, Vol. 12: Thermal Expansion, Metallic Elements and Alloys*, IFI/Plenum, New York, NY, 1977, pp. 208, 316, 354.
- [13] H. Choi-Yim, R. D. Conner, W. L. Johnson, *Ann. Chim. Sci. Mat.* 27 (2002) 113.
- [14] D. R. Lide, *Handbook of Chemistry and Physics*, 82nd Edition, CRC Press, Boca Raton, FL, 2001, pp. 12-220.
- [15] J. F. Löffler, S. Bossuyt, S. C. Glade, W. L. Johnson, W. Wagner, P. Thiyagarajan, *Appl. Phys. Lett.* 77 (2000) 525.

CHAPTER 4

RESULTS AND DISCUSSION:

MECHANICAL BEHAVIOR AND MODELING

OF *IN-SITU* β PHASE COMPOSITES

4.1 *In-situ* Composite Development and Characterization

4.1.1 Background: Development of LM2 *In-situ* Composites

Ever since A. Peker and W. L. Johnson developed the $Zr_{41.2}Ti_{13.8}Cu_{12.5}Ni_{10}Be_{22.5}$ (Vitreloy 1) bulk metallic glass with a critical cooling rate of about 1K/s in 1993 [1], Caltech has investigated many other BMG systems such as $Cu_{47}Ti_{34}Zr_{11}Ni_8$, (Vitreloy 101), $Zr_{52.5}Ti_5Cu_{17.9}Ni_{14.6}Al_{10}$ (Vitreloy 105), and $Zr_{57}Nb_5Cu_{15.4}Ni_{12.6}Al_{10}$ (Vitreloy 106), with a critical cooling rate of about 10 K/s [2-3]. At the same time, several different kinds of composites with wire and particulate reinforcements have been processed and have successfully shown a significant improvement of ductility [4-5]. In 1999, C. P. Kim and W. L. Johnson at Caltech developed the $Zr_{56.2}Ti_{13.8}Nb_{5.0}Cu_{6.9}Ni_{5.6}Be_{12.5}$ *in-situ* composites (named LM2 by Liquid Metal Technologies) while searching for new BMG systems near $Zr_{41.2}Ti_{13.8}Cu_{12.5}Ni_{10.0}Be_{22.5}$ (Vitreloy 1, also called LM1). Due to chemical partitioning during casting, these composites end up with an amorphous matrix similar to Vitreloy 1 and a dendritic BCC crystalline phase (called the β phase). Such *in-situ* composites are attractive since they allow microstructure control and avoid interface reactions seen in most *ex-situ* composites. Figs. 4.1 to 4.3 are reproduced from C. P. Kim's Ph.D. thesis and offer phase diagram, microstructure and mechanical property information about these composites.

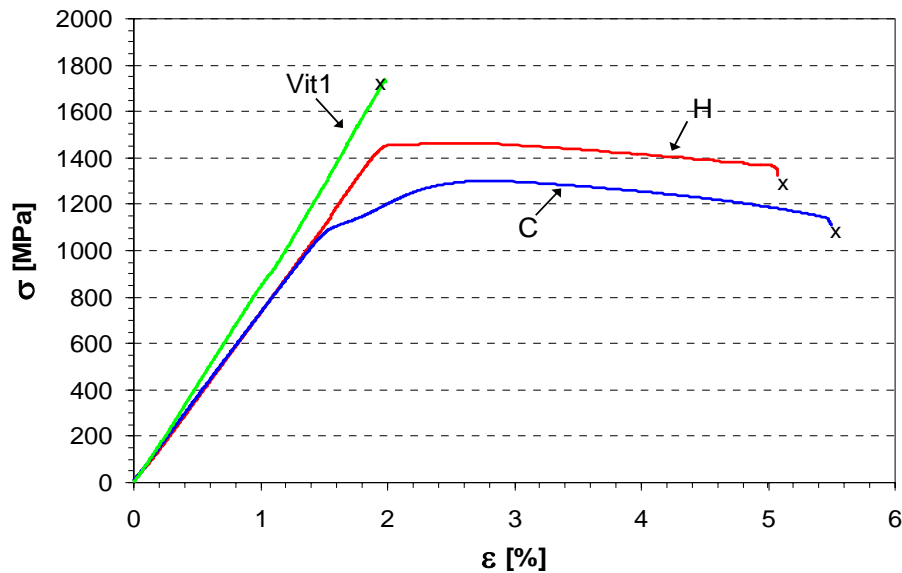


Fig. 4.3 Tensile stress-strain curves of two *in-situ* composites compared to that of Vit. 1. C represents the composite made at Caltech, and H labels the composite made by the Howmet Corporation. The finer dendrite size in the latter composite leads to a higher yield strength [6].

It is clear from Fig. 4.3 that the *in-situ* composites possess significant ductility compared to a monolithic BMG while retaining most of its high yield strength. Fig. 4.2 and Fig. 4.3 also imply that composites processed at higher cooling rates have finer dendritic structures leading toward a higher yield strength. This observation, in turn, suggests a unique opportunity to manipulate composite properties by optimizing processing conditions. The present study undertook a systematic effort to relate microstructure to processing conditions by investigating a wide range of composites. The details of microstructure analyses are illustrated in Chapter 5 while this chapter presents the effects of processing on mechanical properties and elastic constants.

Here, it is important to note that while earlier work on these composites suggested a dendrite volume fraction of 25% [6], a more precise digital image analysis performed in the present study yielded a value of 40%. This number was obtained from the average of 40 different micrograph analyses which had a standard deviation of 3.56%. The corrected value was employed in the chemical composition analyses.

| Sample | Composition [at.%] | Phase | E [GPa] | G [GPa] | ν |
|---------|---|-----------|---------|---------|-------|
| Vit1 | $Zr_{41.2}Ti_{13.8}Cu_{12.5}Ni_{10}Be_{22.5}$ | BMG | 97.2 | 35.9 | 0.355 |
| C and H | $Zr_{56.2}Ti_{13.8}Nb_{5.0}Cu_{6.9}Ni_{5.6}Be_{12.5}$ | BMG + bcc | 78.8 | 28.6 | 0.375 |
| M | $Zr_{47}Ti_{12.9}Nb_{2.8}Cu_{11}Ni_{9.6}Be_{16.7}$ | BMG | 89.2 | 32.6 | 0.369 |
| B | $Zr_{71}Ti_{16.3}Nb_{10}Cu_{1.8}Ni_{0.9}$ | bcc | 63.3 | 22.7 | 0.401 |

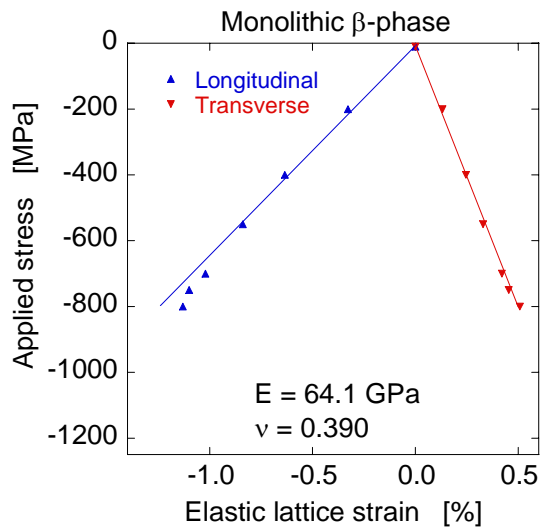
Table 4.1 Composition and elastic constants of LM2 *in-situ* composites from ref. [6]
C: composite made at Caltech; H: composite made at Howmet; M: amorphous matrix; B: BCC dendrite. (E: Young's modulus; G: shear modulus; ν : Poisson's ratio).

Table 4.1 exhibits the elastic constants along with the composition of each phase in the early LM2 composites in comparison with Vit. 1. Composition analyses were performed by a JEOL JXA-73 electron microprobe, which does not detect low Z elements such as Be. To obtain the Be content, a common practice is to calculate it from the balance of all the other elements so that a total of 100% is reached for the composition of a given phase. In the wavelength dispersive spectroscopy (WDS) analysis performed with the microprobe, the total composition of all the other elements was very close to 100% in the β phase, so it was assumed that no Be exists in this phase. As for the matrix, the Be content (16.7%) was calculated from the balance of the other elements.

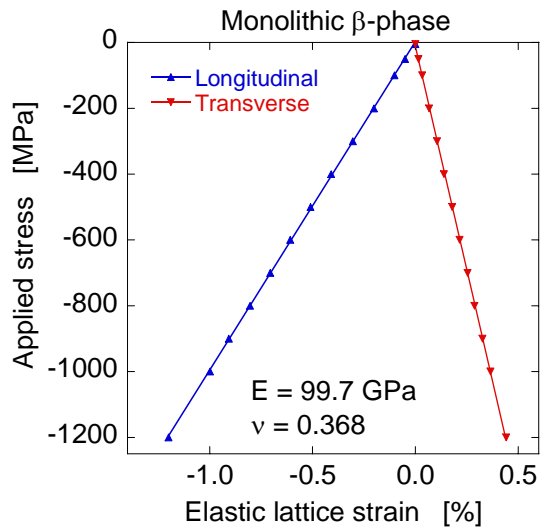
However, this analysis assumed a wrong value for the volume fraction of the matrix (75% instead of the correct value of 60% determined in the present study). Therefore, a new balance calculation was performed to obtain 20.8% Be in the matrix, resulting in an accurate composition of $Zr_{44.7}Ti_{12.2}Nb_{2.7}Cu_{10.5}Ni_{9.1}Be_{20.8}$, which is very close to the composition of Vit. 1 (except for the Nb) and proves once again the similarity between the matrix in β phase composites and Vit. 1.

Following the development of the LM2 composites, Clausen *et al.* utilized neutron diffraction to investigate the deformation of these composites and the monolithic β phase prepared as a reference [7]. In order to estimate the thermal residual stresses in the composites, they also performed CTE measurements on the monolithic β phase in a dilatometer with a heating rate of $3^{\circ}C /min$ up to $350^{\circ}C$. The sample was cooled down after being held at $350^{\circ}C$ for 30 minutes at the same rate used during heating. When this heat-treated β phase sample was loaded during neutron diffraction, an unexpected behavior was observed: the specimen stiffened over 50% while becoming extremely brittle (Fig. 4.4).

While the as-cast monolithic β phase started to yield around 600 MPa and had a Young's modulus of 64 GPa, it stiffened up to 100 GPa and remained elastic throughout loading after the heat treatment. This unexpected behavior triggered a systematic study of the deformation behavior and phase evolution in β phase composites presented in this thesis. Overall mechanical properties are discussed in Chapter 4, and phase evolution and microstructure are explained in Chapter 5 in more detail.



(a) Before CTE measurement



(b) After CTE measurement

Fig. 4.4 Neutron diffraction data of monolithic β phase before and after CTE measurement up to 350°C. The Young's modulus jumps from 64 to 100 GPa while the material becomes brittle. The neutron diffraction patterns are shown in Fig. 5.9.

4.1.2 System Optimization and Physical Properties of LM2A2 *In-situ* Composites

Following the development of the LM2 ($Zr_{56.2}Ti_{13.8}Nb_{5.0}Cu_{6.9}Ni_{5.6}Be_{12.5}$) *in-situ* composites, Liquid Metal Technologies continued new composite development and arrived at LM2A2 ($Zr_{56.2}Ti_{11.3}Nb_{7.5}Cu_{6.9}Ni_{5.6}Be_{12.5}$) as a better material. The only compositional difference between LM2 and LM2A2 is in the Ti and Nb content (5% vs. 7.5% Nb at the expense of Ti). Despite this small difference, the thermal stability and ductility of LM2A2 surpass those of LM2 significantly. For example, as shown in Fig.4.5, the ductility increased to 14% from 8% total strain while maintaining the same level of yield strength above 1400 MPa.

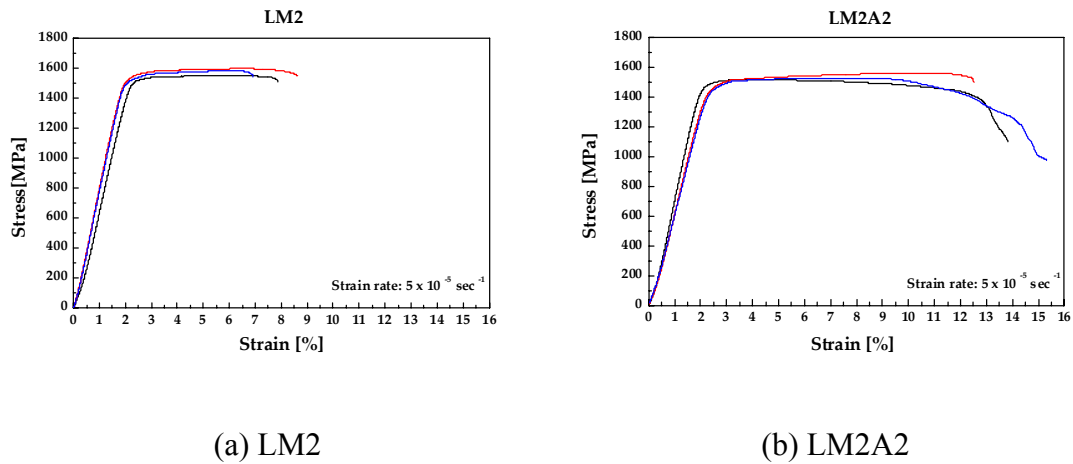


Fig. 4.5 Compressive tests of LM2 (~8% total strain) and LM2A2 (~14% total strain) *in-situ* composites (courtesy of Liquid Metal Technologies).

In the present study, the LM2A2 ($Zr_{56.2}Ti_{11.3}Nb_{7.5}Cu_{6.9}Ni_{5.6}Be_{12.5}$) composite was used for heat treatment and mechanical tests. Here, in addition to the composite, monolithic β phase and monolithic glass samples were studied as reference materials for the reinforcement and matrix, respectively. Their compositions were determined by an electron microprobe analysis of the composite. A minimum of six different locations were probed in each phase of the composite to arrive at the data displayed in Table 4.2 below. As with LM2, the Be content was determined by balance. Note that the β phase contains no Be since the total of the other elements approached 100%. As for the matrix, the measured volume fractions of each phase (40% for the reinforcements and 60% for the matrix) were used to calculate its composition from the conservation of mass principle. Notice that the matrix composition ($Zr_{42.2}Ti_{9.4}Nb_{3.2}Cu_{13.7}Ni_{10.7}Be_{20.6}$) is quite similar to that of Vitreloy 1 (Table 4.2) except for the Nb. It is not surprising, therefore, that the elastic constants of the matrix material are also close to those of Vitreloy 1.

| Sample | Composition [at.%] | Phase | E [GPa] | G [GPa] | ν |
|---------------|--|------------------|----------------|----------------|-------------------------|
| Vit1 | $Zr_{41.2}Ti_{13.8}Cu_{12.5}Ni_{10}Be_{22.5}$ | BMG | 97 | 36 | 0.36 |
| C | $Zr_{56.2}Ti_{11.3}Nb_{7.5}Cu_{6.9}Ni_{5.6}Be_{12.5}$ | BMG + bcc | 78 | 28 | 0.37 |
| M | $Zr_{42.2}Ti_{9.4}Nb_{3.2}Cu_{13.7}Ni_{10.7}Be_{20.8}$ | BMG | 95 | 35 | 0.36 |
| B | $Zr_{71.1}Ti_{13.1}Nb_{13.4}Cu_{1.6}Ni_{0.8}$ | bcc | 62 | 22 | 0.40 |

Table 4.2 Composition and elastic constants of LM2A2 *in-situ* composites and the corresponding monolithic versions of its components. (C: composite; M: monolithic matrix glass; B: monolithic β phase alloy).

4.2 Tensile and Compressive Stress-Strain Behavior of LM2A2 Composites

4.2.1 Tensile Tests of Heat Treated LM2A2

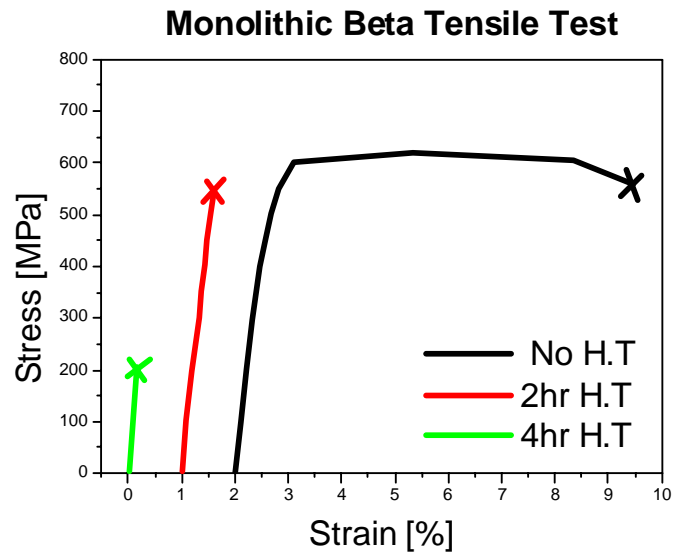


Fig. 4.6 Tensile stress-strain plots of monolithic β phase heat treated at 300°C.

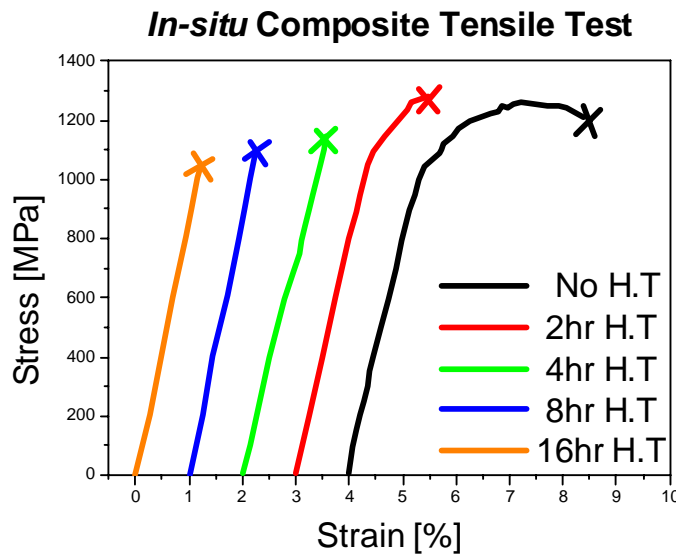


Fig. 4.7 Tensile stress-strain plots of β phase composite heat treated at 300°C.

Figs. 4.6 and 4.7 show tensile stress-strain curves for monolithic β phase and composite, respectively, as a function of heat treatment at 300°C. These figures were obtained directly from an extensometer attached to samples during *in-situ* synchrotron diffraction experiments at APS. It is clear that as heat treatment holds increase, there is a gradual reduction of ductility in both the monolithic β phase and the composite.

Synchrotron diffraction data of all heat treated composites show peak broadening of the BCC peaks from the reinforcement, and indicate no crystallization of the matrix. As will be explained in more detail in Chapter 5, it is reasonable to conclude that the observed dramatic changes in the composite behavior as a function of heat treatment are mostly due to changes in the reinforcement. Specifically, it appears that when the β phase becomes more brittle, so does the composite. This observation suggests an important conclusion that the inherent ductility of the reinforcement is crucial for the overall composite ductility and may be even more important than the geometric effect of shear band blocking in the matrix by β phase dendrites. Some preliminary work was performed to image the interactions between matrix shear bands and dendritic reinforcements (see Figs. 4.8 – 4.10). The shear bands appear to run between dendrites and are somehow multiplied due to a combined effect of yielding in the dendrites and their geometric constraint on the matrix. It is shown below that the β phase yields first and then triggers shear banding in the matrix, but the micromechanical details of this process are not well understood at the moment. This is suggested as an important future study since it is important to fully appreciate the micromechanical deformation mechanisms in these composites before their properties can be further enhanced.

One last comment before concluding this section: The embrittlement of β phase composites during heat treatment appears to be more severe in tension compared with compression, confirming the general trend observed in these BMG composites (as well as others) that they are usually more ductile in compression. While some composites were later discovered to contain processing-induced pores that act as stress concentrators (such as the β phase composites quenched in water or cast in a Cu mold), the overall lack of tensile ductility is still an important problem to address in BMG composites.

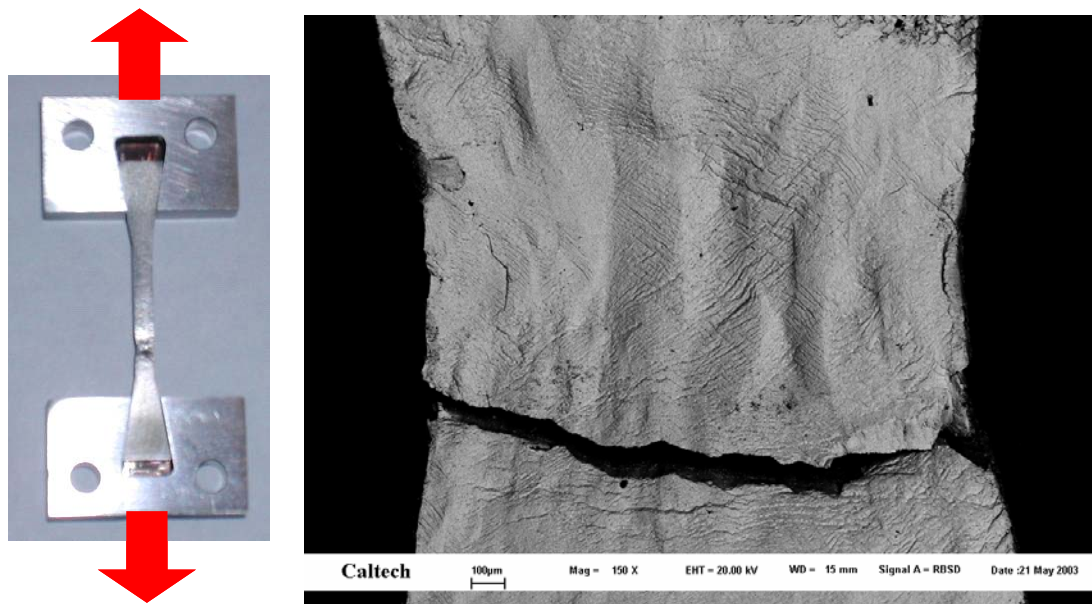


Fig. 4.8 Tensile sample geometry and fracture image of an as-cast β phase composite after necking in the middle of sample.

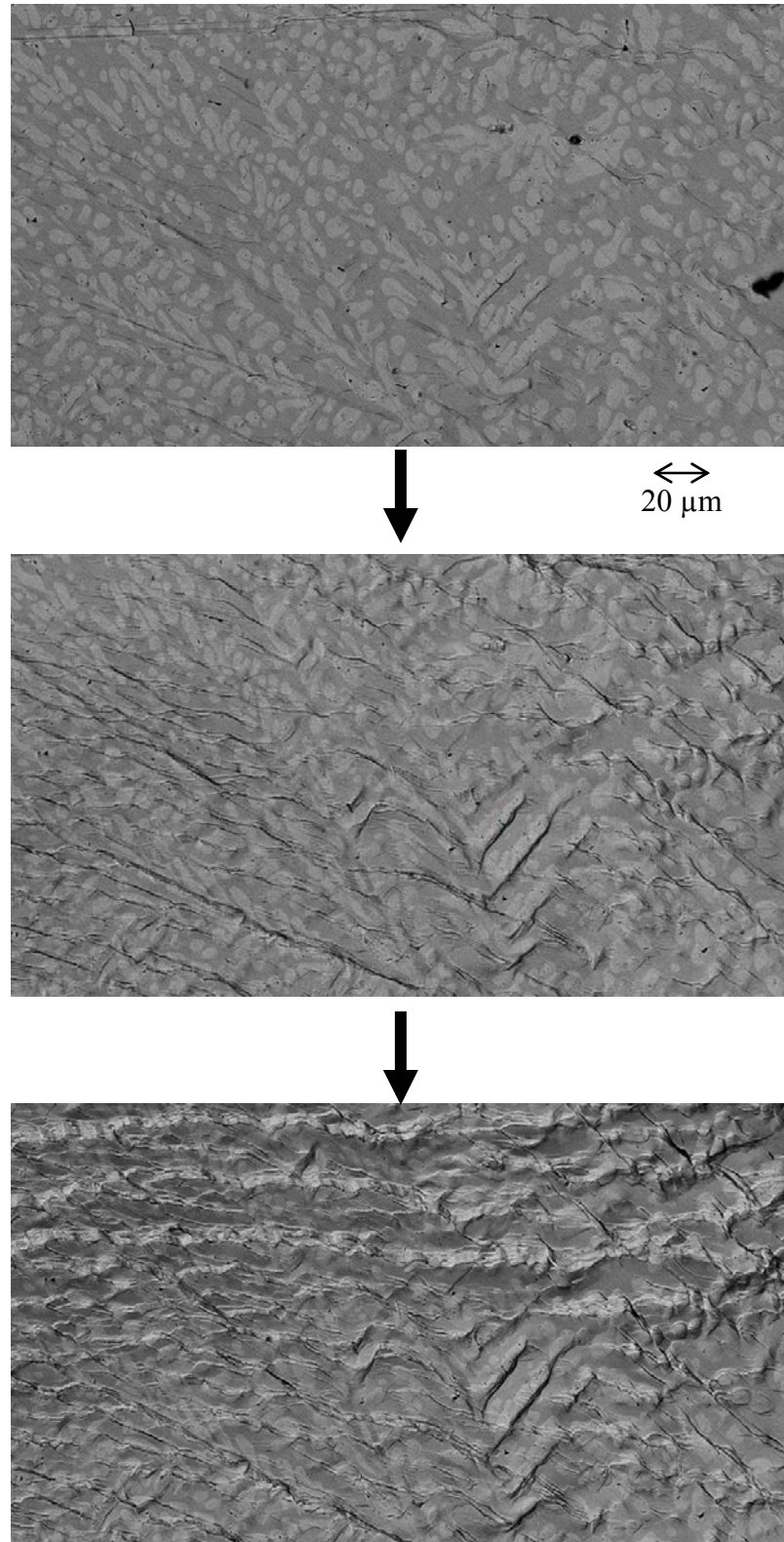


Fig. 4.9 Successive SEM images taken from the same region of the tensile test sample shown in Fig. 4.8. Shear bands are visible as dark lines.

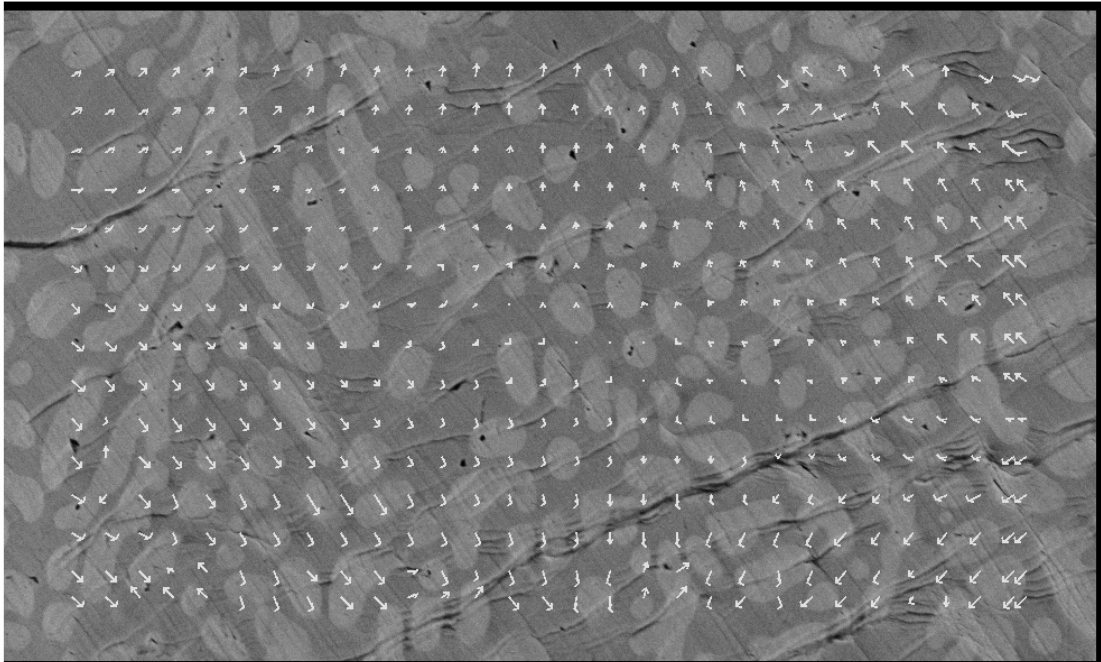


Fig. 4.10 Surface displacement field in the deformed β phase composite shown in Fig. 4.9 obtained from digital image processing (in collaboration with Rockwell Scientific). Although the resolution is limited, the image suggests a general tendency of vertical deformation (along the loading direction) and some Poisson effect.

4.2.2 Compressive Tests of Heat Treated LM2A2

Compressive tests were performed on a screw-driven load frame (Instron 4204) at Caltech. The results are illustrated in Figs. 4.11 – 4.14. Figs. 4.11 and 4.12 show a similar trend with heat treatment as that observed in tensile tests: both the monolithic β phase and composite samples became more brittle as the heat treatment holds increased. Note that the as-cast versions of both samples were quite ductile and did not fracture during the tests despite significant deformation (Fig. 4.14). In order to ensure that the embrittlement is purely a reinforcement effect, monolithic glass samples (of the same composition as that found in the matrix) were heat treated at 340°C and tested under compression (Fig. 4.13). Those tests yielded virtually identical results and showed no embrittlement of the glass. Additional X-ray diffraction confirmed that there was no crystallization. It can be concluded, therefore, that heat treatment led to embrittlement in composites, and that this is largely due to the embrittlement of the β phase reinforcements.

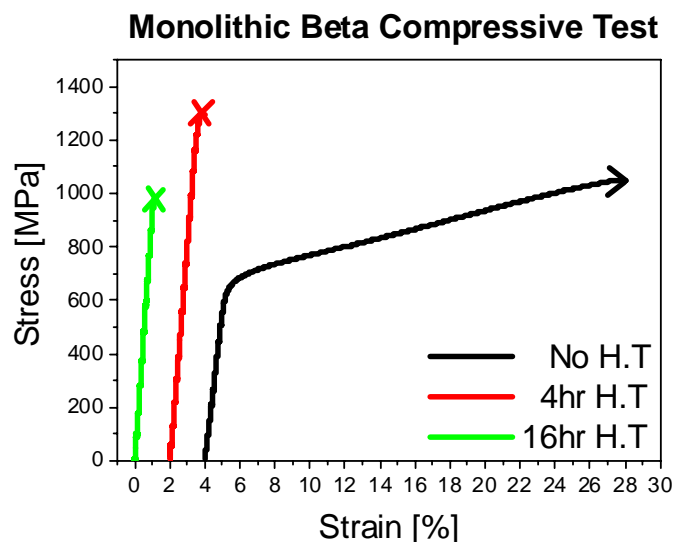


Fig. 4.11 Compressive stress-strain curves of monolithic β phase heat treated at 340°C. Note that the as-cast specimen did not fracture during the test.

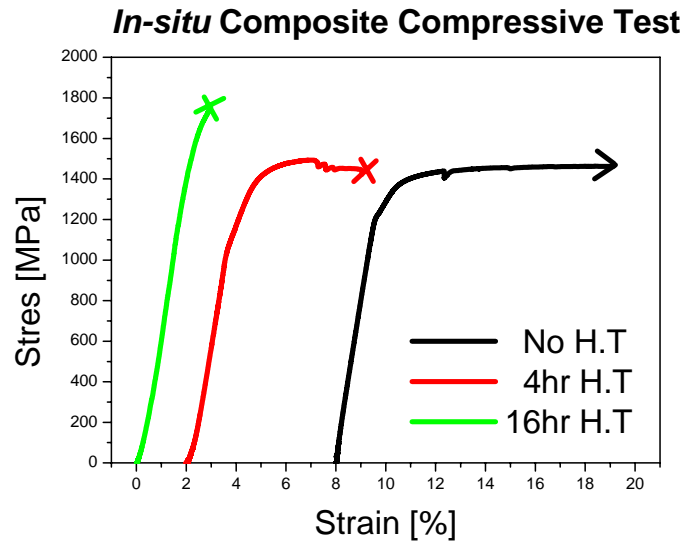


Fig. 4.12 Compressive stress-strain plots of β phase composites heat treated at 340°C. Here the as-cast specimen did not fracture in the duration of the test.

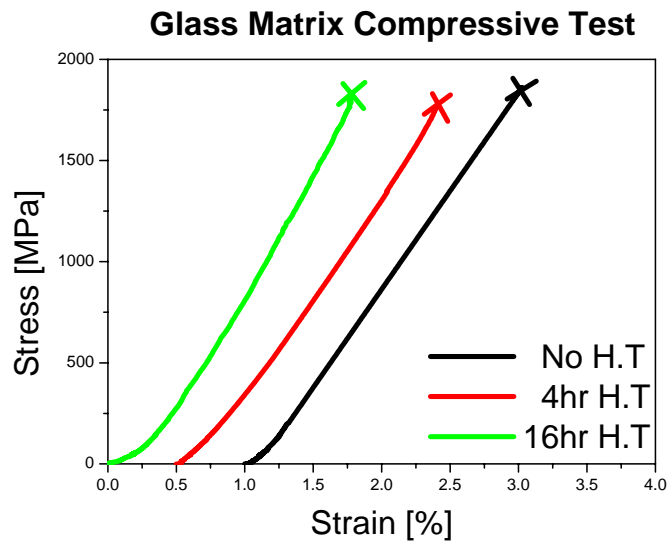


Fig. 4.13 Compressive stress-strain curves of monolithic glass heat treated at 340°C.



Fig. 4.14 Compression samples (6 mm diam. x 14.4 mm length) after testing (left to right): as-cast monolithic β phase, same material after 16 hr HT, as-cast composite, and the same material after 16 hr HT.

4.2.3 Ultrasonic Sound Velocity Measurement of Elastic Constants

To quantify another important property evolution during heat treatment, all samples mentioned above were subjected to ultrasonic tests to measure their elastic constants. The results are listed in Tables 4.3 – 4.5. The shear modulus of the β phase increased from 22 GPa to 32 GPa (a 45% increase), while that of the composite changed from 27 GPa to 33 GPa (a 22% increase). Similar changes were also seen in the Young's modulus, whereas the Poisson's ratio remained largely constant or decreased slightly in both samples. On the other hand, heat treatment had less effect on the elastic constants of the monolithic glass matrix.

Therefore, it can be concluded that the stiffening of the composite can mostly be attributed to the stiffening of the reinforcement. This result is similar to the effects of heat treatment on ductility, and once again, proves that dramatic changes in the β phase reinforcement are leading to significant changes in the mechanical properties of the composite during heat treatment.

| | No H.T. | 4 hr H.T. | 16 hr H.T. |
|---|-------------|-------------|-------------|
| G (Shear Modulus, GPa) | 22 | 28 | 32 |
| E (Young's Modulus, GPa) | 62 | 78 | 88 |
| ν (Poisson's ratio) | 0.40 | 0.38 | 0.37 |

Table 4.3 Ultrasonic sound velocity measurements of the elastic constants of monolithic β phase as a function of heat treatment at 340°C.

| | No H.T. | 4 hr H.T. | 16hr H.T. |
|---|-------------|-------------|-------------|
| G (Shear Modulus, GPa) | 27 | 30 | 33 |
| E (Young's Modulus, GPa) | 74 | 83 | 89 |
| ν (Poisson's ratio) | 0.39 | 0.37 | 0.36 |

Table 4.4 Ultrasonic sound velocity measurements of the elastic constants of *in-situ* composites as a function of heat treatment at 340°C.

| | No H.T. | 4 hr H.T. | 16 hr H.T. |
|---|-------------|-------------|-------------|
| G (Shear Modulus, GPa) | 36 | 37 | 37 |
| E (Young's Modulus, GPa) | 98 | 99 | 101 |
| ν (Poisson's ratio) | 0.36 | 0.36 | 0.36 |

Table 4.5 Ultrasonic sound velocity measurements of the elastic constants of monolithic glass as a function of heat treatment at 340°C.

4.3 *In-situ* Loading Experiments

4.3.1 Compressive Loading Behavior during Neutron Diffraction of As-cast Specimens

4.3.1.1 Introduction

In this section, a detailed investigation of the deformation mechanisms in β phase composites is presented. First, relevant previous work is reviewed. The dendritic structure of the β phase has been shown to inhibit the formation of macroscopic shear bands in the matrix which cause sudden failure in monolithic BMGs. The mechanical properties of the BMG/ β phase composites have previously been characterized via macroscopic measurements, such as determination of elastic constants by ultrasound and conventional tension and compression, as well as Charpy impact testing [8-10]. It was found that the β phase leads to the formation of multiple shear bands in the BMG matrix with a similar spacing to that of the secondary dendrites in the β phase. However, neither the underlying deformation mechanisms nor the load sharing in the composite could be determined in these studies. There was some speculation that plastic deformation via dislocation slip, twinning or a stress-induced phase transformation in the β phase might play a role. Since the β phase composites offer an attractive venue to manipulate microstructure and optimize the mechanical properties of BMG matrix composites, it is important to understand their effective deformation mechanisms.

In the present study, neutron diffraction was used, aided by self-consistent modeling, to investigate the *in-situ* deformation of a BMG/ β phase composite and a β phase monolith during compressive loading. Neutron diffraction allows for *in-situ* bulk measurements of internal strains in crystalline materials [11-12], and is ideal for

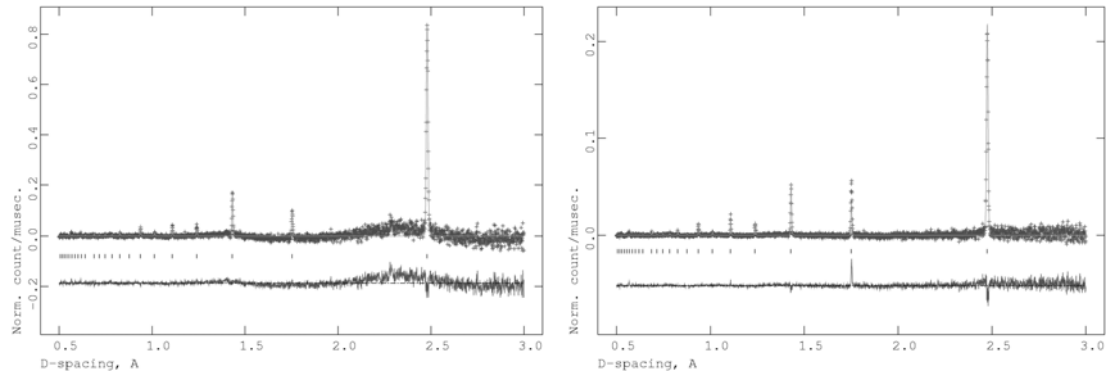
composite systems as it is phase specific. Although the amorphous nature of BMG precluded its analysis by Bragg diffraction, the crystalline β phase could be used as an internal “strain gauge.” Then, by combining the diffraction data for the β phase with model predictions of the composite behavior, it was possible to infer the *in-situ* behavior of the BMG matrix. Moreover, the neutron diffraction data could identify the nature of the deformation mechanism in these composites.

4.3.1.2 Experimental Procedure

Specimens were prepared by alloying high purity Cu (99.999 %), Ni (99.995 %), Ti (99.995 %), (all from Cerac, Inc., Milwaukee, WI 53201), Nb (99.8 %, from Alfa Aesar, Ward Hill, MA 01835), Zr (with less than 300 ppm oxygen content from Teledyne Wah-Chang Inc., Albany, OR 97321), and Be (99.99 %, from Electronic Space Products International, Ashland, OR 97520). The alloys were prepared as 25 g rods of roughly cylindrical geometry by plasma arc melting in a Ti-gettered argon atmosphere on a water-cooled copper plate. The molten alloy was then undercooled to a temperature range between the liquidus and solidus for a given composition [8]. This led to the chemical partitioning of the undercooled liquid into a solid (crystalline metal dendrites - the β phase, about 40 vol.%) and a liquid phase with a different composition. The liquid phase, depleted of the elements going into the β phase, attained the composition of a BMG forming alloy (approximately Vitreloy 1). Cooling of the remaining liquid thus resulted in the formation of an amorphous matrix around the crystalline phase. In addition to the composite, a monolithic β phase sample with the same chemical composition found in the

dendrites of the composites was prepared by the arc melting procedure described above, except that there was no high-temperature hold used in the chemical partitioning step.

In-situ compression testing was performed on the specimens while neutron diffraction data were collected in the NPD and SMARTS diffractometers at the Lujan Neutron Science Center, Los Alamos National Laboratory. All specimens were cylindrical with a 6 mm diameter and 14.4 mm length (aspect ratio = 2.4). The setups of NPD and SMARTS permit the collection of multiple diffraction patterns simultaneously. Load frames specially constructed for these instruments allow the scattering vectors for the two $2\theta = \pm 90^\circ$ banks to be oriented parallel and perpendicular to the loading axis. This provides simultaneous measurement of the longitudinal and transverse lattice strains. Using the time-of-flight technique, diffraction patterns within a d spacing range of 0.5 to 4 Å were collected (see Fig. 4.15) and the Rietveld method [13-15] was employed to determine an average lattice strain in the β phase based on changes in its lattice parameter. The reported lattice strains were calculated relative to the lattice parameter at a nominal – 5 MPa compression needed to hold the sample in the load frame. In this study, results obtained from two samples are presented: a BMG/ β phase composite and a monolithic β phase specimen.



(a) Composite

(b) Monolithic β phase

Fig. 4.15 Diffraction patterns parallel to the loading axis for: (a) the composite sample and (b) the monolithic β phase sample. The raw data are shown as crosses fit with the Rietveld model. The lower curve exhibits the difference between the two. The sharp Bragg reflections in both patterns are from the BCC β phase (with a lattice constant of about 3.50 Å). In the composite (a), the presence of the amorphous BMG matrix is apparent from the undulating background.

4.3.1.3 Neutron Diffraction Data

Diffraction patterns parallel to the loading axis for both samples are shown in Fig. 4.15. In these patterns, the BCC structure of the β phase is clearly evident. The pattern for the composite, Fig. 4.15(a), shows a wavy background due to the amorphous matrix. The weighted fitting residuals, R_{wp} , for all Rietveld refinements were around 0.05 to 0.07 suggesting a good match between the data and the Rietveld model. Throughout the study (in both the monolithic and composite forms), the β phase was successfully described with the space group, $Im3m$ (BCC). This result eliminates the possibility of a stress-induced phase transformation in this phase (at least within the ~3-5 wt.% detection limit of neutron diffraction).

The macroscopic longitudinal deformation of both samples was monitored by an extensometer during the neutron diffraction experiments (see Figs. 4.16(a) and 4.17(a)

below). Although there is some nonlinearity in the low stress regions (likely due to settling of samples on the compression platens and/or some bending), the data obtained in this study match previous results. The stiffness of the monolithic β phase sample obtained from the extensometer data was around 70 GPa, comparable to the literature value of 63 GPa [10]. The macroscopic stiffness of the composite was 74 GPa, again close to the literature value (79 GPa in [10]). The deviations are attributed to sample and extensometer mounting and sample bending during loading, since as described below, the Young's modulus and Poisson's ratio of the β phase calculated from the bulk-averaged neutron data were within 7% of the literature values.

4.3.1.4 Lattice Strains and Elastic Anisotropy

The neutron diffraction data were analyzed using both the whole-pattern Rietveld refinement method [13-15] and single peak fits. Within the Rietveld technique, a crystal structure model is fit to the entire diffraction pattern and the lattice parameters determined yield an average strain value for a given phase. Single peak fits to individual reflections, on the other hand, provide information about lattice plane specific elastic and plastic behavior and are used in self-consistent model calculations.

Self-consistent (polycrystal deformation) models (SCM) [16-17], can predict the lattice plane specific Young's modulus and Poisson's ratio, also known as the diffraction elastic constants (DECs), with good accuracy [11,18-20]. These calculations require as input only the single crystal stiffnesses of the material. Within the SCM scheme the polycrystal is regarded as an agglomerate of ellipsoidal grains whose properties are determined by the single crystal properties (elastic and plastic) of the material.

Interactions between grains are modeled using the Eshelby theory [21] where each grain is embedded in a matrix (or “equivalent medium”) with the average properties of the polycrystal. Direct comparison of SCM predictions with diffraction experiments is possible via weighted averages of elastic strains in grains that are oriented with given lattice plane normals parallel to the scattering vector used in the experiment (see references [16-17] for further details). In the present work a “reverse” approach was followed, namely the SCM was used for the first time in combination with a least squares fitting program to determine the single crystal stiffnesses of the β phase based on its measured DECs. This approach is similar to that of Gnäupel-Herold *et al.* [22] who used Voigt, Reuss and other classical models, except that the SCM enables one to take into account the effects of the orientations and the finite size of the detectors in diffraction experiments. This is especially critical when the material is highly anisotropic, as is demonstrated below for the β phase.

The input data for the calculation of the single crystal stiffnesses of the β phase were the slopes of linear fits to the elastic region of the loading curves (up to about –600 MPa) in Fig. 4.16(b). The results of the calculation (Table 4.6) show that the β phase has a relatively low Young’s modulus, but large elastic anisotropy leading to elastic constants that vary significantly with crystallographic orientation. This can also be deduced from the spread of slopes in the elastic portions of the loading data in Fig. 4.16(b).

| β phase | E_R (GPa) | ν_R | E_S (GPa) | ν_S | C_{11} (GPa) | C_{12} (GPa) | C_{44} (GPa) | A |
|---------------|----------------|---------|----------------|---------|-------------------|-------------------|-------------------|-----|
| This study | 59(1) | 0.37(1) | 59(2) | 0.37(2) | 90(2) | 68(2) | 33(1) | 3.0 |

Table 4.6 Elastic constants for the β phase monolith determined from neutron diffraction data. Subscript “R” refers to Rietveld refinements and indicates elastic constants obtained from changes in lattice constants as a function of applied stress. Here, the error bars are based on linear fits to the neutron data. Subscript “S” refers to data from single peak fits which also employed the self-consistent model. The errors in this case are based on the least squares fitting routine. A is the anisotropy ratio: $2C_{44}/(C_{11}-C_{12})$.

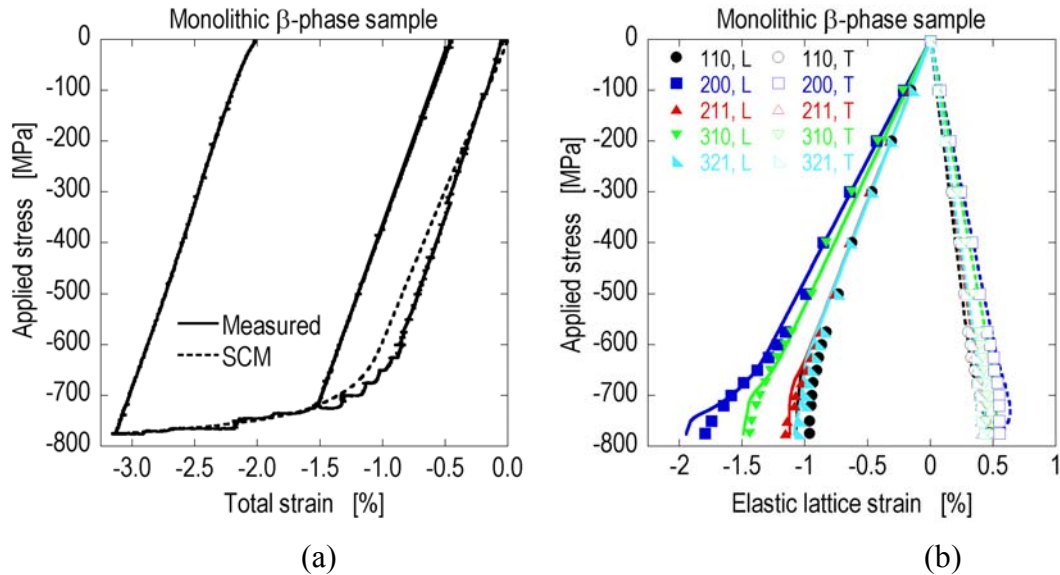


Fig. 4.16 Measured and calculated response of the monolithic β phase sample to applied compressive stress: (a) macroscopic strain along the loading axis; and (b) lattice plane specific elastic strain (symbols designate neutron data while lines are SCM predictions; (here, “L” and “T” indicate longitudinal and transverse directions, respectively). The difference between measured and calculated macroscopic stiffness shown in (a) is likely due to extensometer problems. This claim is supported by the fact that the diffraction data in the elastic region is in good agreement with model calculations as shown in (b).

4.3.1.5 Self-Consistent Modeling of Plastic Deformation

The single peak data also revealed information about the plastic anisotropy in the β phase. Since the 110, 211 and 321 reflections of cubic material are elastically identical, they are a good indicator of the onset of plasticity as they split after yielding due to their plastic anisotropy: beyond -600 MPa in the β phase monolith (see Fig. 4.16(b)) and beyond -1000 MPa in the composite (see Fig. 4.17(b)). To understand the *in-situ* plastic deformation of the composite, the SCM calculations were extended into the plastic regime.

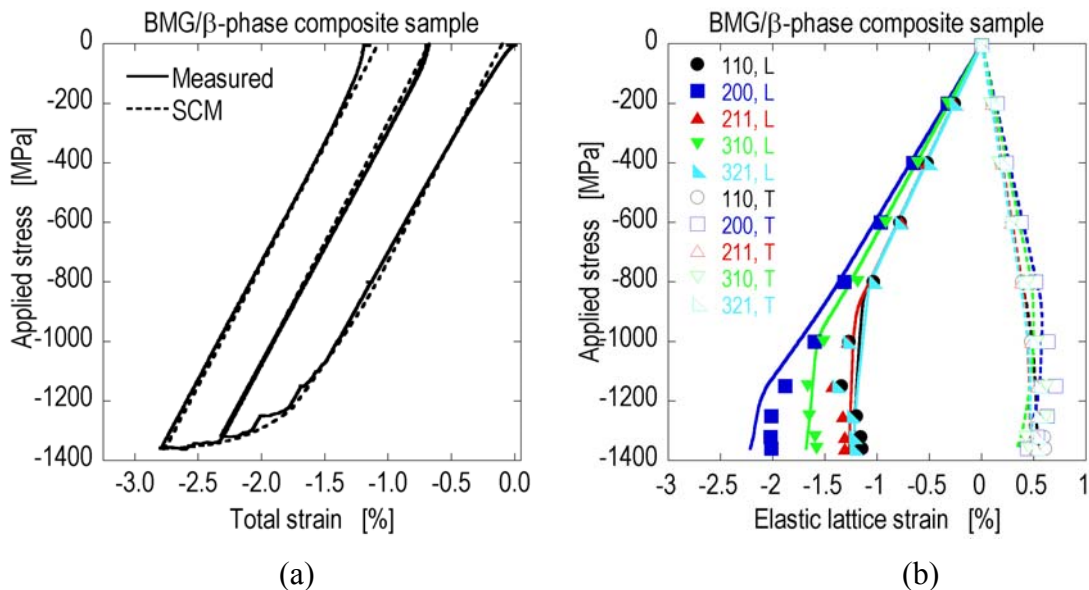


Fig. 4.17 (a) Comparison of measured (by extensometer) and calculated (SCM) macroscopic stress-strain curve for the composite sample. (b) Comparison of measured (symbols) and calculated (lines) lattice specific stress-strain curves for the β phase in the composite sample (“L” and “T” indicate longitudinal and transverse directions, respectively).

Modeling the deformation of a dendritic second phase in a composite is challenging due to the difficulty of assigning a representative geometry to accurately

describe dendrites. For this reason, some studies have employed approximate shapes in the form of a cylinder with a certain aspect ratio and used the finite element method [23] or have chosen a sphere in a mean field model [24]. In the present work, the β phase dendrites were approximated as spheres and a new self-consistent polycrystal deformation model was developed to describe the mechanical behavior of the β phase/BMG composites. A recent study [25] confirmed that the shape of β phase dendrites in a BMG composite does not influence the overall SCM predictions and that a sphere is a good approximation of a dendrite in this model.

Two new approaches were adapted in this study while performing SCM calculations. The first one was described earlier and involved a “reverse” calculation of the single crystal elastic constants starting from lattice plane dependent DECs via a least squares fitting. The second new addition to the SCM was the inclusion of a second phase to represent the BMG matrix. Here, the self-consistent polycrystal deformation model of Turner and Tomé [17] was improved so that the deformations of both the β phase and the BMG matrix were accounted for. The basic approach was to use the measured macroscopic stress-strain curve of the composite to refine its yielding and hardening behavior. To further validate the model, its lattice plane specific predictions were then compared to diffraction data from the β phase inside the composite.

First, the elastic-plastic deformation of the monolithic β phase was evaluated. The reader is referred to [16-17] for the description of the ‘traditional’ SCM based on dislocation slip in crystalline grains. Despite some problems with the extensometer data, reasonable fits to both the macroscopic strains and the lattice plane specific diffraction data were obtained (see Fig. 4.16). Overall, the monolithic β phase was found to have a

uniaxial yield stress of -610 MPa. This corresponds to an initial critical resolved shear stress of -300 MPa, which is the threshold shear stress used in the crystal-plasticity-based self-consistent models. Its strain hardening coefficient was found to be zero. It should be noted that the macroscopic data were used to determine the onset of non-linearity in the stress-strain plot which is independent of any systematic error in the extensometer data. The SCM calculations employed this information to evaluate the initial critical resolved shear stress. Similarly, the high plastic region (beyond -1.5% total strain in Fig. 4.16(a)) of the macroscopic stress-strain plot was fit by the model to obtain the strain hardening parameter.

The extensometer behaved more satisfactorily during the testing of the composite (Fig. 4.17(a)). Here, the metallic glass matrix was modeled as an isotropic continuum, i.e., without the elastic and plastic anisotropy found in the crystalline β phase. For the BMG, the von Mises (or J_2) yield criterion was assumed, which was shown by Lowhaphandu *et al.* [26-27] to be a good approximation of the plastic behavior of most BMG alloys. Since this is the first time that polycrystal plasticity and continuum mechanics have been combined in the rate independent SCM formulation, some alterations were needed to the model, mainly for the calculation of the elastic-plastic stiffness tensor (also known as the tangent stiffness tensor) of the BMG. These calculations were based on the J_2 theory described in detail in [28].

The β phase was modeled as a set of 10,000 single crystals with different orientations and the inherent single crystal stiffnesses and slip systems of the BCC crystal structure. The BMG was introduced into the model as an isotropic single grain weighted with the appropriate ratio of the volume fractions of the matrix and β phase. In this

formulation, the BMG still interacted with the average composite matrix (also known as the “equivalent medium”), as did the β phase grains. Further details of the model are presented in [29].

The results of the SCM calculations for the composite sample are shown in Fig. 4.17. The macroscopic predictions of the model were accurately fit to the measured composite stress-strain curve (Fig. 4.17(a)) using the initial BMG yield stress, the initial critical resolved shear stress for the β phase, and the hardening behavior of the BMG as variables. The single crystal elastic constants for the β phase used in the composite calculations were determined from the monolithic β phase sample. The Young’s modulus and Poisson’s ratio for the BMG matrix were taken from ref. [10]. The β phase was treated as non-hardening (or perfectly plastic, similar to the case for the monolithic β phase). This is consistent with the observation that the stress vs. elastic (lattice) strain curves for the β phase in the composite become vertical after yielding (see Fig. 4.17(b)). The reader should note that another mechanism that would lead to such behavior in the β phase is its complete debonding from the BMG matrix. So far, no large scale debonding at β phase/matrix interfaces has been observed [10].

As seen in Fig. 4.17(a), the agreement between the model and data on the macroscopic scale is good. The initial critical resolved shear stress for the β phase was estimated as -325 MPa, and the initial von Mises critical shear stress of the BMG was found to be -800 MPa. These values are somewhat different from those for the monoliths (-300 MPa for the monolithic β phase and a literature value of about $-1600/\sqrt{3} = -924$ MPa, i.e., tensile yield stress divided by $\sqrt{3}$ for the matrix [10]). It is possible that thermal residual stresses developed in the composite during processing altered the

“apparent” yield points of each phase. If so, this would suggest an initial tensile longitudinal residual stress in the β phase and a compressive stress in the BMG.

The hardening behavior of the BMG was modeled with a Voce-type exponentially decreasing hardening function (often used in the traditional SCM [17]):

$$\bar{h}(\bar{\epsilon}_p) = \tau_0 + (\tau_1 + \theta_1 \bar{\epsilon}_p) \left(1 - e^{-\left(\frac{\bar{\epsilon}_p \theta_0}{\tau_1}\right)}\right) \quad (1)$$

where τ_0 is the initial critical shear stress, $\bar{\epsilon}_p$ is the equivalent plastic strain (the hardening parameter), τ_1 is the width of the transition range, θ_0 is the hardening slope at the initial shear stress and θ_1 is the hardening slope at the end of the transition range. The hardening modulus of the BMG was found to change from an initial value of 52 GPa (θ_0) at an initial critical shear stress of -800 MPa (τ_0) to a final value of 1 GPa (θ_1) over an 80 MPa range (τ_1). The hardening parameters were determined by trial-and-error calculations which yielded an error bar of less than 3%.

To further validate the model, its lattice plane dependent estimates were compared with the diffraction data (Fig. 4.17(b)). The model predicts the elastic region with good accuracy. The predictions are also satisfactory in the plastic region except that beyond -1200 MPa the measured data show a slight reversal in the elastic strain, whereas the model exhibits saturation. The SCM estimates also compare very well to the transverse strain data. Overall, the agreement between the model predictions and the neutron data is quite satisfactory and comparable to SCM predictions for other materials [11,16,20].

Fig. 4.18 shows the calculated *in-situ* behavior of each phase in the composite as well as the composite average. The calculated *in-situ* stiffnesses for the β phase and the matrix are 61 and 89 GPa, respectively. These values compare very well to those reported

in the literature. Szuecs *et al.* [10] studied monolithic β phase and metallic glass (prepared under identical conditions to those used in the present study) and reported Young's moduli of 63 GPa for the β phase and 89 GPa for the BMG monolith. Similarly, the composite modulus predicted by the SCM model (81 GPa) is comparable to the value measured by the extensometer and to that obtained by Szuecs *et al.* (~ 79 GPa) [10].

The current results clearly show that it is the β phase that yields first during the loading of a BMG/ β phase composite. A possible scenario that follows is that the load transfer to the BMG matrix that succeeds the yielding of the β phase and/or the stress concentrations generated at the intersection of slip bands in the β phase and the matrix/particle interface induce multiple shear bands in the BMG matrix. Such shear bands have indeed been observed in β phase/BMG composites subject to plastic strain [8-10]. The multiple shear bands in the BMG enhance its ductility and damage tolerance as a single, catastrophic shear band is avoided. It should be noted that contrary to its monolithic behavior, the BMG does appear to strain harden in the composite (see Fig. 4.18), which is likely related to the generation of multiple shear bands in it. In the present study, calculations (not reported here) showed that agreement between the self-consistent model and experimental data was not possible without including strain hardening in the BMG. The details of the micromechanics of multiple shear band generation in β phase/BMG composites, however, are still unclear and subject to future investigations.

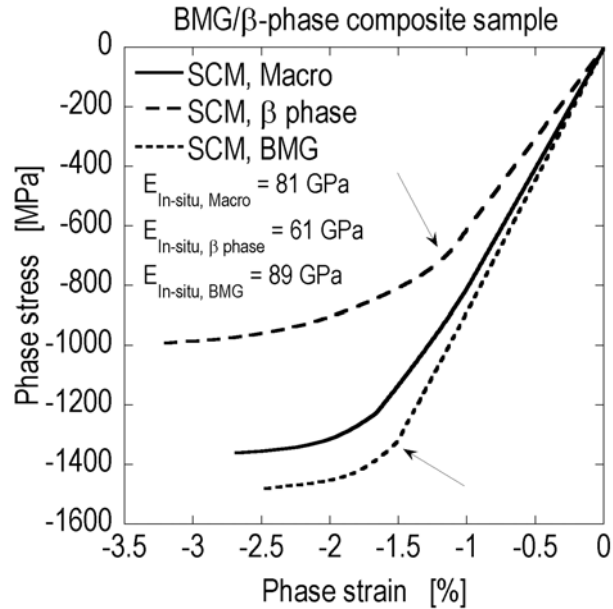


Fig. 4.18 Calculated *in-situ* behavior (phase stress vs. phase strain) for the composite. The arrows indicate the yield points in the β phase (about -650 MPa) and the BMG matrix (around -1350 MPa). The solid line (“macro”) designates the composite behavior. The *in-situ* Young’s moduli for each phase are also shown.

4.3.1.6 Texture Evolution in the β Phase

The previous discussion established that the dislocation slip based plasticity of the β phase plays a significant role in the ductility of BMG/ β phase composites. Moreover, the diffraction data showed that there was no detectable stress-induced phase change upon loading the β phase. This section deals with the last possible deformation mechanism in the β phase: twinning.

If a crystalline metal is subjected to plastic deformation, it is expected that texture will develop in it. For instance, Pang *et al.* [30] reported changes in peak intensities reaching 50% for the 111 and 220 reflections in an FCC stainless steel sample deformed by dislocation slip up to 8% in tension. If plastic deformation is governed by twinning, a much larger and abrupt shift in peak intensity is to be expected. Brown *et al.* [31]

demonstrated peak intensity changes of 100% or more, even with some peaks totally disappearing and new ones appearing in U - 6 wt.% Nb alloys that deform by twinning. Furthermore, the two plastic deformation modes, slip and twinning, lead to different texture developments in the material depending on the nature of active slip or twin systems.

Fig. 4.19 exhibits the change in the measured peak intensities in the β phase parallel to the loading axis for the two samples as a function of applied stress. This provides a qualitative description of texture development since more detailed texture data (which requires diffraction patterns in multiple orientations) are not available at present. The expected texture development during uniaxial compression of a BCC metal due to crystallographic slip is combined $\langle 111 \rangle$ and $\langle 100 \rangle$ fiber texture [32] along the compression axis (the $\langle 111 \rangle$ component being the strongest). This is exactly opposite of what is expected for FCC metals due to the relationship between slip planes and slip vectors in BCC and FCC crystal structures [32]. Based on the reported peak intensity changes [30] and the plastic deformation of the monolithic β phase sample, one would expect no more than 40% change in the intensity of the 222 (111 is not an allowed reflection in the BCC crystal structure) and 200 reflections of the β phase if its plastic deformation were entirely due to dislocation slip. The experimental data for the monolithic sample (see Fig. 4.19(b)) indeed show a change of about 40% for the 200 reflection, but unfortunately the intensity of the 222 reflection was too weak to be analyzed using single peak fits. The changes in peak intensity seen for the 200 (increasing) and 110 (decreasing), too, are consistent with that of plastic deformation by dislocation slip as described in [32]. The large increase of the 321 peak intensity in the

composite is not seen in the monolithic sample and could be an indication of slightly changed slip pattern in the β phase inside the composite due to the additional constraints by the BMG matrix. In conclusion, the present data lend support to a dislocation slip based deformation in the β phase, although a minor contribution from twinning cannot be entirely discounted. Additional studies are underway to further clarify texture development in monolithic β phase and β phase/BMG composites subject to large plastic deformation.

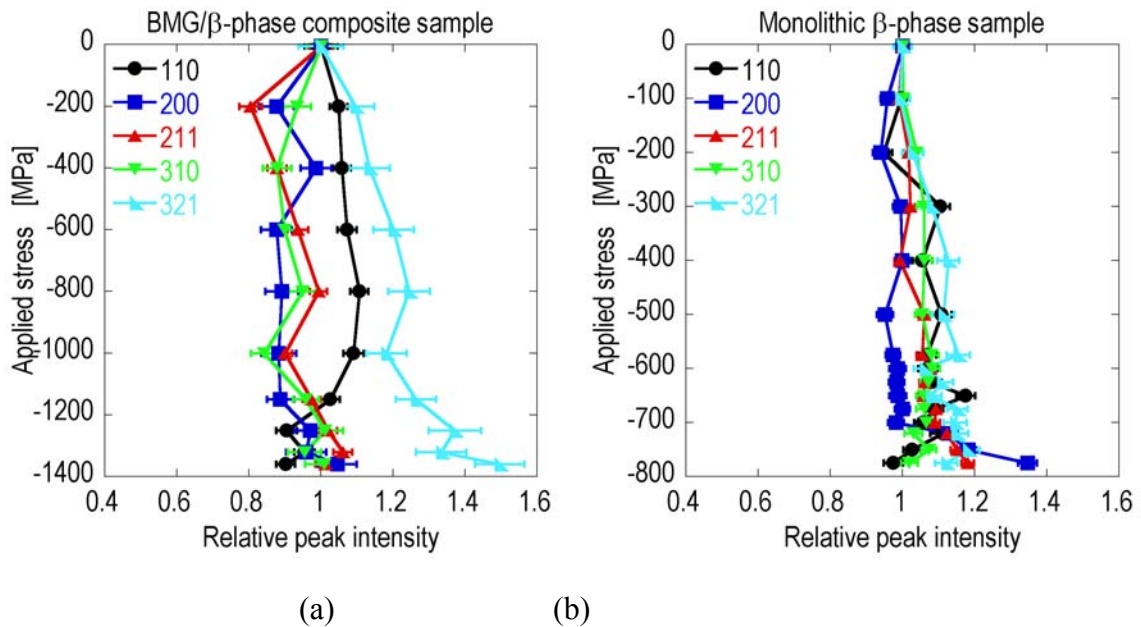


Fig. 4.19 Development of peak intensity parallel to the loading axis as a function of applied stress in the β phase for: (a) the composite, and (b) the monolithic β phase.

4.3.1.7 Summary of the Deformation Mechanism in As-cast Composites

The compressive deformation of as-cast *in-situ* composites was investigated with neutron diffraction and self-consistent modeling (SCM) for the first time. Previous studies [10] had proposed several deformation mechanisms for the β phase including

stress-induced phase transformations, twinning and dislocation slip. The neutron diffraction data conclusively showed that no detectable phase transformations were present as the β phase remained BCC during its deformation in both monolithic and composite forms. Furthermore, the low degree of texture development observed suggested that twinning was not a dominant deformation mechanism. This left dislocation slip as the only active deformation mode in the β phase. This conclusion was also supported by the fact that the SCM calculations, that considered only dislocation slip in the β phase, showed good agreement with the lattice plane specific diffraction data.

The successful fitting of model predictions with diffraction data allowed the deduction of the mechanical properties of the β phase, both as a monolith and inside a metallic glass matrix. It was shown that the β phase is highly anisotropic in the elastic regime (with an anisotropy ratio reaching 3.0), has a uniaxial yield point of about -600 MPa and plastically deforms by dislocation slip. The β phase was seen to largely retain these properties inside a metallic glass matrix. The SCM predictions also yielded insight into the load sharing behavior of the two phases in the composite. It was demonstrated that, upon loading, the β phase yields first (around -600 to -700 MPa), then starts transferring load to the matrix. The BMG matrix enters the “plastic” regime around -1400 MPa by presumably initiating multiple shear bands. It is speculated that the plastic deformation of the dendritic β phase somehow triggers shear banding in the matrix. However, the detailed micromechanical description of this process is still lacking and is subject to future studies.

4.3.2 Tensile Loading Behavior of As-cast Specimens during Synchrotron X-ray Diffraction

X-ray diffraction using an area detector yields multiaxial strain and texture information. To exploit this feature of XRD several *in-situ* tensile tests were performed at APS with high energy X-rays (80 keV). Cyclic loading was applied up to 4.3% total strain, and the first two cycles analyzed so far with the Rietveld method are shown in Fig. 4.20. It is seen that as the β phase starts yielding, it experiences progressively compressive lattice strain. Future work will attempt to compare these data with the predictions of the self-consistent model presented above. Due to its multiaxial nature, the synchrotron data are expected to offer a more rigorous test for the model.

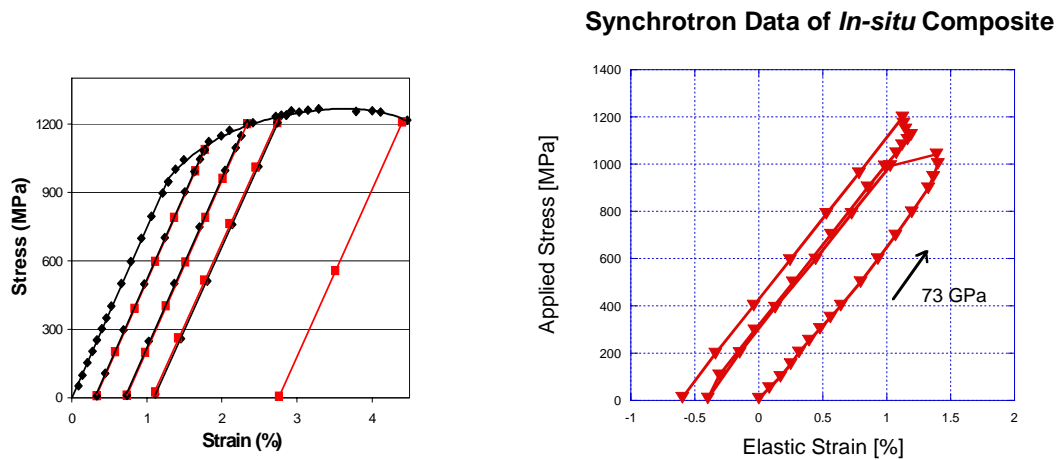


Fig. 4.20 Macro stress-strain curve (left) and synchrotron X-ray diffraction data (lattice strain in the β phase - right) from an as-cast composite under cyclic tensile loading.

4.4 Effect of Heat Treatment on *In-situ* Composites

The preceding sections established that the mechanical behavior of the *in-situ* composites is largely controlled by the dendritic reinforcements. The combined neutron diffraction – self-consistent modeling study showed that in the as-cast form, the β phase deforms by dislocation slip. On the other hand, heat treatment led to significant embrittlement in both the composite and the monolithic β phase. As will be shown in Chapter 5, heat treatment appears to induce ordering in the β phase. Such an effect of ordering on alloy ductility is a commonly observed phenomenon. Fig. 4.21 illustrates the effect of atomic bonding on the Peierls-Nabarro force encountered by moving dislocations. Here, the size of the dislocation width (W) is dependent upon the directionality of the bonding. W is large in a typical ductile metal (due to limited directional bonding), while it is usually small when ordering, or directional bonding is present (also in ceramics). As a result, the Peierls-Nabarro force encountered by a gliding dislocation is expected to be much larger in ordered alloys [33]. When dislocation motion is hindered, it is possible that the other competing deformation mechanism, namely twinning, may become active in the heat treated (and ordered) β phase. The ongoing analysis of the *in-situ* deformation data from diffraction experiments may shed light on this issue. In any case, however, dislocation slip will be hindered and the alloy will become more brittle.

Another interesting effect of ordering in the heat treated β phase is its stiffening. To gauge its influence on the composite behavior, some parametric studies were performed using the self-consistent model presented earlier. Fig. 4.22 exhibits some of the results of these studies. It is clear that as the β phase stiffens, the overall ductility of

the composite decreases dramatically. This result proves, once again, the need for soft, compliant dendrites to achieve high ductility in these composites.

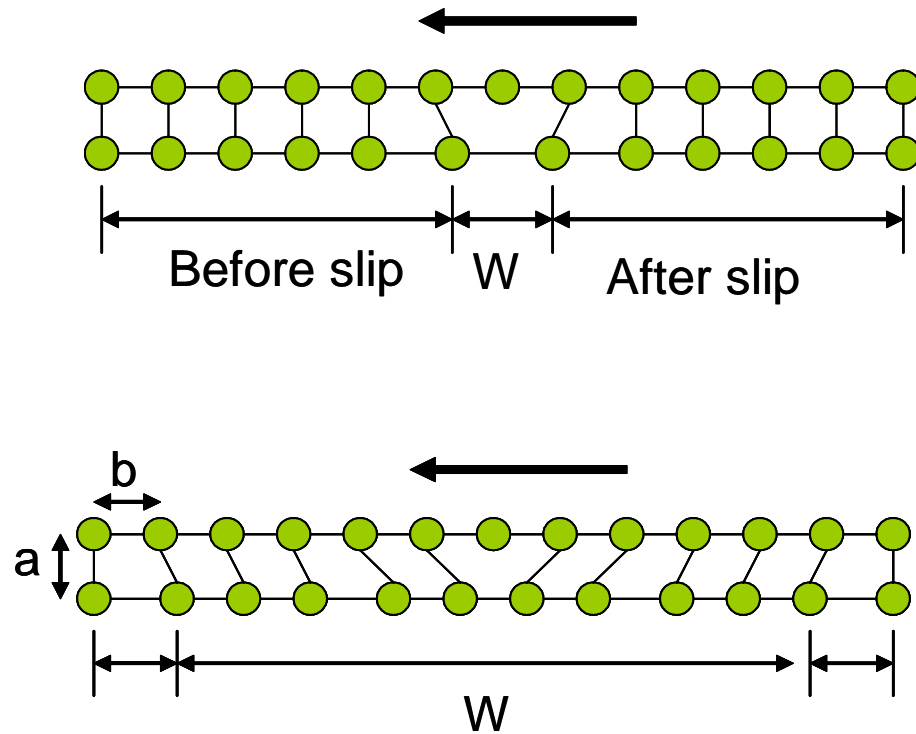


Fig. 4.21 Schematic of dislocation width for a ceramic or ordered metal (top) and a typical ductile metal (below).

$$\tau_p \approx \frac{2G}{1-\nu} e^{-2\pi w/b} \approx \frac{2G}{1-\nu} e^{-[2\pi a/(1-\nu)b]} \quad (2)$$

Peierls-Nabarro Force [33]

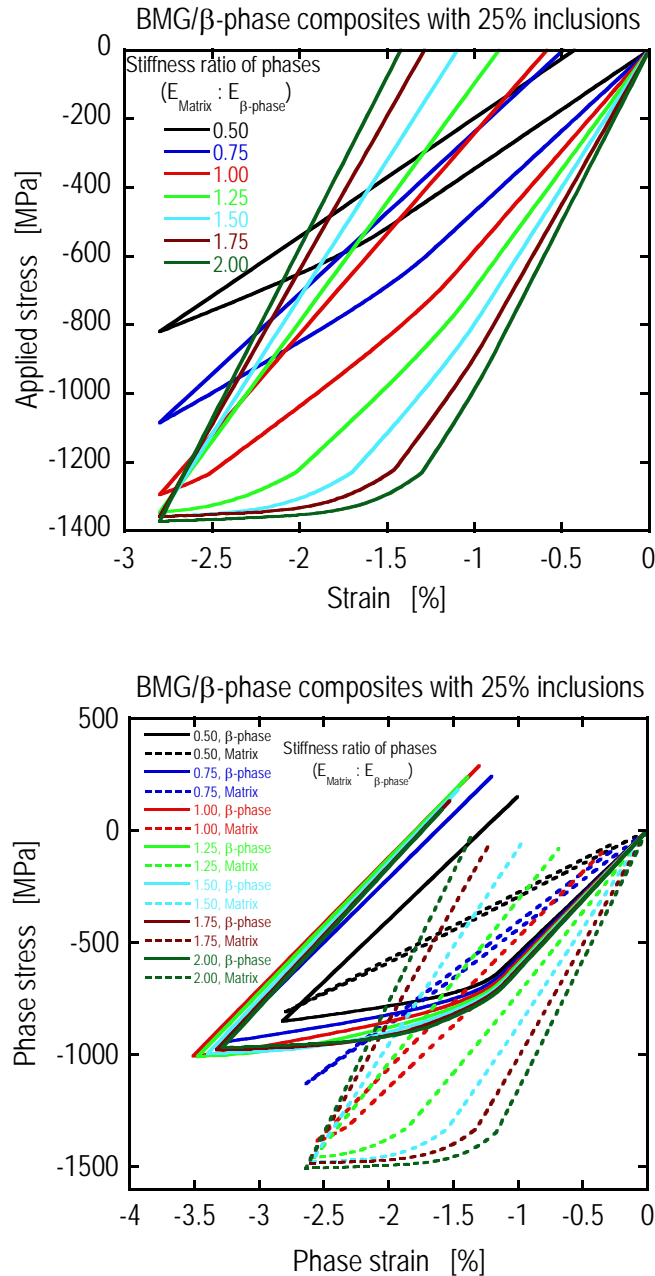


Fig. 4.22 Self-consistent model calculation of composite (top) and phase-specific stress-strain plots (bottom) by varying the relative Young's moduli of the amorphous matrix and the β phase reinforcements. In the as-cast composites, $E_{\text{matrix}} / E_{\beta\text{ phase}} \sim 1.5$. The calculations employed the constitutive relations shown in Fig. 4.18 and assumed 25 vol.% dendrites. In the top figure, a clear trend is observed towards lower ductility (as quantified by the area under the stress-strain curve) when the β phase reinforcements become stiffer.

4.5 Conclusions

The most attractive BMG composite, Zr-based *in-situ* β phase composite, was developed in 1999, and systematic optimization was carried out on it over the past several years. It was found that an extra addition of Nb increases ductility and thermal stability. Although β phase was known to lead to the formation of multiple shear bands in the BMG matrix with a similar spacing to that of the secondary dendrites, the underlying deformation mechanism and load sharing in the composite could not be determined from macroscopic tests alone. In order to obtain further insight into the deformation of *in-situ* composites, diffraction experiments were performed in the present study combined with mechanics modeling.

The neutron diffraction results combined with self-consistent modeling revealed that in the as-cast composites (with the highest ductility known to date), the β phase yields first and starts to deform plastically via dislocation slip. During this process, load is transferred to the matrix initiating multiple shear bands in it. The complicated three-dimensional morphology of the dendrites enhances multiple shear band formation, and hence, leads to higher ductility in the amorphous matrix. The previously considered twinning and stress induced phase transformation mechanisms were not supported by diffraction data analysis, and it was concluded that dislocation slip is the most dominant mechanism for the β phase inside the as-cast composite.

On the other hand, if the reinforcement is ordered after heat treatment below the glass transition temperature of the amorphous matrix, it stiffens and its resistance to dislocation slip increases dramatically resulting in a stiff and hard, but brittle composite. The ultrasound measurement of elastic constants and neutron data show drastic increases

in the Young's and shear moduli of the β phase. This suggests that dislocation slip in the β phase may no longer be the major deformation mechanism due to the high Peierls-Nabarro force and the high shear modulus due to increased bonding directionality, and twinning may become a prominent deformation mechanism once the ordering takes place. Additional diffraction work is underway to better quantify the contribution of twinning in heat treated specimens.

To achieve desired mechanical performance by composites, especially high ductility, it is crucial to understand the two major parameters that control multiple shear band formation in the matrix: shear blocking and shear softening, i.e., the geometric constraints by and the mechanical properties of reinforcements, respectively. Results from the particulate and fiber composites suggested the importance of stopping shear band propagation by reinforcements, and geometric constraints such as the volume fraction, size and the shape of the reinforcements were seen as important factors. The three dimensional, complicated geometry of dendrites in the *in-situ* composites can certainly provide effective geometric constraint. However, the heat treatment study of *in-situ* composites showed that the overall composite properties can be strongly influenced by the mechanical properties of reinforcements as well. To resolve this issue and to quantify the relative contributions of geometric constraints by reinforcements and shear softening in the matrix on multiple shear band formation in the latter, a deeper understanding of the micromechanics of shear band initiation at the matrix/reinforcement interface is crucial. This is another important topic for future work. The mechanical properties of BMG composites can be optimized only after the micromechanics of shear band formation in these materials is fully appreciated.

References

- [1] W. L. Johnson (1996). Fundamental aspects of bulk metallic glass formation in multicomponent alloys. *Metastable, Mechanically Alloyed and Nanocrystalline Materials*, Pts 1 and 2. **225**: pp. 35-49.
- [2] X. H. Lin (1997). Bulk glass formation and crystallization of Zr-Ti based alloys. Caltech Ph.D. Thesis.
- [3] X. H. Lin and W. L. Johnson (1995). *Journal of Applied Physics* **78**(11): 6514-6519.
- [4] H. Choi-Yim, R. Busch, U. Koster and W. L. Johnson (1999). *Acta Materialia* **47**(8): 2455-2462.
- [5] R. D. Conner, R. B. Dandliker and W. L. Johnson (1998). *Acta Materialia* **46**(17): 6089-6102.
- [6] C. P. Kim (2001). Ductile phase reinforced bulk metallic glass composites formed by chemical partitioning. Caltech Ph.D. Thesis.
- [7] B. Clausen, S. Y. Lee, E. Ustundag, C. P. Kim, D. W. Brown and M. A. M. Bourke (2002) Deformation of *in-situ*-reinforced bulk metallic glass matrix composites. *Ecrs 6: Proceedings of the 6th European Conference on Residual Stresses*. **404-4**: pp. 553-558.
- [8] C. C. Hays, C. P. Kim and W. L. Johnson (2000). *Physical Review Letters* **84**(13): 2901-2904.
- [9] C. C. Hays, C. P. Kim and W. L. Johnson (2001). *Materials Science and Engineering a-Structural Materials Properties Microstructure and Processing* **304**: 650-655.
- [10] F. Szuecs, C. P. Kim and W. L. Johnson (2001). *Acta Materialia* **49**(9): 1507-1513.
- [11] B. Clausen, T. Lorentzen, M. A. M. Bourke and M. R. Daymond (1999). *Materials Science and Engineering a-Structural Materials Properties Microstructure and Processing* **259**(1): 17-24.
- [12] R. Vaidyanathan, M. A. M. Bourke and D. C. Dunand (1999). *Acta Materialia* **47**(12): 3353-3366.

- [13] H. M. Rietveld (1967). *Acta Crystallographica* **22**: 151-&.
- [14] H. M. Rietveld (1969). *Journal of Applied Crystallography* **2**: 65-&.
- [15] R. B. Vondreele, J. D. Jorgensen and C. G. Windsor (1982). *Journal of Applied Crystallography* **15**(DEC): 581-589.
- [16] B. Clausen, T. Lorentzen and T. Leffers (1998). *Acta Materialia* **46**(9): 3087-3098.
- [17] P. A. Turner and C. N. Tome (1994). *Acta Metallurgica Et Materialia* **42**(12): 4143-4153.
- [18] B. Clausen and T. Lorentzen (1997). *Metallurgical and Materials Transactions a-Physical Metallurgy and Materials Science* **28**(12): 2537-2541.
- [19] T. Lorentzen, M. R. Daymond, B. Clausen and C. N. Tome (2002). *Acta Materialia* **50**(6): 1627-1638.
- [20] T. M. Holden, R. A. Holt and C. N. Tome (2000). *Materials Science and Engineering a-Structural Materials Properties Microstructure and Processing* **282**(1-2): 131-136.
- [21] J. D. Eshelby (1957). *Proceedings of the Royal Society of London Series a-Mathematical and Physical Sciences* **241**(1226): 376-396.
- [22] T. Gnaupel-Herold, P. C. Brand and H. J. Prask (1998). *Journal of Applied Crystallography* **31**: 929-935.
- [23] G. A. Henshall, P. R. Subramanian, M. J. Strum and M. G. Mendiratta (1997). *Acta Materialia* **45**(8): 3135-3142.
- [24] P. Peralta, R. Dickerson, J. R. Michael, K. J. McClellan, F. Chu and T. E. Mitchell (1999). *Materials Science and Engineering a-Structural Materials Properties Microstructure and Processing* **261**(1-2): 261-269.
- [25] E. Ustundag and B. Clausen (2003). *Materials Science and Engineering A* submitted.
- [26] P. Lowhaphandu, L. A. Ludrosky, S. L. Montgomery and J. J. Lewandowski (2000). *Intermetallics* **8**(5-6): 487-492.
- [27] P. Lowhaphandu, S. L. Montgomery and J. J. Lewandowski (1999). *Scripta Materialia* **41**(1): 19-24.
- [28] Z. P. Bazant and M. Jirasek (2001). *Inelastic Analysis of Structure*. New York, John Wiley: pp. 317-323.

- [29] B. Clausen, S. Y. Lee, E. Ustundag, C. P. Kim, J. C. Hanan, D. W. Brown and M. A. M. Bourke (2005). *Journal of Applied Physics* to be submitted.
- [30] J. W. L. Pang, T. M. Holden, J. S. Wright and T. E. Mason (2000). *Acta Materialia* **48**(5): 1131-1140.
- [31] D. W. Brown, M. A. M. Bourke, P. S. Dunn, R. D. Field, M. G. Stout and D. J. Thoma (2001). *Metallurgical and Materials Transactions a-Physical Metallurgy and Materials Science* **32**(9): 2219-2228.
- [32] U. F. Kocks, C. N. Tome and H. R. Wenk (1998). *Texture and Anisotropy*. Cambridge, UK, Cambridge University Press: pp. 18.
- [33] G. E. Dieter (1988). *Mechanical Metallurgy*.

CHAPTER 5

RESULTS AND DISCUSSION:

MICROSTRUCTURE AND PHASE EVOLUTION

OF *IN-SITU* β PHASE COMPOSITES

5.1 Microstructure of *In-situ* β Phase Composites

The main purpose of investigating these composites is to optimize their composition and microstructure, which govern their overall mechanical properties. C. P. Kim and W. L. Johnson at Caltech developed the $Zr_{56.2}Ti_{13.8}Nb_{5.0}Cu_{6.9}Ni_{5.6}Be_{12.5}$ *in-situ* composites (LM2) in 1999 in the process of searching for a new BMG system around $Zr_{41.2}Ti_{13.8}Cu_{12.5}Ni_{10.0}Be_{22.5}$ (also known as Vitreloy 1 or LM1). The LM2 composite consists of a dendritic and ductile BCC crystalline phase within an amorphous matrix which is almost identical to Vitreloy 1 [1]. Since then, Liquid Metal Technologies (LMT) has developed many other Zr-based *in-situ* composites (called the LM2 series), and systematic optimization has been performed to increase thermal stability and mechanical properties. The $Zr_{56.2}Ti_{11.3}Nb_{7.5}Cu_{6.9}Ni_{5.6}Be_{12.5}$ *in-situ* composite called LM2A2 (note that it contains 7.5% Nb instead of 5% in the LM2 series) was chosen as the best, based on its ΔT (i.e., the temperature difference between T_x - crystallization and T_g - glass transition) and toughness as explained previously in Section 4.1.2. Since compositional optimization was reached, it became important to correlate mechanical properties with microstructure that is controlled by processing conditions.

As the physical properties such as elastic and shear moduli are very sensitive to processing conditions, and yield properties are dependent on microstructure, it was

crucial to investigate microstructure in more detail and correlate it with processing. This chapter first presents a detailed microstructural analysis of β phase composites. This is followed by an in-depth investigation of phase evolution during heat treatment to correlate the significant hardening and stiffening described in Chapter 4 with changes in the β phase.

By taking advantage of the excellent glass forming ability associated with Vitreloy 1 (critical cooling rate of 1.8 K/s, [2]), β phase *in-situ* composites (LM2 series) have been successfully made in the arc-melter and studied. The arc-melter provides a wide range of cooling rates compared to mold casting due to unidirectional cooling and bigger sample size, but it still has to maintain cooling rates which are needed to ensure the glassy structure of the matrix. The critical cooling rate equation for a plate and cylinder can be derived as follows [3]:

$$R_{\text{crit}}^{\text{plate}} \text{ (K/s)} = \frac{0.4\kappa T_L}{L_{\text{crit}}^2} = \frac{0.4K_t T_L}{C_p L_{\text{crit}}^2} \quad (1)$$

$$R_{\text{crit}}^{\text{cylinder}} \text{ (K/s)} = \frac{0.8\kappa T_L}{D_{\text{crit}}^2} = \frac{0.8K_t T_L}{C_p D_{\text{crit}}^2} \quad (2)$$

κ = thermal diffusivity of the liquid alloy
 T_L = liquidus temperature of the alloy (K)
 L = plate thickness (cm)
 D = cylinder diameter (cm)
 K_t = thermal conductivity (Watts/cm-K)
 C_p = specific heat of the alloy (J/cm³-K)

The formula assumes that the thermal conductivity of the mold is at least ~10 times that of the liquid alloy. For example, for Vitreloy 1, $K_t=0.18$ Watts/cm-K, $C_p=5$ J/cm³-K,

$T_L=1000\text{K}$, then $R_{\text{crit}}^{\text{plate}} \approx 15/L^2$ (cm), $R_{\text{crit}}^{\text{cylinder}} \approx 30/D^2$ (cm); for $R_{\text{crit}}=1.8$ K/s, one obtains $L=2.9$ cm in plate and $D=4.1$ cm in cylinder geometry. That means one can make an *in-situ* composite in the arc-melter up to 1.4 cm in height because the heat transfer solution for the top of the button with one side as heat sink is very close to the solution at the center of a two times thicker plate with heat sinks at both sides. Therefore, it is estimated that an LM2A2 *in-situ* β phase composite can be made up to 30 g (a hemisphere of 1.4 cm radius and a density of 6.3 g/cm^3 [4]) using the arc-melter without crystallization. In other words, the cooling rate of a Cu mold for a 5 mm diameter rod is about 120 K/s, while for a hemispherical arc-melted sample with 5 mm radius it is 15 K/s.

In the present study, two different kinds of samples were prepared: a wedge-shaped copper mold casting and an arc-melted button. Both of them experienced varying cooling rates over different regions in them, and exhibit different size and shape of the dendritic β phase while volume fraction of this phase remained in the range of 40% ($\pm 4\%$). In the second part of the microstructure study, tensile yield strength was indirectly calculated from Vickers hardness tests to relate microstructural variations with the mechanical properties of the composites.

5.1.1 Microstructure of Wedge-Shaped LM2A2

Ingots of LM2A2 materials prepared in the arc-melter were cut into small pieces to fit into a quartz tube with an inner diameter of 8 mm. A Cu mold carved into a wedge shape was put inside the casting chamber and the quartz tube was located above it in contact with the gate of the mold. A turbo-pump-aided pumping system lowered the pressure to the level of $10^{-3} \sim 10^{-4}$ torr, and materials were heated by an induction coil

around the quartz tube, followed by an injection process with pressurized Ar gas. The final sample dimensions were 38.4 mm height x 7.8 mm width x 4.3 mm thickness with a wedge angle of 11.6°.

Considering the geometry of the wedge shape, one can expect a lower cooling rate going up to the top and/or moving towards the center of the sample. Fig. 5.1 illustrates microstructural changes in the center along the vertical axis. At the very bottom of the sample, no noticeable second phase was detected, probably because the kinetics of the second phase precipitation is not fast enough to overcome the high quenching rate there [5]. Dendrite size begins to gradually increase from bottom to top, indicating that slow cooling allows more time for dendrites to grow. The morphology of the second phase appears equiaxed regardless of dendrite size and sampling volume location, which suggests that heat flux is not uniaxial and/or cooling rate is fast enough to prevent directional growth in the second phase. This is a reasonable assumption for the mold casting sample. However, as will be shown below, the arc-melted button experienced more directional heat flux from the bottom and top and perhaps a lower cooling rate even though sample thickness was the same (7.8 mm) in both samples.

In the wedge-shaped sample, dendrite size is about 2-4 μm near the bottom, and increases to 4-7 μm around the center of the sample. The maximum dendrite size in this sample is around 8-10 μm at the very top of the wedge.

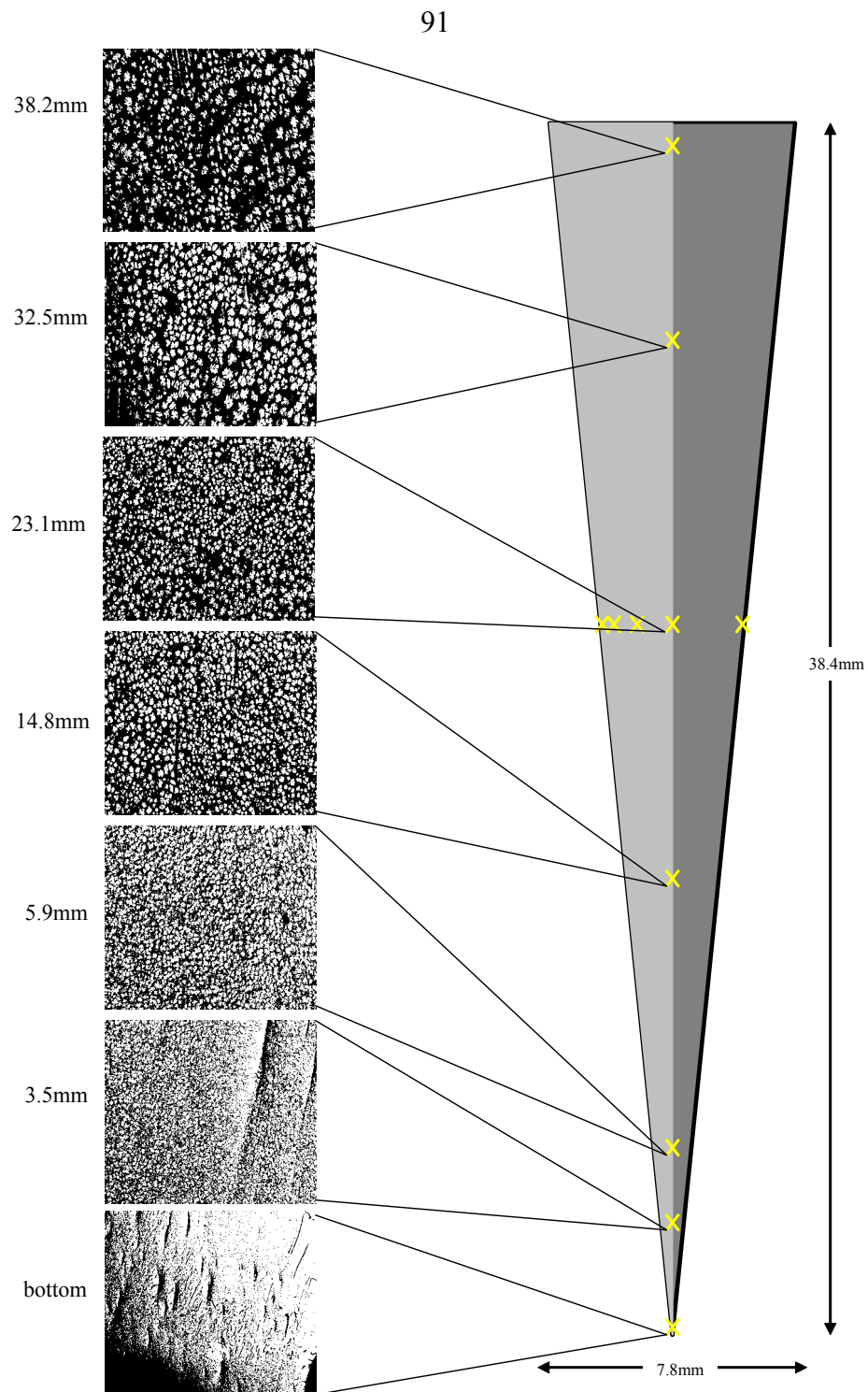


Fig. 5.1 Backscattered SEM images of the microstructure of the wedge-shaped LM2A2 sample along its vertical axis. Here, the bright regions belong to the β phase while the dark area is the amorphous matrix. Numbers indicate distance from the bottom corner (magnification: x 1000). Slow cooling regions show large dendrite size as expected.

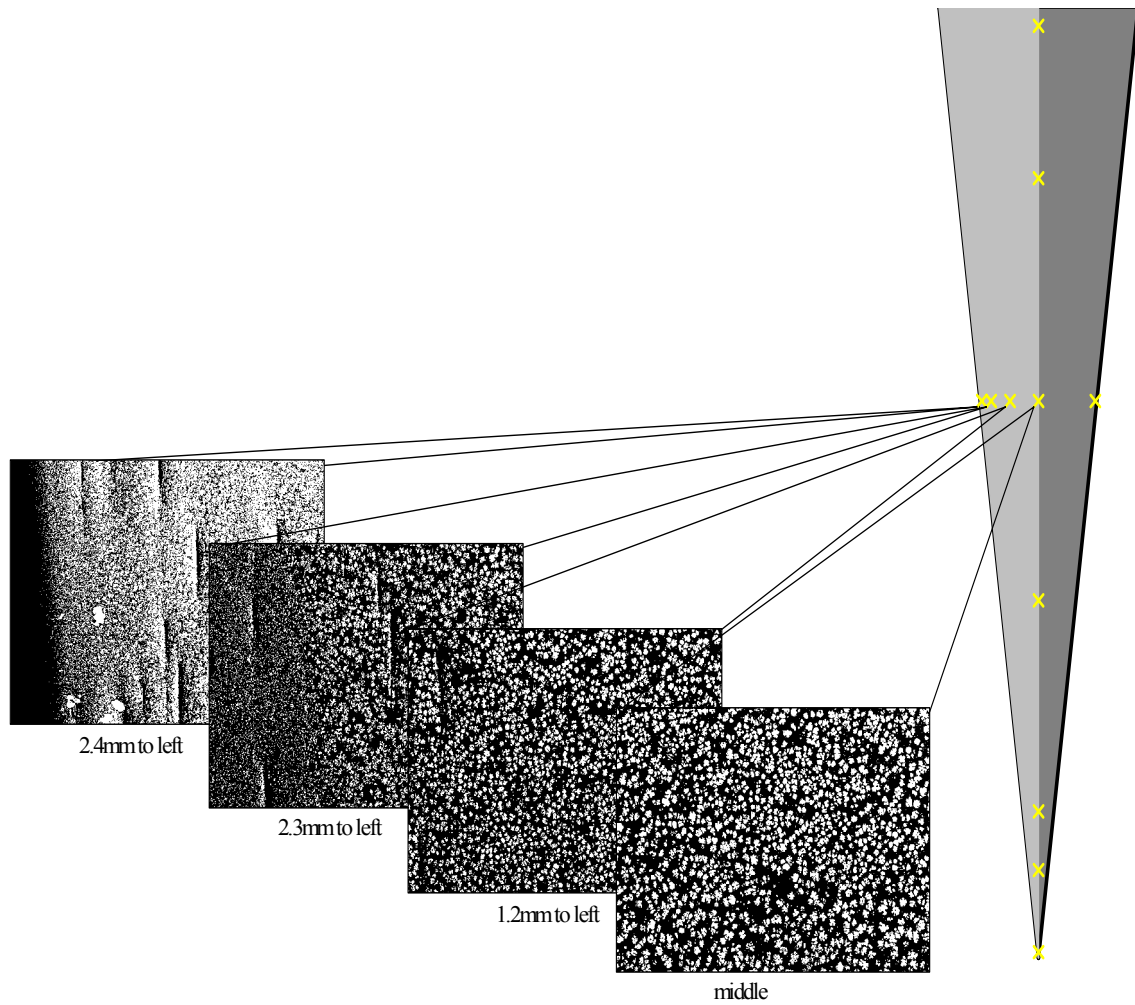


Fig. 5.2 Backscattered SEM images of the microstructure of the wedge-shaped LM2A2 sample along its horizontal axis. Here, the bright regions belong to the β phase while the dark area is the amorphous matrix. Numbers indicate distance from the central line (magnification: x 1000).

The horizontal scan reveals a similar trend in microstructure as that observed along the vertical one. Dendrite size varies from 1 μm to 7 μm and dendrites become visible in the SEM at about 80 μm from the outside surface (for x 1000 magnification). As shown in Chapter 4, the Cu-mold-quenched LM2A2 sample exhibits 40% dendrite volume fraction, similar to all the other *in-situ* composites. It is worth noting that casting pores often exist in samples prepared by Cu mold casting and many of such pores (about 20-30 μm in diameter) were observed at certain spots in the LM2A2 wedge sample as well. This observation explains why all composite materials processed through Cu mold casting never exhibit any ductility in tension tests despite enhanced compressive ductility. It is presumed that these pores function as stress concentrators and crack opening sources [6-7]

5.1.2 Microstructure of Arc-Melted LM2A2

In this study, 10 g of raw materials were used to obtain a hemisphere of 16 mm diameter x 7.8 mm height. Fig. 5.3 shows SEM images of the arc-melted sample along its vertical axis. At the very bottom (known as the skull), there is no clear distinction between the amorphous matrix and the β phase dendrites. Each phase becomes identifiable around 0.7 mm from the bottom, and long streaks of β phase are seen inside the matrix suggesting unidirectional cooling toward the bottom. Between 1.3 ~ 1.9 mm from the bottom, the largest dendrites are located and their size ranges from 8-12 μm . As the height increases, dendrites first become smaller (down to 1 μm) and then enlarge back to 2-3 μm on the top. Fig. 5.4 displays top and bottom scans of the sample around its edges. Top regions show gradual decrease in dendrite size from 2-3 μm , down to 1 μm

moving from the center to the down left due to thickness change, while the bottom area above the skull exhibits an abrupt increase in dendrite size up to 10 μm around the corner of the left edge because sample actually does not touch the Cu plate in that region. Fig. 5.5 summarizes the general trends in microstructure (i.e., dendrite size) with contour lines and SEM images. The smallest dendrites are found on the left center of the sample with 0.4 ~0.6 μm , and the largest ones are located around the center.

In conclusion, both wedge-shaped and arc-melted samples exhibit significant variations in dendrite size due to changes in cooling rates during solidification. While the changes in the former sample can be directly correlated with sample shape (and thus resulting cooling rates), the arc-melted sample showed unexpected variations. One possible explanation for these variations is that radiation cooling may become quite effective from the top of the arc-melted sample leading to small dendrites there. Finite element modeling was applied to confirm this effect and is illustrated in Appendix C. As expected, the bottom also shows small dendrites due to the high conduction heat transfer there. On the other hand, loss of contact at the lower left precluded effective cooling in that region via conduction. Unfortunately, radiation does not appear to be effective at the lower left resulting in the lowest cooling, and hence the largest dendrites there.

In any case, these large variations in dendrite size are expected to influence the mechanical properties of the composite leading to significant variations across samples. This topic is further discussed in the next section.

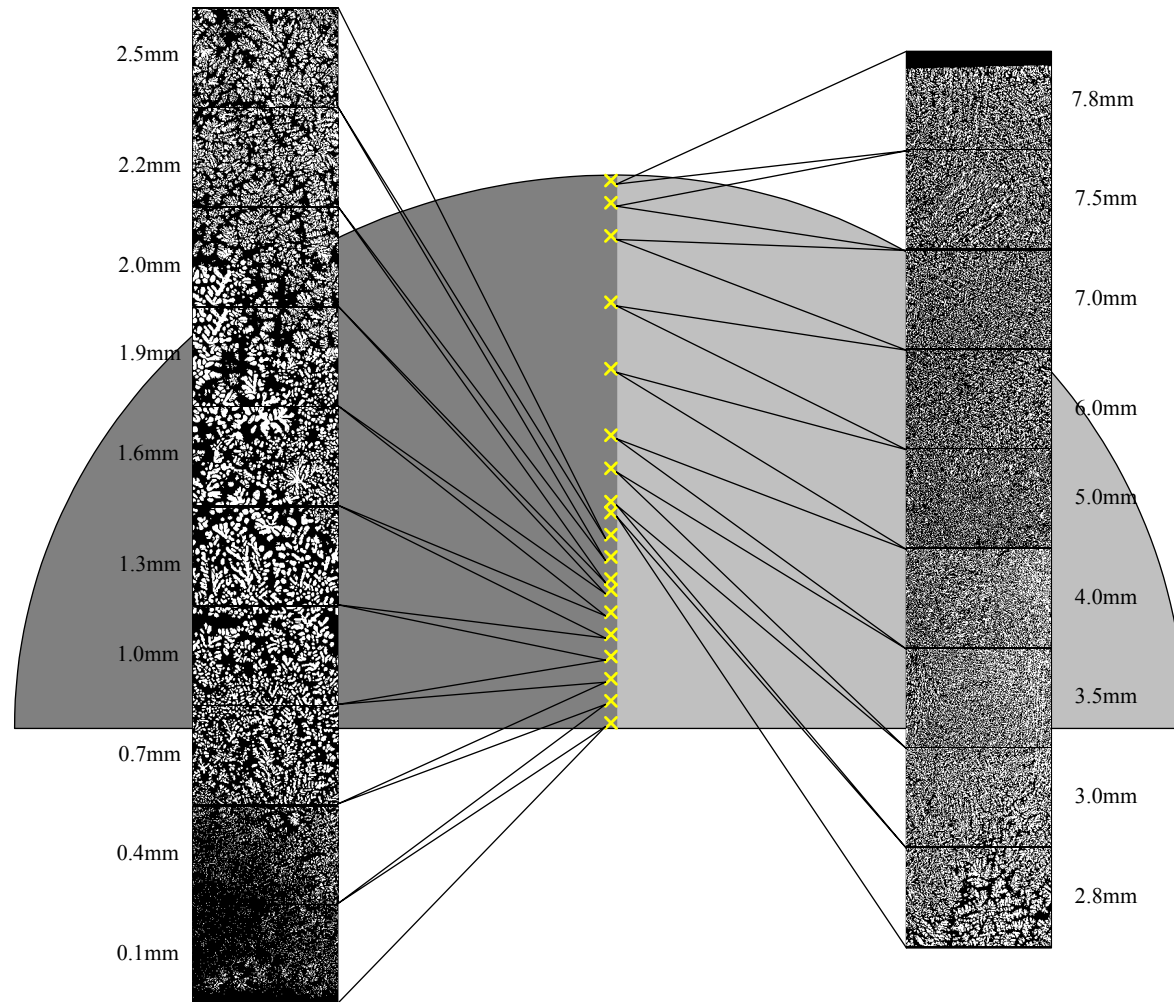


Fig. 5.3 Backscattered SEM images of the microstructure of the arc-melted, as-cast LM2A2 sample along its vertical axis. Here, the bright regions belong to the β phase while the dark area is the amorphous matrix. Numbers indicate distance from the bottom (magnification: x 1000).

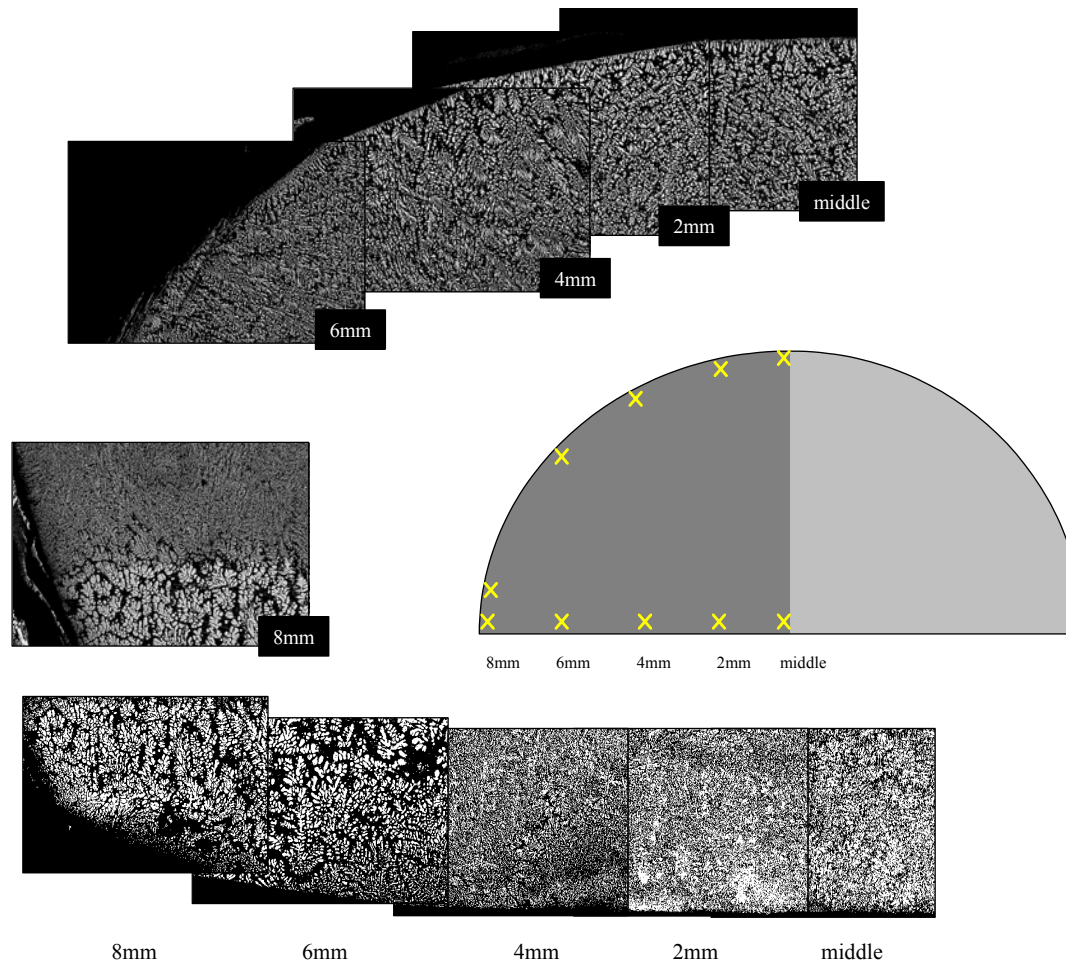


Fig. 5.4 Backscattered SEM images of the microstructure of the arc-melted, as-cast LM2A2 sample around its edges. Here, the bright regions belong to the β phase while the dark area is the amorphous matrix. Numbers indicate horizontal distance from the center (magnification: x 1000).

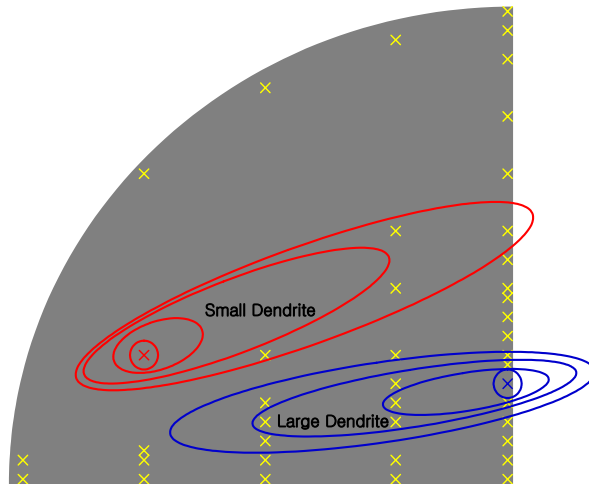
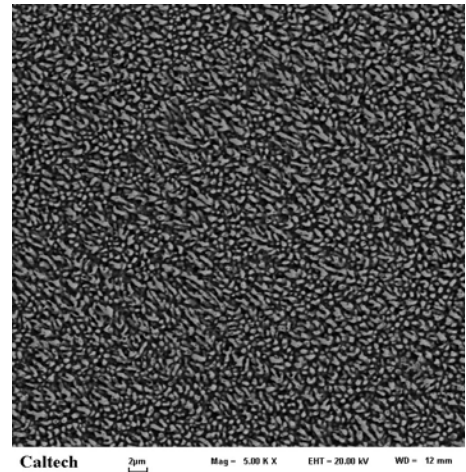
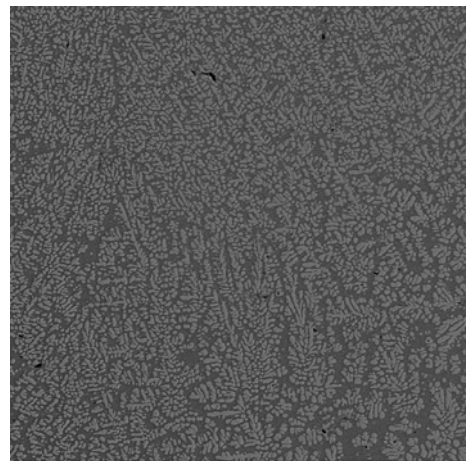


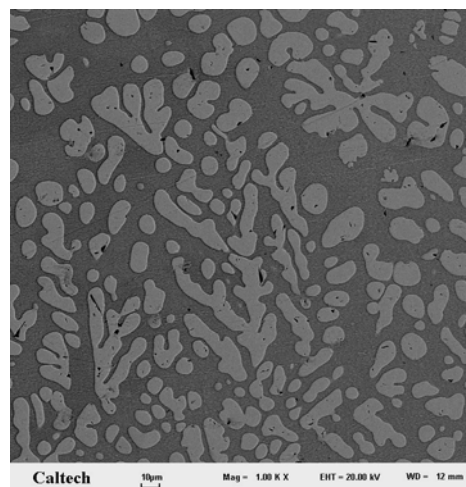
Fig. 5.5 Contour lines (not to scale) of the dendrite size distribution (left) and corresponding typical microstructure images (backscattered SEM) from the arc-melted sample.



a) Smallest dendrites (0.4~0.6 μm)
(x 5000)



b) Middle size dendrites (2~4 μm)



c) Largest dendrites (8~12 μm)

5.1.3 Yield Strength vs. Dendrite Size

The SEM study of LM2A2 samples revealed that dendrite size and shape of the β phase are very sensitive to cooling rate and direction, whereas their volume fraction remained quite stable at around $40\% \pm 4\%$ (based on the analysis of about 40 micrographs). A key question is how these different microstructures affect the mechanical properties of the composite such as yield strength. Because the β phase is very sensitive to processing conditions and it is difficult to apply systematically different cooling rates in each sample, an indirect procedure of deducing yield strength was used from Vickers hardness measurements. A diamond tip was pressed into various parts of the button and hardness and tensile yield strength values were calculated by the following equation [8]:

$$\text{Hardness} = \frac{(1.854 \times \text{Weight})}{d^2} \quad (3)$$

$$\text{Tensile Yield Strength} = \frac{\text{Hardness}}{3} \quad (4)$$

(d = diagonal length of square indents)

Fig. 5.6 shows Vickers indents in different areas with varying dendrite size. Hardness values range from 4.1 to 7.1 GPa and calculated yield strength varies from 1.4 to 2.4 GPa when dendrite size changes between 2 to 10 μm . These results are compared to earlier tension test data from other *in-situ* composites. Both types of yield strength data clearly exhibit a marked decrease with increasing dendrite size in analogy to the classical Hall-Petch relation found in polycrystalline metals where yield strength decreases with increasing grain size. The discrepancy between the tension test results

and the Vickers indentation data suggests a possible problem with calculating yield strength from indent size in these composites, likely due to their inhomogeneous structure. Nevertheless, all yield strength data clearly demonstrate a significant decrease in yield strength when dendrite size increases. A natural question at this point is the “ideal” dendrite size that maximizes both yield strength and ductility, a question to be addressed in future work.

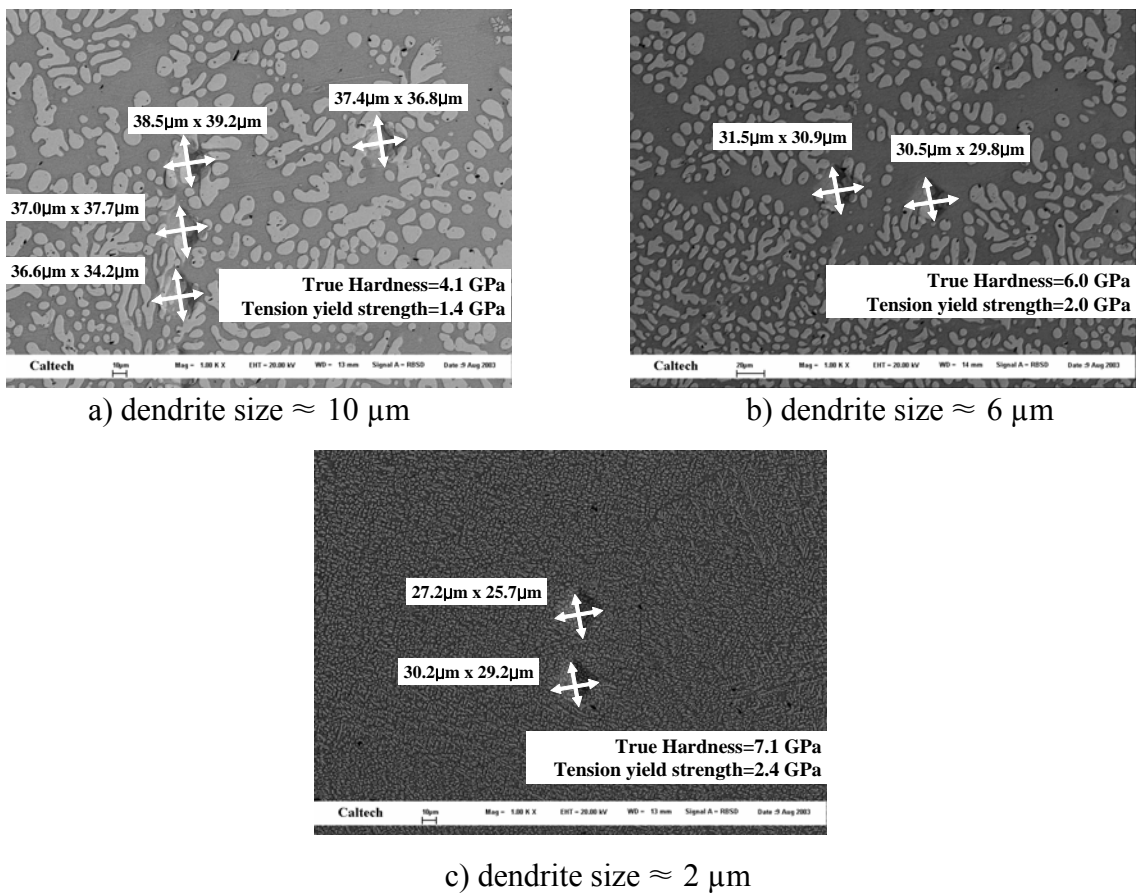


Fig. 5.6 Vickers indents (marked as white arrows) and the corresponding hardness and yield strength data for different regions within an arc-melted button.

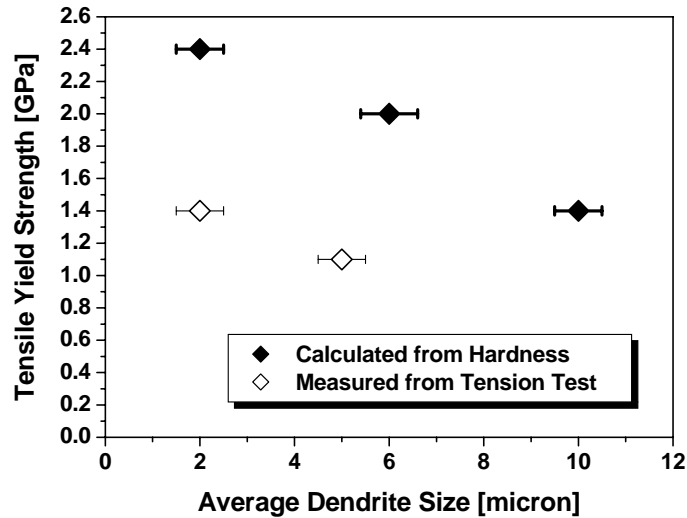


Fig. 5.7 Tensile yield strength calculated from Vickers hardness data vs. average dendrite size compared to tension tests of earlier composites from Caltech (5 μm dendrite size average) and Howmet (2 μm average) materials [4].

5.2 Phase Evolution of *In-situ* β Phase Composites

The accidental discovery of β phase stiffening (see Chapter 4) led to a systematic study of the effect of heat treatment (HT) on this phase's properties, both in monolithic and composite forms. Two kinds of HT experiments were carried out and the details are presented below: (i) cyclic heating up to the melting temperature of the composite; and (ii) isothermal holds at 300°C and 600°C of both the monolithic β phase and composite. 300°C was chosen to avoid crystallization in the matrix (its glass transition temperature is about 350°C) and isolate events occurring only in the β phase. 600°C is between the crystallization and melting temperatures of the matrix; thus, HT at this temperature might lead to changes in both the dendrites and the matrix. It will be shown below that only the β phase undergoes phase evolution at 300°C, while crystallization takes place in the

amorphous matrix at 600°C without any appreciable change in the β phase. Results from the 300°C isothermal holds are especially interesting since they point to the intrinsic instability of the β phase below the glass transition temperature of the amorphous matrix, a regime where these composites are likely to be used in applications. Phase analysis during and after HT were performed using either laboratory X-rays (with Cu $K\alpha$ radiation) or high energy synchrotron X-rays for deeper penetration (see Chapter 2 for details). Samples consisted of arc-melted LM2A2 buttons machined into 3 mm diameter x 35 mm height cylindrical samples using Electrical Discharging Machining (EDM). Oxidation layers from EDM cutting were removed by mechanical polishing.

5.2.1 LM2 Composite Phase Evolution

Differential Scanning Calorimeter (DSC) data from an LM2 ($Zr_{56.2}Ti_{13.8}Nb_{5.0}Cu_{6.9}Ni_{5.6}Be_{12.5}$) composite are illustrated in Fig. 5.8. It is seen that the LM2 composite (top curve) and monolithic glass (bottom curve) behave very similarly to Vitreloy 1 (T_g : 350°C, T_L : 720°C, $T_x(1^{st})$: 400°C, $T_x(2^{nd})$: 450°C) [9]. The glass transition temperature (T_g) of the composite and monolithic glass are both \sim 350°C, whereas the 1st and 2nd crystallization temperatures are at \sim 400°C and 450°C, respectively. However, it is somewhat ambiguous to determine the liquidus line for both the composite and monolithic glass curves: T_L (matrix) is estimated at about: 750°C, but T_L (composite) could not be determined from DSC. Another interesting observation is that the monolithic β phase does not melt in the DSC up to 1300°C, and in another experiment using Electro Static Levitation (ESL) up to 1400°C. On the other hand, the β phase inside the composite melts below 1200°C as seen in *in-situ* X-ray diffraction studies (presented

below). These observations suggest that the β phase inside the composite may behave somewhat differently compared to the monolithic β phase. Nevertheless, the monolithic β phase offers valuable crystal structure and mechanical property data crucial for understanding the behavior of *in-situ* composites.

Fig. 5.9 shows XRD patterns of two LM2 monolithic β phase specimens: as-cast (left) and after an accidental heat treatment during CTE measurements. The latter exhibited significant stiffening and embrittlement. Here, the HT involved a heating rate of 3°C/min up to 350°C, a 30 minute hold, and a final cooling at the same rate as with heating. The total HT time was about 24 hours. Diffraction data reveal that lots of new diffraction spots appeared around the original BCC patterns suggesting new phase formation. More details with respect to this phenomenon are discussed below.

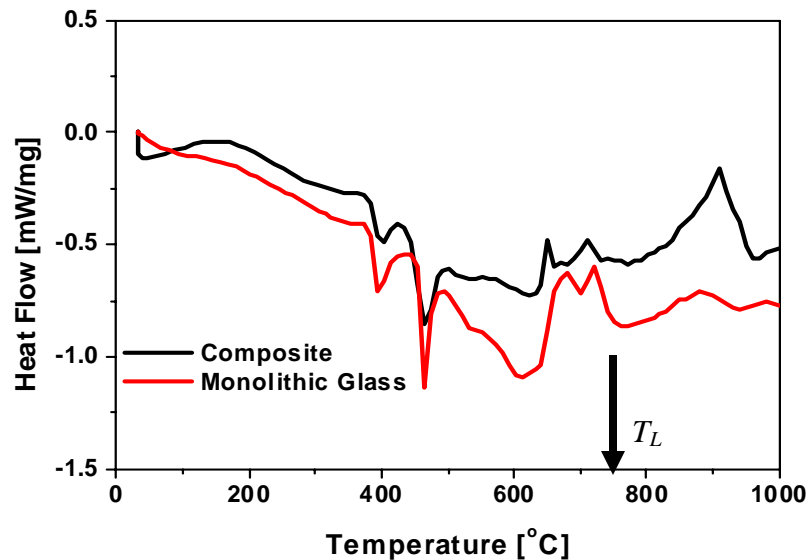


Fig. 5.8 DSC scans for the $Zr_{56.2}Ti_{13.8}Nb_{5.0}Cu_{6.9}Ni_{5.6}Be_{12.5}$ (LM2) composite and amorphous matrix under a constant heating rate of 20°C/min. (T_g : ~350°C, 1st T_x : ~400°C, 2nd T_x : ~450°C, T_L (matrix): ~750°C).

5.2.2 *In-situ* Cyclic Heating Experiment of LM2A2

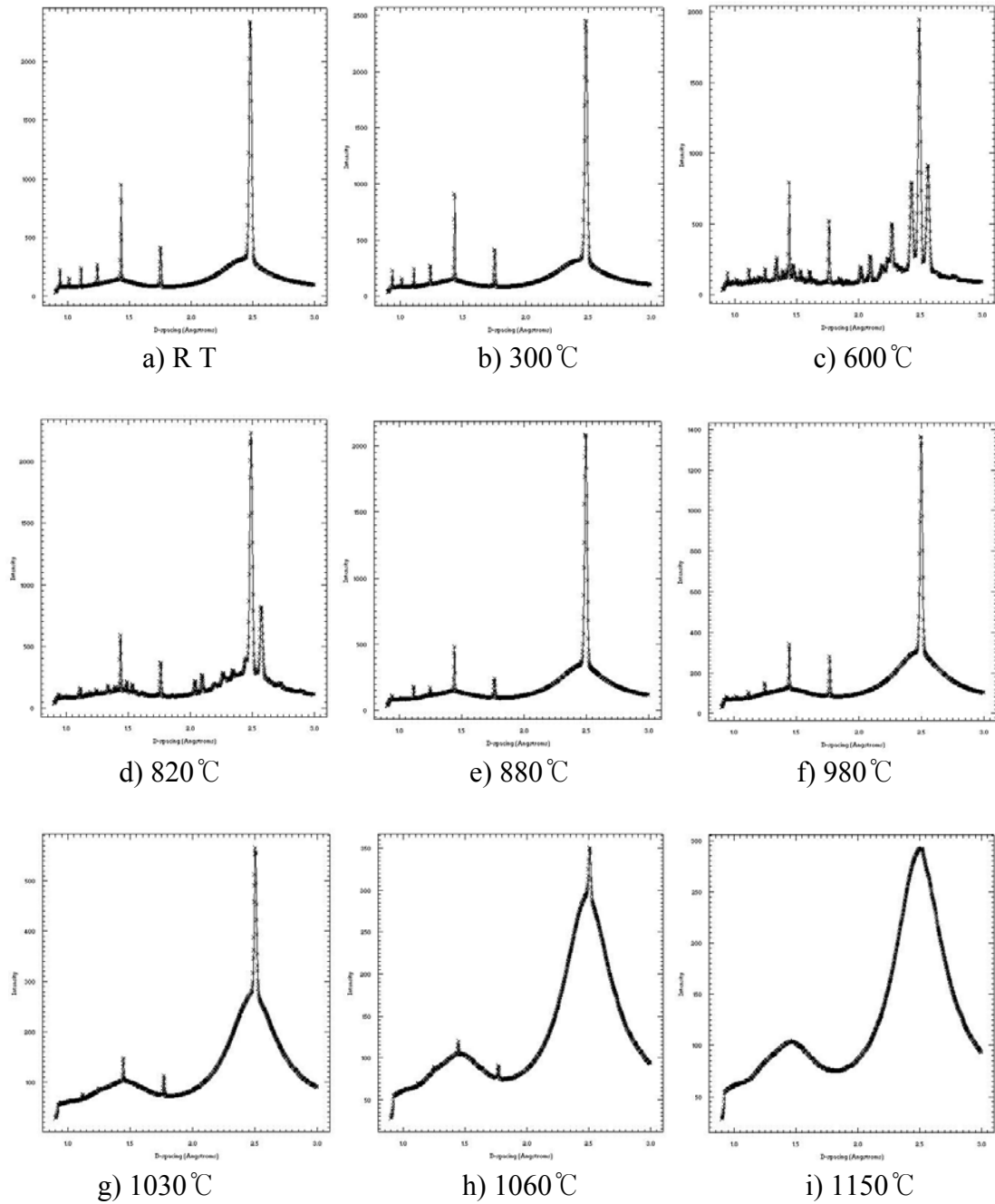


Fig. 5.10 Azimuthally integrated 2-D diffraction patterns during the *heating* of an *in-situ* β phase composite. Experiments were performed with high energy synchrotron XRD using a beam size of 100 x 100 μm .

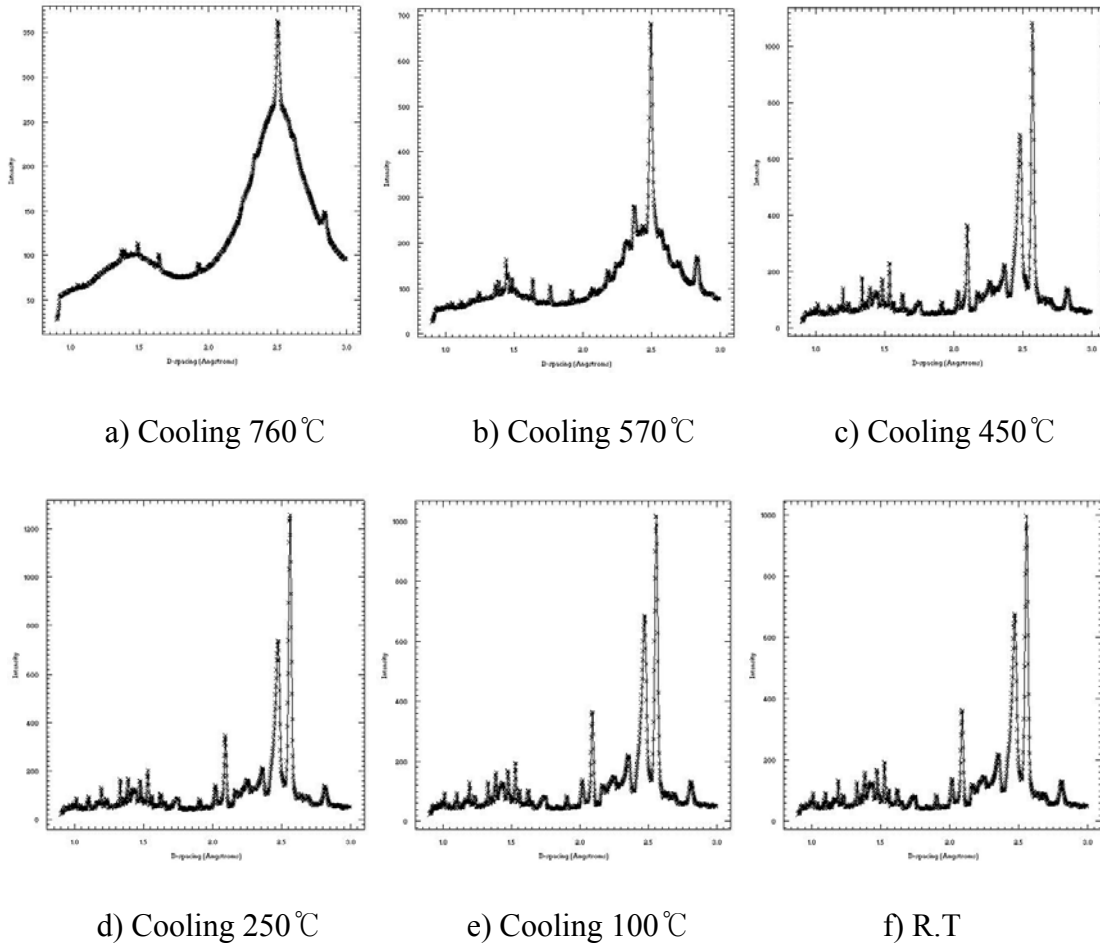


Fig. 5.11 Same as in Fig. 5.10, except the patterns were taken during the *cooling* stage of the experiment.

Figs. 5.10 and 5.11 show integrated diffraction patterns from an *in-situ* cyclic HT experiment (Fig. 5.10: during the heating stage, Fig. 5.11: during the cooling stage) of a β phase composite. The sample was sealed in a quartz tube to prevent oxidation at high temperature, and an IR furnace supplied heat at a rate of 50°C/min. The most important message from this experiment is that the BCC second phase remains stable throughout most of the temperature range until the whole composite melts at 1150°C (the solidus line seems to start after 800°C). Please also note that the cooling was achieved by simply

turning off the furnace (i.e., under air cooling conditions) leading to numerous crystallization peaks observed in the cooling stage (Fig. 5.11). This confirmation of the high temperature stability of the β phase placed additional significance on the isothermal heat treatment experiments presented below.

5.2.3 Isothermal Heat Treatment of LM2A2

It has been known that an isothermal HT, even below T_g , can change the mechanical properties of monolithic BMGs, e.g., by reducing their fracture strength [10]. In addition, the TTT diagram of Vitreloy 1 [11-13] exhibits no asymptotic line against crystallization, which means BMG can be crystallized even below T_g under proper HT time and other sample conditions. Thiagarajan and co-workers also reported that the embrittlement of BMG can take place even before crystallization due to a decomposition (or phase separation) process [14]. Phase separation in Vitreloy 1 has been scrutinized by Atom Probe Field Ion Microscopy (AP/FIM) [15] and Small Angle Neutron Scattering (SANS) [16-20]. The process was identifiable in SANS after several hours of HT at 350°C (= T_g of Vit.1). Therefore, due to the similarity between the amorphous matrix in *in-situ* composites investigated in the present study and Vit.1, it was important to maintain a relatively low HT temperature (300°C) not only to avoid the crystallization of the amorphous matrix, but also to exclude its decomposition and thus isolate effects solely due to the β phase reinforcements. Even though 18 hours of HT at 300°C might involve a certain degree of decomposition in the matrix, it was seen in Chapter 4 that the monolithic BMG with the same composition as the matrix in β phase composites remained amorphous after 18 hr HT at 300°C and its fracture strength did not change at

all. Therefore, it can be assumed that all the HT effects observed in *in-situ* composites at 300°C are likely due to phase evolution in the second phase reinforcement only.

Fig 5.12 and Fig 5.13 show as-cast and water-quenched *in-situ* composites before and after a 300°C HT. 2-D diffraction images clearly show amorphous rings (from the matrix), along with BCC patterns from the β phase reinforcements. Compared with the water-quenched sample, BCC rings are spottier in the as-cast sample, suggesting a larger grain size for the β phase in the latter. This is to be expected from the higher cooling rate likely attained in the water-quenched sample.

However, the effect of HT on both samples is similar. The main BCC peaks are mostly retained as HT time increases, but this process is accompanied with peak broadening, especially towards the end. There is also a clear overall peak height drop (compare, e.g., the changes in peak height for the 110). Overall, it appears that the BCC peaks are splitting, indicating a gradual phase transition from cubic into tetragonal-like phase. It is not clear yet whether this new phase is tetragonal or whether it consists of two BCC phases undergoing phase separation. Additional phase analysis is needed to clarify this issue. The unstable nature of the BCC β phase has long been suspected in these materials. The most dominant element in the β phase ($\text{Zr}_{71.1}\text{Ti}_{13.1}\text{Nb}_{13.4}\text{Cu}_{1.6}\text{Ni}_{0.8}$) is Zr which is HCP at room temperature (the α phase) and transforms into β (BCC) at 862°C. A similar trend is also known for Ti (transition at 880°C). On the other hand, Nb is a well known BCC (β phase) stabilizer in Zr-Ti alloys [4]. Therefore, the presence of these three elements as the majority of the β phase assures its structure as a metastable BCC at low temperatures. However, there is stored lattice energy in the β phase which can be

considered as the main source of the driving force for the cubic to tetragonal-like phase transition (or ordering) in this material.

In order to confirm that the new phase is the preferred low temperature ordering phase and not an intermediate phase before a more stable phase is reached, additional long term HT experiments were carried out at 300°C and 600°C. At each temperature, the HT was continued until no further changes in the diffraction patterns were observed. The results are displayed in Fig. 5.14. If the new phase was an intermediate phase, phase transformation kinetics would be expected to increase at 600°C. However, if it is an ordered phase at 300°C, there should not be much change in 600°C because order-disorder transition normally takes place at lower temperatures. This is exactly what happened during the long term HT experiment. At 600°C, neither any drop in peak intensity nor any appreciable peak broadening was observed. But, at 300°C, as was also seen in synchrotron data, BCC peaks became broader and the peak splitting was obvious. Therefore, it can be concluded that the β phase undergoes order-disorder transition at 300°C from cubic to a tetragonal-like phase. Lattice mismatch between BCC and the new phase and other microstrain effects due to the diffusion that accompanies the transition process would be possible reasons for peak broadening. If a nucleation process is dominant and continuous, then a small grain size for the ordered phase would be another reason behind peak broadening. Since the ordered phase has a shallower potential well, its shear modulus (curvature of the potential well) would be increased as ordering process is in progress, an effect that has been observed in ultrasonic measurements (see Section 4.2.3).

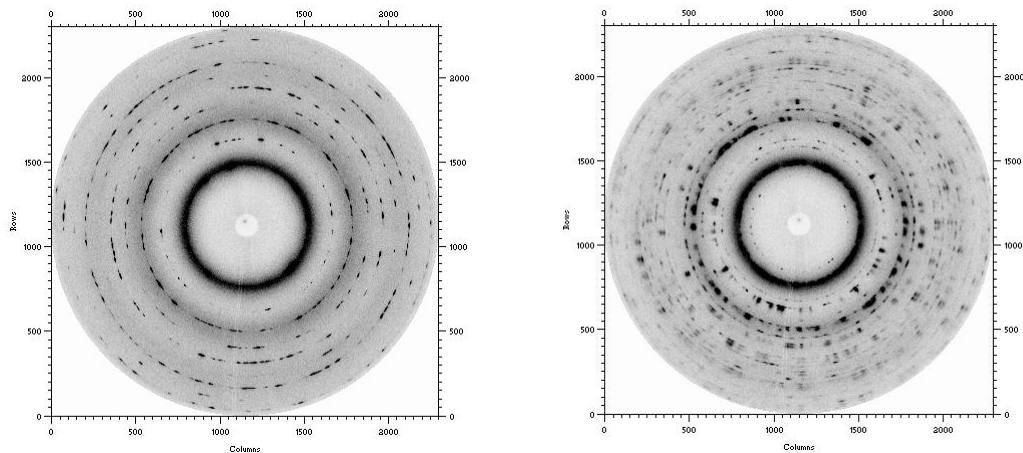
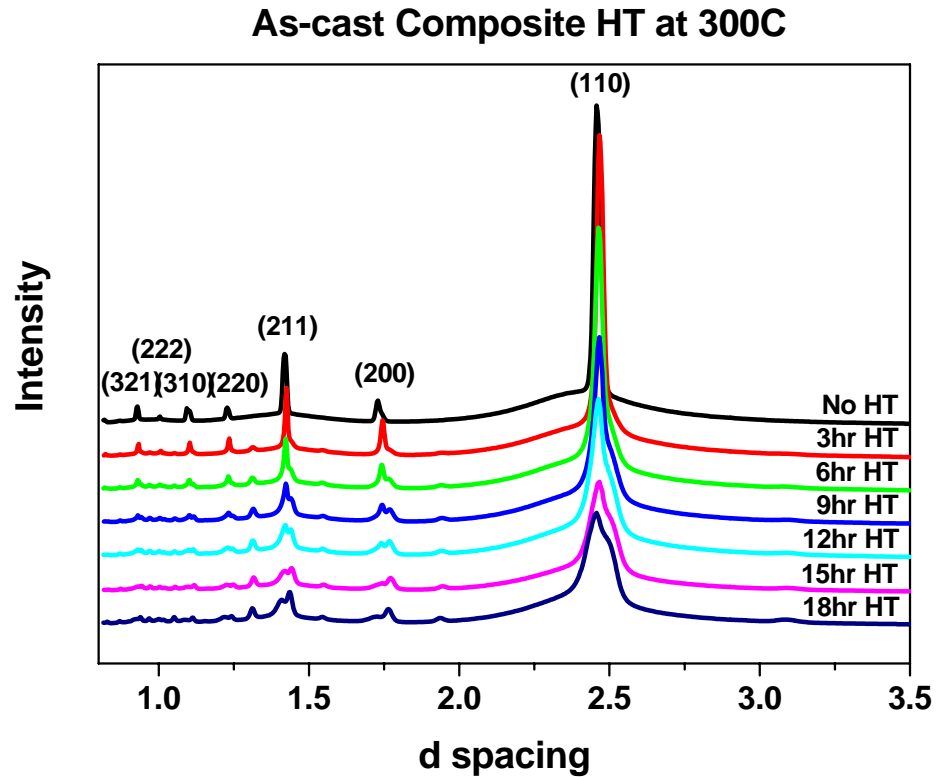


Fig. 5.12 Azimuthally integrated diffraction patterns of an as-cast *in-situ* composite (top) and sample 2-D patterns before (lower left) after its heat treatment at 300°C for 18 hours (lower right). The diffraction data were collected using high energy XRD at APS (see Chapter 2 for details).

Water-quenched Composite HT at 300C

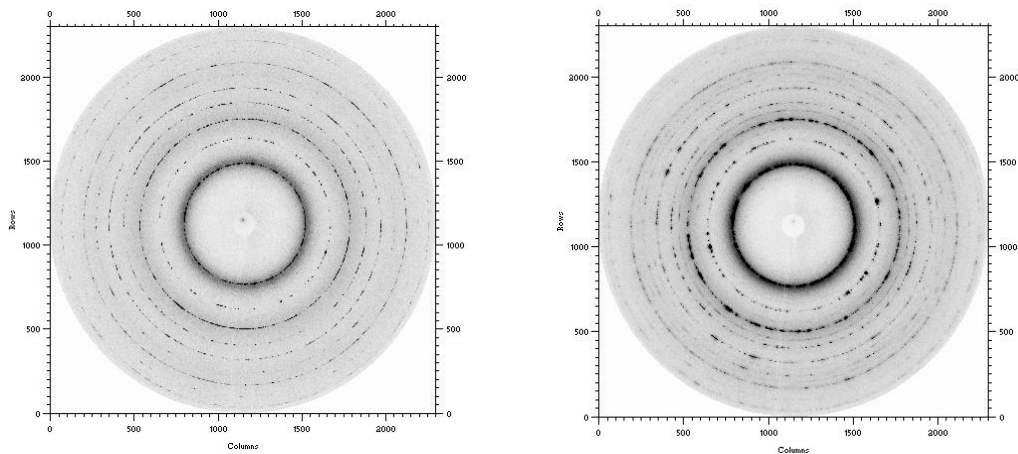
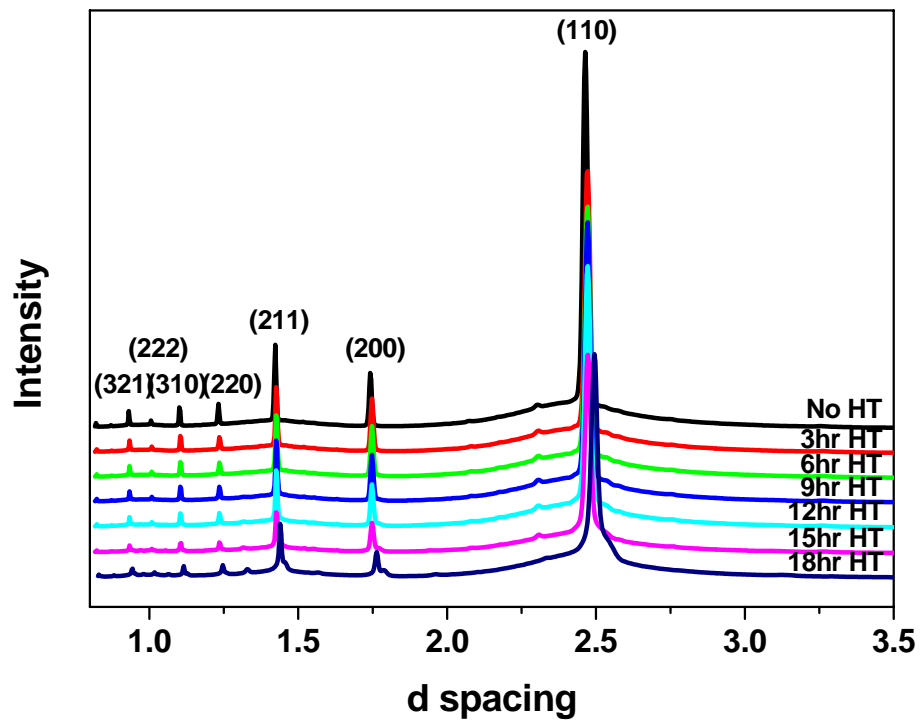


Fig. 5.13 Azimuthally integrated diffraction patterns of a water-quenched *in-situ* composite (top) and sample 2-D patterns before (lower left) after its heat treatment at 300°C for 18 hours (lower right). The diffraction data were collected using high energy XRD at APS (see Chapter 2 for details).

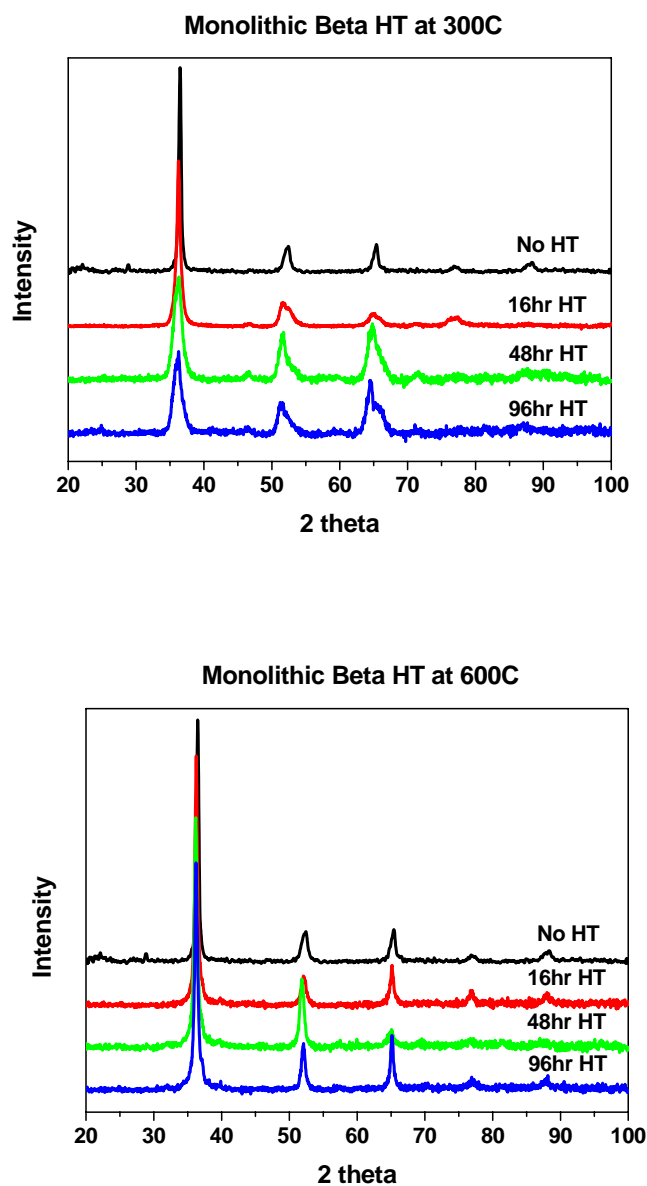


Fig. 5.14 Evolution of LM2A2 monolithic β phase diffraction patterns during long term HT at 300°C (top) and 600°C (bottom). The data were collected *ex-situ* using a laboratory X-ray machine with Cu $K\alpha$ radiation at Caltech. Note that more peak broadening and splitting is observed at 300°C while no appreciable changes are seen after HT at 600°C.

This ordering mechanism also explains why the water-quenched sample is more resistant to phase evolution. Since water-quenching can bring stable BCC configuration down to room temperature due to a fast cooling, it takes more energy to induce phase transformation in this stable BCC. In other words, the as-cast BCC phase at room temperature is more unstable than the water-quenched one because the phase stability of the as-cast sample is only dependent on compositional modification by the addition of the β phase stabilizer, Nb, but that of the water-quenched one is aided by fast cooling as well. Another reason would be the grain boundary effect. Elastically stored energy (the driving force for ordering) can be released more when incoherency is introduced by defects such as grain boundaries. As seen in 2-D diffraction images, the water-quenched sample has a finer grain size and there would be less chance to build up much of strain energy inside grains.

Another isothermal HT experiment at 600°C was conducted on a β phase composite. In this case, the phase evolution shown in Fig. 5.15 can be attributed to the crystallization of the amorphous matrix. At this temperature, the crystallization kinetics is very fast and the TTT diagram of Vit.1 suggests it takes only 100 sec before the onset of crystallization [11].

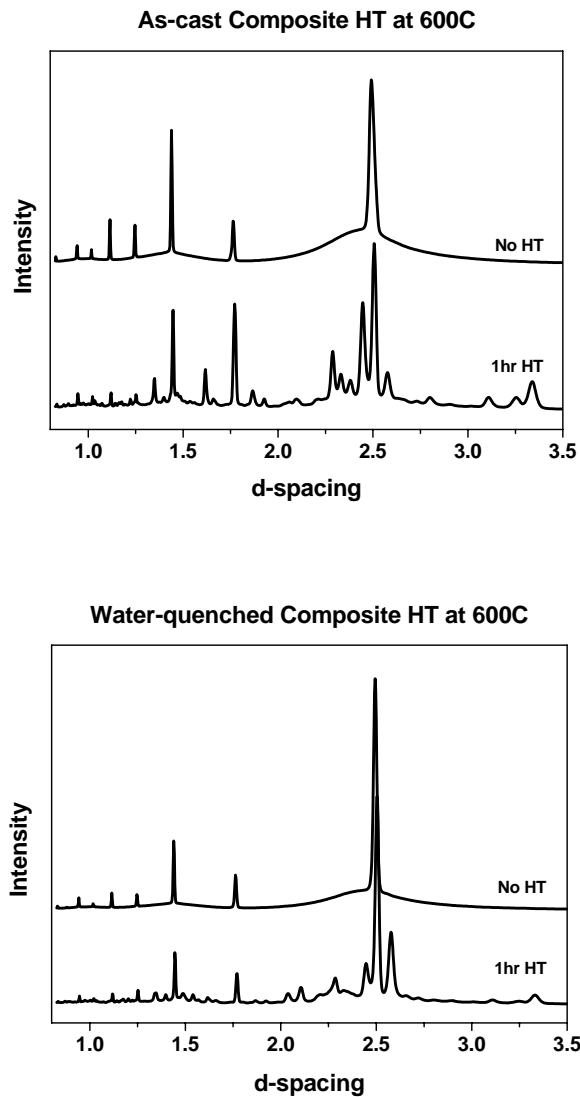


Fig. 5.15 Azimuthally integrated diffraction patterns of an as-cast (top) and a water-quenched (bottom) *in-situ* composite heat treated at 600°C for 1 hour. The experiments were conducted *in situ* using high energy XRD at APS.

Fig. 5.15 shows the two extremes of before and after crystallization for both types of composites. While the BCC β phase peaks are dominant before HT, many additional peaks are observed afterwards. In order to identify these new peaks, it was assumed that the crystallized matrix ($Zr_{42.2}Ti_{9.4}Nb_{3.2}Cu_{13.7}Ni_{10.7}Be_{20.8}$) is almost identical with Vit.1

($Zr_{41.2}Ti_{13.8}Cu_{12.5}Ni_{10.0}Be_{22.5}$), except for the existence of Nb. There have been many studies of the crystallization behavior of Vit.1 [9, 21-22] and on diffusion mechanisms in metallic glasses [23-26]. Despite some minor discrepancy among these papers, there has been a general agreement in that Zr_2Cu and Be_2Zr are the major crystalline phases [27-28]. Using this information as a basis, two basic criteria were chosen when matching the new peaks to known phases in the powder diffraction database: heat of mixing (thermodynamics), and the diffusion constant and the amount of each element (kinetics). If there were multiple candidates for small peaks, diffusivity and heat of mixing criteria were applied to narrow down the choices. Besides the two major phases (Zr_2Cu and Be_2Zr), two minor ones ($Be_{17}Nb_2$ and $NiTi$) offered the best matches. However, this process was done under the assumption that there are no unknown ternary phases possible in this alloy, a possibility that cannot be entirely excluded. Fig. 5.16 shows the final peak identification results.

| component | ΔH^{mix} (KJ/mol) |
|-----------|------------------------------|
| Zr-Ni | -49 |
| Zr-Be | -43 |
| Ni-Ti | -35 |
| Ni-Nb | -30 |
| Ti-Be | -30 |
| Nb-Be | -25 |
| Zr-Cu | -23 |

(a)

| Component | D (cm ² /s) |
|------------|------------------------|
| Be (20.8%) | 1.01E-12 |
| Zr (42.2%) | 1.58E-14 |
| Ti (9.4%) | 4.48E-15 |
| Cu (13.7%) | 2.68E-18 |
| Ni (10.7%) | 4.40E-24 |
| Nb (3.2%) | 4.23E-32 |

(b)

Table 5.1 Heat of mixing among matrix elements (a) [29] and diffusivity data (b) at 350°C [30]. Tracer self diffusivity data except for Be, which was measured in Zr solvent atmosphere. Real Be diffusivity: $D_{Be}(T_g) = 1.5 \times 10^{-15}$ cm²/s, $D_{Be}(T_e) = 2.0 \times 10^{-6}$ cm²/s [24]. Considering diffusivity and heat of mixing Be_2Zr phase should form first and it agrees with other results [12].

Crystallized LM2A2 Composite after 1hr HT at 600C

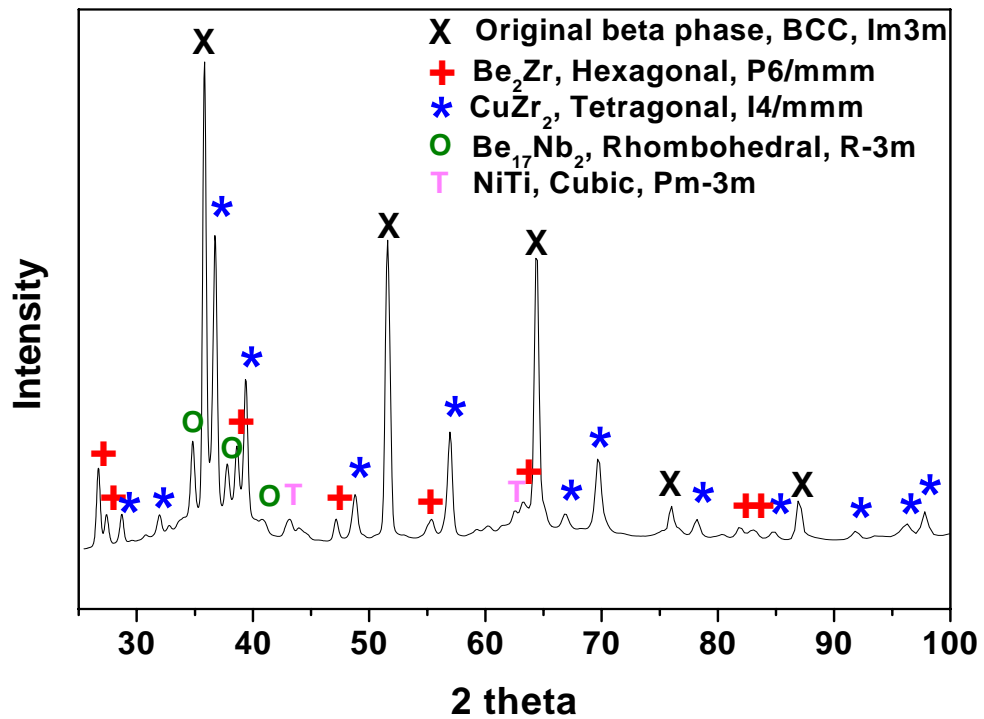
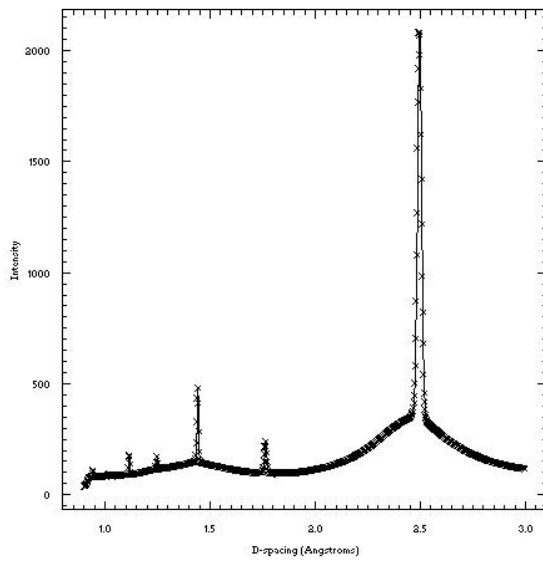


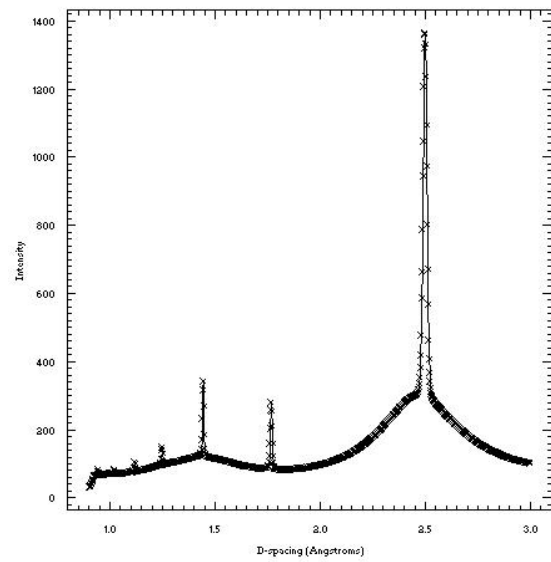
Fig. 5.16 Phase distribution in the LM2A2 composite after 1 hr HT at 600°C.

(One major difference from other crystallization studies [9, 21-22] was to have Nb in the alloy).

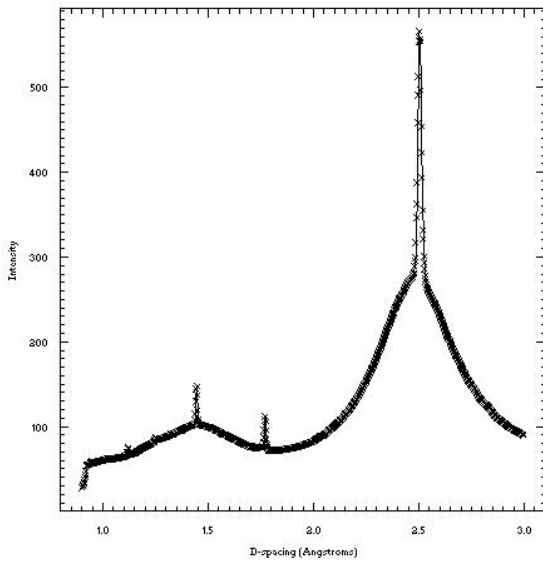
5.3 Pseudo Binary Phase Diagram for *In-situ* β Phase Composites



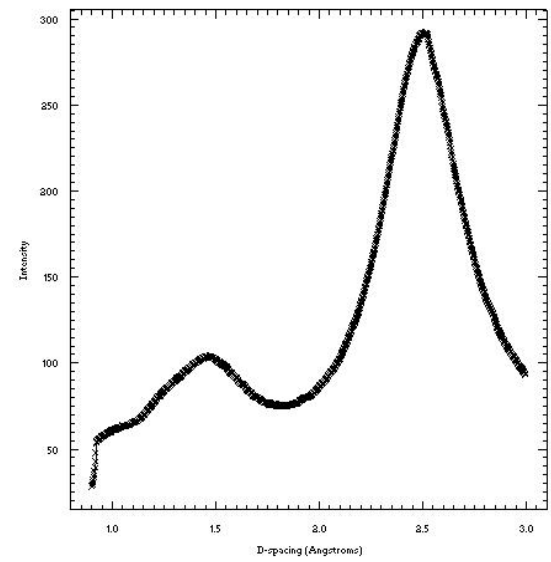
(a) 880°C

Liquid: 65%, β Phase: 35%

(b) 980°C

Liquid: 74%, β Phase: 26%

(c) 1030°C

Liquid: 82%, β Phase: 18%

(d) 1150°C

Liquid: 100%, β Phase: 0%

Fig. 5.17 Synchrotron X-ray diffraction data used in determining phase volume fraction. The areas of crystalline peaks and amorphous background were calculated through image analysis.

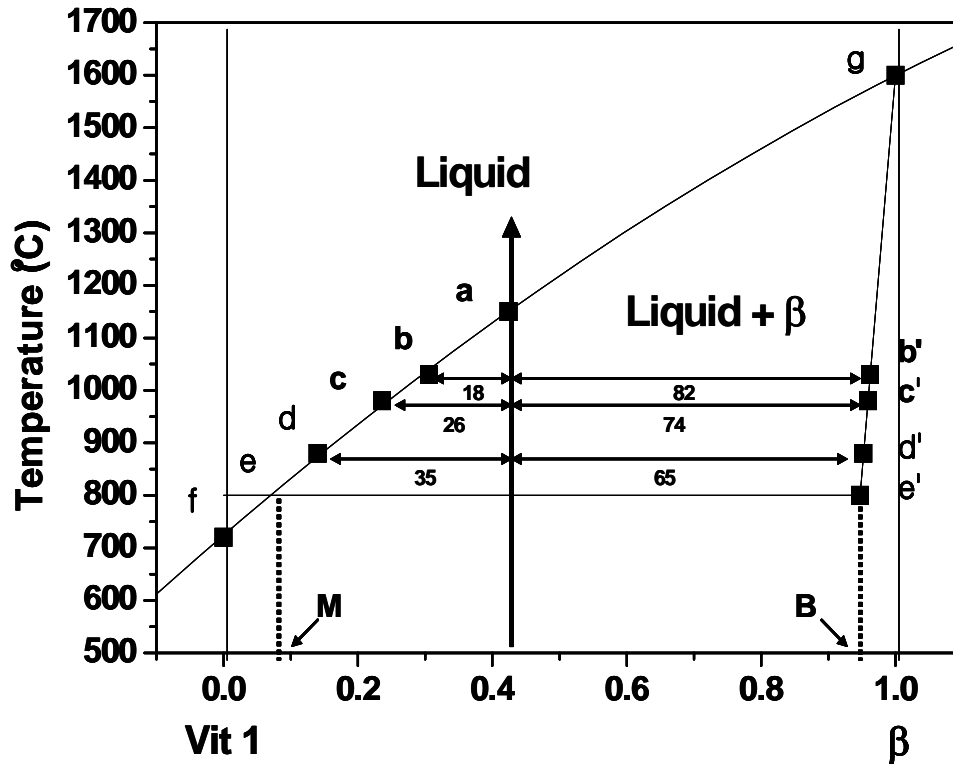


Fig. 5.18 Pseudo binary phase diagram for *in-situ* β phase composites. **M** and **B** represent the glassy matrix and the β phase, respectively. The Vitreloy 1 alloy, $(Zr_{75}Ti_{25})_{55}(Be_{50}(Cu_{55}Ni_{45})_{50})_{45}$ and the monolithic β phase, $Zr_{75}(TiNb)_{25}$ are chosen as binary axes. The *in-situ* composite, $(Zr_{75}(TiNb)_{25})_{75}(Be_{50}(Cu_{55}Ni_{45})_{50})_{25}$ falls on $x=0.424$ as indicated by the arrow. The composition of **M** ($Zr_{42.2}Ti_{9.4}Nb_{3.2}Cu_{13.7}Ni_{10.7}Be_{20.8}$) and **B** ($Zr_{71.1}Ti_{13.1}Nb_{13.4}Cu_{1.6}Ni_{0.8}$) were measured via electron microprobe analysis. **M** sits on $x=0.076$ based on Be content of 20.8% compared with 22.5% of Vit 1, while **B** occupies $x=0.947$ according to the $ZrTiNb$ content $(97.6-55.0)/(100-55)$. The melting temperature of Vit 1 (720°C) and the $Zr_{75}(TiNb)_{25}$ β phase (1600°C) were deduced from literature [31-32].

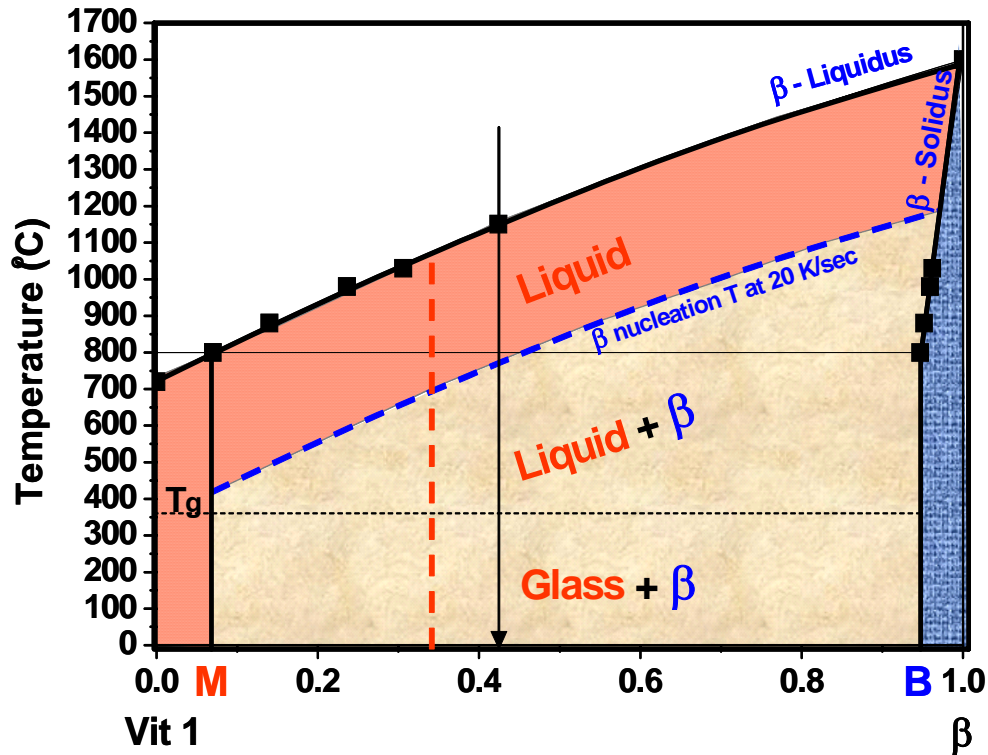


Fig. 5.19 Processing map for the Vit 1 and BCC β phase alloys. M represents the solubility limit of the β phase alloy within the glass forming region. Blue dashed line indicates the onset of dendritic phase under homogenous nucleation conditions. Materials shaded with yellow decompose into glass (M) and the BCC crystalline (B) phase when they cool down. The overall Nb content for the composite varies from 5.0 % to 7.5 % at the expense of Ti, yet bulk glass forming region extends further to the red dashed line, $(Zr_{75}Ti_{25})_{70}(Be_{50}(Cu_{55}Ni_{45})_{50})_{30}$, if Nb is not present in the alloy.

As seen in Section 5.2, the most important result obtained from the cyclic and isothermal heating experiments is that the monolithic β phase (or the β phase inside the composite) undergoes order-disorder transition at low temperatures (below T_g of the glassy matrix) whereas it remains as a stable BCC phase at high temperatures (above T_m of the glassy matrix). The characteristic of the low temperature ordering is extremely important because it determines the overall mechanical property of the composite as explained in Section 4.4. At one hand, the low temperature behavior of the β phase reveals a drawback of this composite by suggesting limits for its use temperature and time in real applications. On the other hand, the stable nature of the β phase at high temperatures offers an advantage since the stability of the β phase makes it possible to control the volume fraction and size of the dendrites using information from the thermodynamic quasi-equilibrium phase diagram and kinetics data from a TTT diagram. The term 'quasi' is used because glass formation itself involves a certain degree of kinetic process and it appears to follow an equilibrium diagram as long as the cooling rate is sufficient enough for glass formation.

The first step for the construction of the quasi-equilibrium phase diagram is to determine the volume fraction of each phase. Since the scattering intensity is proportional to the volume fraction of each phase, integrated areas under diffraction peaks (obtained from image analysis, hence the values are only approximate) are assumed to correlate with volume fraction. In order to confirm this method, room temperature data were analyzed and showed indeed that the 40/60 volumetric ratio between the BCC crystalline (β) and amorphous matrix phases. Fig. 5.17 shows that the β phase melting proceeds as temperature increases; each volume fraction here is calculated by the same method. The

pseudo binary equilibrium phase diagram was constructed with these volume fraction data and Fig. 5.18 exhibits all the details. C. P. Kim generated the room temperature two-dimensional ternary phase diagram showing phase partitioning in Fig. 4.1 [4], and Fig. 5.18 was constructed with temperature information based on his work. The Vitreloy 1, $(Zr_{75}Ti_{25})_{55}(Be_{50}(Cu_{55}Ni_{45})_{50})_{45}$, and monolithic β phase, $Zr_{75}(TiNb)_{25}$, are selected as binary axes, and the *in-situ* composite, $(Zr_{75}(TiNb)_{25})_{75}(Be_{50}(Cu_{55}Ni_{45})_{50})_{25}$, is marked with the arrow in the middle of diagram. As the Vitreloy 1 and monolithic β phase allow a certain level of solubility of each other, the actual glassy and crystalline phase compositions inside the composite turn out to be **M** ($Zr_{42.2}Ti_{9.4}Nb_{3.2}Cu_{13.7}Ni_{10.7}Be_{20.8}$) and **B** ($Zr_{71.1}Ti_{13.1}Nb_{13.4}Cu_{1.6}Ni_{0.8}$) and are marked. The β phase lattice parameter values deduced from diffraction data increase above 800°C (beyond the nominal thermal expansion effect) which suggests the reduction of small atom solubility, i.e., the Be content decreases. The data points, b' , c' , and d' are interpolated from e' and g . The melting point of Vitreloy 1 (f) and monolithic β phase (g) were taken from literature [31-32]. Since the composite chemical composition is known and the β phase solidus line is fixed, the β phase liquidus line could be calculated. As the glass volume fraction changes to 65%, 74%, 82% and 100% at 880°C, 980°C, 1030°C and 1150°C, respectively, data points of a , b , c , and d are calculated according to the lever rule. The β phase liquidus line was extended to two extremes of each phase (f and g), and it shows very good agreement with one another.

This pseudo binary phase diagram (Fig. 5.18) is very important from processing point of view, because one can modify phase volume fraction by changing processing temperature and composition. However, in order to apply this diagram in the laboratory, a

more detailed description is needed as the β phase formation is quite sensitive to cooling rate. S. Mukherjee reported that the β phase dendrite starts to form at 780°C with about 400°C undercooling if at the cooling rate is 20 K/sec under homogenous nucleation conditions [2]. C. P. Kim formed bulk glass up to the composition of $(Zr_{75}Ti_{25})_{70}(Be_{50}(Cu_{55}Ni_{45})_{50})_{30}$, when Nb is absent [4], but once β phase is stabilized by the addition of Nb up to 7.5%, then materials shaded with yellow in Fig. 5.19 decompose into glass (M) and the BCC crystalline (B) phase. The dendrite formation temperature (blue dashed line) and the maximum bulk glass forming region without Nb (red dashed line) are marked in Fig. 5.19, and quasi-equilibrium phase diagram (Fig. 5.18) combined with these kinetic information resulted in a “processing map for *in-situ* composite” (Fig. 5.19.)

It now becomes possible to control dendrite size as well as volume fraction. As seen in Fig. 5.18, the volume fraction will be governed by the lever rule between M and B . On top of that, if the appropriate point is chosen in terms of temperature and composition, one can suppress dendrite growth with enhanced nucleation rate. For example, if the materials is held around 600°C~700°C at the composition of $x=0.28$ in Fig. 5.19, it is highly possible to obtain a finer dendritic composite. The exact processing conditions should be developed through experiments based on this map, and a series of composite processing is subject to future work.

This phase diagram also explains why a monolithic β phase behaves differently from that inside a composite. According to Fig. 5.19, β phase composition B should have 1.2 at% Be, yet the electron microprobe technique is not capable of detecting this little difference. Therefore, this small amount of Be is likely responsible for the slight difference in the behavior of the β phase in monolithic and composite forms.

5.4 Conclusions

Although the Zr-based *in-situ* composite is among the most promising BMG composites, its processing sensitivity and the unstable nature of its dendritic reinforcement became serious issues in the application of this material. The present study performed a systematic microstructure analysis and phase evolution investigation using SEM and synchrotron high energy X-ray diffraction to quantify microstructure and phase evolution during the casting and heat treatment of the *in-situ* composites.

Wedge- and button-shaped *in-situ* composites were studied and it was found that the dendrite size is very sensitive to processing conditions and can vary even in one button from 0.4 μm to 12 μm . The arc-melted button showed that the volume fraction of dendrites remains around 40% regardless of location, while the dendrite size varies by one order of magnitude. This observation suggests that the β phase formation is relatively stable thermodynamically, but is very sensitive to heat flux (i.e., cooling rate). The tensile yield strength was indirectly deduced from a Vickers hardness tests on the arc-melted button, and it showed a gradual decrease with increasing dendrite size. Therefore, it will be desirable to have as small dendrites as possible to increase the yield strength of the composite. However, too small a dendrite size will be likely be detrimental as it might preclude effective toughening of the composite. The “ideal” dendrite size is still a subject of speculation and is one of the important topics to be tackled in future research.

Besides the microstructure of the composite, phase stability of the reinforcement and the amorphous matrix became an important factor in the composite’s mechanical behavior. Through the cyclic and isothermal heating of *in-situ* composites, it was determined that the β phase remains as a stable BCC crystalline phase above the melting

temperature of the glassy matrix, but it undergoes an order-disorder phase transition below the glass transition temperature of the matrix. It is not clear yet whether this ordered phase has a tetragonal unit cell or it involves a phase separation of two BCC crystalline phases. Whatever the case might be, it has been shown that the shear modulus of the β phase increases accompanied with a reduction in ductility, leading to the embrittlement of the composite.

One of the most important results of this study is the construction of the ‘quasi-equilibrium phase diagram’ of β phase composites, because this diagram provides the fundamental guide in composite design. For instance, a desired volume fraction can be achieved by the appropriate processing conditions in terms of hold temperature and overall composition. On top of that, the kinetic information about the onset of β phase formation will make it possible to even control dendrite size at a given volume fraction by suppressing dendrite growth rate. Therefore, it is feasible to process a much finer dendritic composite without applying a fast cooling rate. This is a very attractive processing method because it is relatively independent of processing time, and it avoids the formation of casting pores which have caused embrittlement of the composite in tension. Of course, the detailed processing conditions should be further tuned in additional experiments, a central topic in future research.

References

- [1] C. C. Hays, C. P. Kim and W. L. Johnson (2000). *Physical Review Letters* **84**(13): 2901-2904.
- [2] S. Mukherjee (2005). Study of crystallization behavior, kinetics and thermodynamics of bulk metallic glasses using noncontact electrostatic levitation technique. Caltech Ph.D thesis.
- [3] W. L. Johnson (2001). Unpublished research on heat transfer equation.
- [4] C. P. Kim (2001). Ductile phase reinforced bulk metallic glass composites formed by chemical partitioning. Caltech Ph.D Thesis.
- [5] S. Bossuyt (2001). Microstructure and crystallization behavior in bulk glass forming alloys. Caltech Ph.D thesis.
- [6] R. B. Dandliker, R. D. Conner and W. L. Johnson (1998). *Journal of Materials Research* **13**(10): 2896-2901.
- [7] H. Choi-Yim, R. Busch, U. Koster and W. L. Johnson (1999). *Acta Materialia* **47**(8): 2455-2462.
- [8] M. A. Meyers and K. Kumarchawla (1999). *Mechanical Behavior of Materials*.
- [9] Y. J. Kim, R. Busch, W. L. Johnson, A. J. Rulison and W. K. Rhim (1994). *Applied Physics Letters* **65**(17): 2136-2138.
- [10] M. Yan, J. F. Sun and J. Shen (2004). *Journal of Alloys and Compounds* **381**(1-2): 86-90.
- [11] J. Schroers, R. Busch, A. Masuhr and W. L. Johnson (1999). *Applied Physics Letters* **74**(19): 2806-2808.
- [12] J. Schroers, R. Busch and W. L. Johnson (2000). Crystallization of Zr₄₁Ti₁₄Cu₁₂Ni₁₀Be₂₃ melts. *Metastable, Mechanically Alloyed and Nanocrystalline Materials, Pts 1 and 2*. **343-3**: pp. 167-172.
- [13] Y. J. Kim, R. Busch, W. L. Johnson, A. J. Rulison and W. K. Rhim (1996). *Applied Physics Letters* **68**(8): 1057-1059.
- [14] P. Thiyagarajan (2003). *Journal of Applied Crystallography* **36**: 373-380.
- [15] R. Busch, S. Schneider, A. Peker and W. L. Johnson (1995). *Applied Physics Letters* **67**(11): 1544-1546.

- [16] J. F. Loffler, P. Thiyagarajan and W. L. Johnson (2000). *Journal of Applied Crystallography* **33**(1): 500-503.
- [17] J. F. Loffler and W. L. Johnson (2001). *Scripta Materialia* **44**(8-9): 1251-1255.
- [18] J. F. Loffler and W. L. Johnson (2000). *Applied Physics Letters* **76**(23): 3394-3396.
- [19] S. Schneider, U. Geyer, P. Thiyagarajan, R. Busch, R. Schulz, K. Samwer and W. L. Johnson (1996). Phase separation and crystallization in the bulk amorphous Zr_{41.2}Ti_{13.8}Cu_{12.5}Ni₁₀Be_{22.5} alloy. *Metastable, Mechanically Alloyed and Nanocrystalline Materials, Pts 1 and 2*. **225**: pp. 59-64.
- [20] S. Schneider, P. Thiyagarajan and W. L. Johnson (1996). *Applied Physics Letters* **68**(4): 493-495.
- [21] J. Schroers, W. L. Johnson and R. Busch (2000). *Applied Physics Letters* **76**(17): 2343-2345.
- [22] J. Schroers and W. L. Johnson (2000). *Journal of Applied Physics* **88**(1): 44-48.
- [23] U. Geyer, W. L. Johnson, S. Schneider, Y. Qiu, T. A. Tombrello and M. P. Macht (1996). *Applied Physics Letters* **69**(17): 2492-2494.
- [24] U. Geyer, S. Schneider, W. L. Johnson, Y. Qiu, T. A. Tombrello and M. P. Macht (1995). *Physical Review Letters* **75**(12): 2364-2367.
- [25] X. P. Tang, R. Busch, W. L. Johnson and Y. Wu (1998). *Physical Review Letters* **81**(24): 5358-5361.
- [26] X. P. Tang, U. Geyer, R. Busch, W. L. Johnson and Y. Wu (1999). *Nature* **402**(6758): 160-162.
- [27] L. L. Sun, T. Kikegawa, Q. Wu, Z. J. Zhan, L. M. Cao, L. M. Wang, G. J. Shao and J. Zhang (2002). *Journal of Physics-Condensed Matter* **14**(44): 11243-11247.
- [28] X. P. Tang, J. F. Loffler, W. L. Johnson and Y. Wu (2003). *Journal of Non-Crystalline Solids* **317**(1-2): 118-122.
- [29] A. R. Miedema, A. K. Niessen and F. R. d. Boer (1989). *Cohesion in metals: Transition Metal Alloys*.
- [30] J. Shackelford and W. Alexander, Eds. (1992). *Materials Science and Engineering Handbook*.

- [31] A. Peker (1994). Formation and characterization of bulk metallic glasses. Caltech Ph.D. Thesis.
- [32] Software Binary phase diagram data base.

CHAPTER 6

SUMMARY AND FUTURE WORK

Ever since the Zr-based bulk metallic glasses (BMGs) were developed in early 1990s, there have been many efforts to improve their ductility. Since it was known that multiple shear band formation is required to prevent catastrophic failure, *ex-situ* and *in-situ* composite systems were developed and these materials indeed showed improved ductility compared to monolithic BMGs.

This thesis studied two classes of BMG composites: (i) fiber reinforced *ex-situ* composites (with Mo, Ta, and Fe wire reinforcements), and (ii) *in-situ* β phase dendritic composites. The main goal of this research was to understand the deformation mechanisms in these BMG composites in order to eventually find out the best composite system.

The geometric constraint by as well as the material properties of the reinforcement plays an important role in toughening BMGs. Therefore, volume fraction, size, and shape of the reinforcement are the key factors in the geometric part, while the elastic constants and plastic behavior of the reinforcement are the crucial material parameters thought to be important for multiple shear band generation in the matrix. In this study, in general, low shear modulus reinforcements and/or a high volume fraction tended to be effective in increasing the ductility of BMGs. An often observed drawback was a reduced yield strength for composites (compared to the value found in monolithic BMGs – about 2 GPa), However, the critical values for each parameter are still unknown since the micromechanics of the initiation and interaction of shear bands in the matrix with reinforcements is still not well understood. The most important next step in BMG

composite research, therefore, should try to address this issue by employing model composites with simplified geometries (e.g., sandwich or concentric cylinder). The “ideal” BMG composite can only be designed after a deeper understanding of the composite micromechanics is reached.

Wire Composites: Based on previous studies of Vitreloy 1 / W fiber composites, Mo, Ta, and stainless steel (Fe) fibers were used in a Vitreloy 106 matrix to enhance its ductility. *In-situ* loading experiments with neutron diffraction were performed to monitor strain evolution of the reinforcements vs. applied stress, and these results were combined with Finite Element Modeling (FEM) to deduce the deformation behavior of the glass matrix. It was found that the reinforcements yielded first and started transferring load to the matrix which remained elastic throughout the whole experiment. Despite the significant increase in ductility with these fibers, those fiber composites were not suggested as good candidates in real applications due to their low yield strength. The unwanted annealing during the melt infiltration process seems to further lower the yield point of the fibers, and hence the composite. Most fibers also exhibited a weak interface with the matrix which reduced the load transfer between the two phases. Due to its high yield strength, high stiffness, and good interface strength, W fibers appear to be the best reinforcements for BMGs. Critical issues to be addressed in future fiber composite research include: (i) Determination of optimum fiber volume fraction; (ii) measurement of fiber-matrix interface strength for various systems to quantify the effect of the interface on overall composite performance.

In-Situ Composites: Vitreloy 1 based *in-situ* composites were developed in 1999 at Caltech, and the dendritic BCC β phase inside caused multiple shear band generation

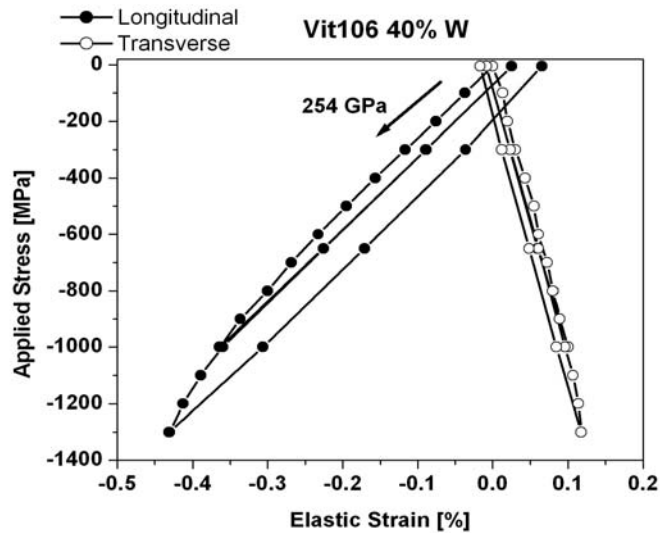
in the matrix increasing the overall ductility. In order to investigate the effective deformation mechanisms in these materials, diffraction data was combined with self-consistent modeling (SCM). The model successfully described phase specific behavior. The results revealed that dislocation slip of the β phase is the most prominent deformation mechanism, and that the β phase is highly anisotropic in the elastic regime. As seen in fiber composites, the β phase yielded first and transferred load to the matrix triggering multiple shear bands. The detailed micromechanical description of this process is still unknown and subject to future research.

In the course of this work, it was also discovered that the β phase is highly metastable at low temperatures and that it can easily be both hardened and stiffened by heat treatments below the glass transition temperature of the glassy matrix. This led to a systematic heat treatment study which investigated both the mechanical properties and phase evolution. It was found that the ductility of the composite decreased as the β phase experienced embrittlement and stiffening during heat treatment. Additional experiments on both monolithic β phase and matrix alloys confirmed that the drastic variations in the composite properties after heat treatment are basically due to changes in the β phase properties. It was also confirmed that the β phase experiences an order-disorder transition at low temperatures. The precise crystallographic analysis of this transition is subject to future studies. This stiffening behavior of the β phase was also supported by ultrasound measurements of its elastic constants. As heat treatment proceeds, the shear modulus of monolithic β phase increases by about 40% while its Poisson's ratio decreases slightly. The overall result is a likely reduction of dislocation slip due to a higher Peierls-Nabarro force which reduces the ductility of the β phase.

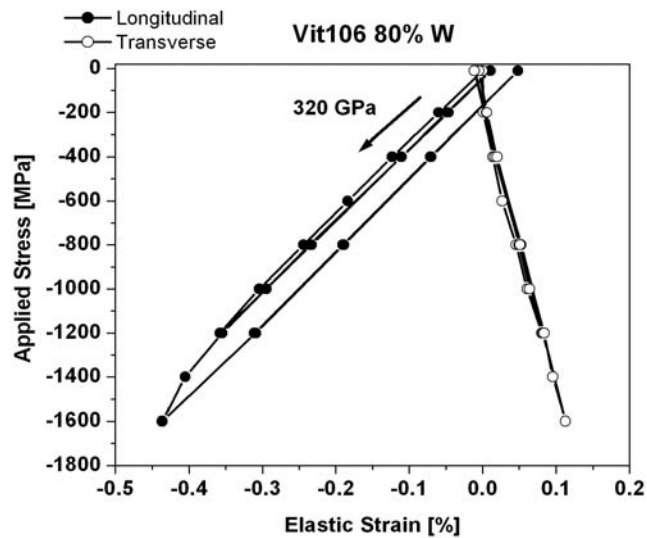
As the mechanical properties of the β phase composite are very sensitive to processing conditions, a microstructure study with a wedge-shaped sample and an arc-melted button showed that dendrite size varied from sub- μm to over $10\ \mu\text{m}$ across sample cross section while maintaining a fixed volume fraction of 40%. In contrast to low temperatures, the β phase was seen to be highly stable at high temperatures in a cyclic heating experiment during synchrotron X-ray diffraction. Combining all these results, it was possible to construct a quasi-equilibrium phase diagram for the β phase composites. This diagram provides the possibility of controlling both the volume fraction and size of β phase dendrites, through which the mechanical performance of the β phase composite can be manipulated. This phase diagram needs to be further populated with additional experiments and detailed processing conditions should be derived using its guidance. These are important future research topics for these composites.

Appendix A

Applied Stress vs. Elastic Strain of Fiber Composites from Neutron Diffraction

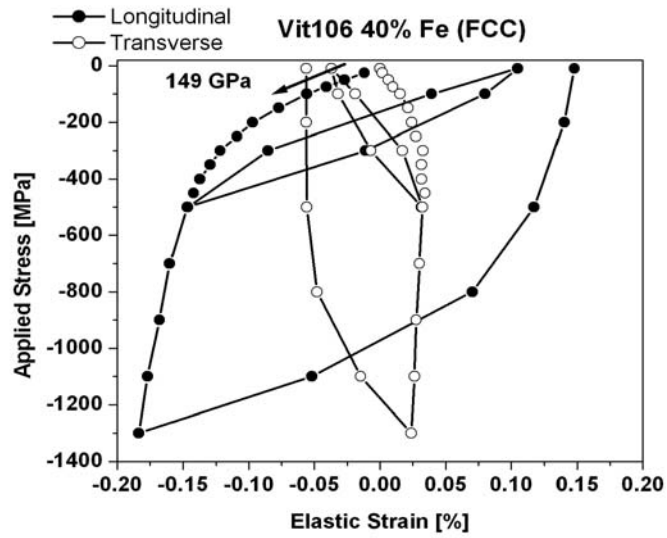


(a) Vit 106 BMG composite with 40% W

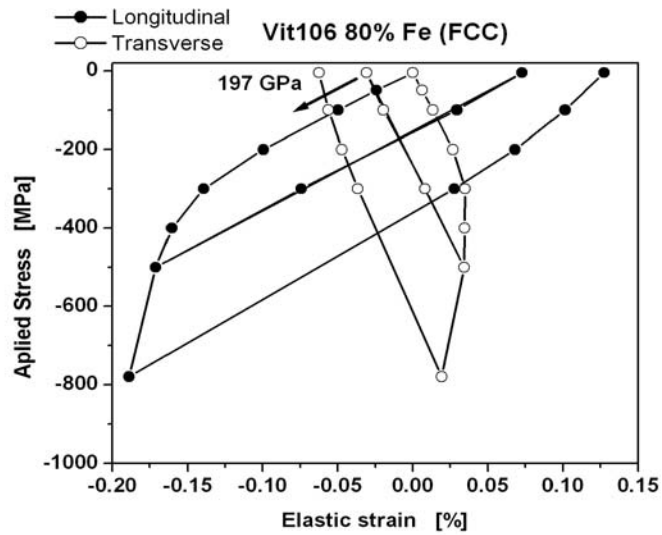


(b) Vit 106 BMG composite with 80% W

Fig. A.1 Applied stress vs. elastic strain data of W reinforced BMG composites from neutron diffraction. Both longitudinal and transverse strains are plotted.

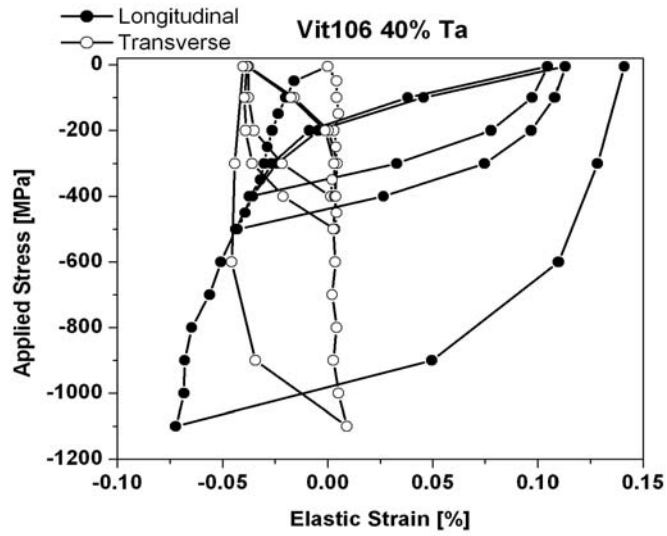


(a) Vit 106 BMG composite with 40% Fe

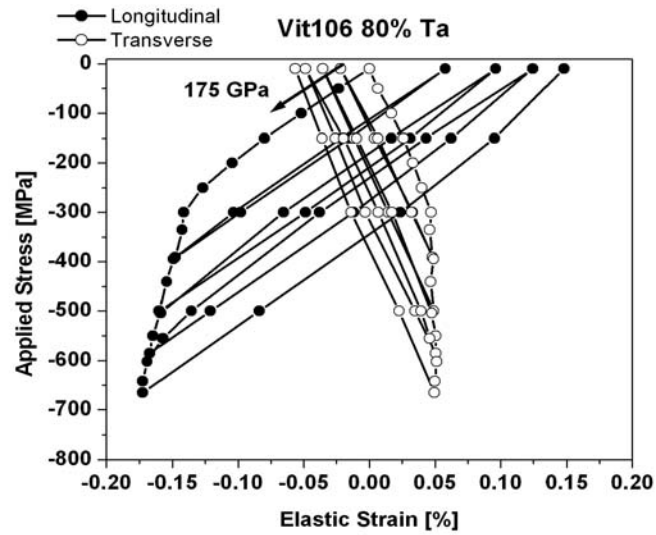


(b) Vit 106 BMG composite with 80% Fe

Fig. A.2 Applied stress vs. elastic strain data of Fe reinforced BMG composites from neutron diffraction. Both longitudinal and transverse strains are plotted.

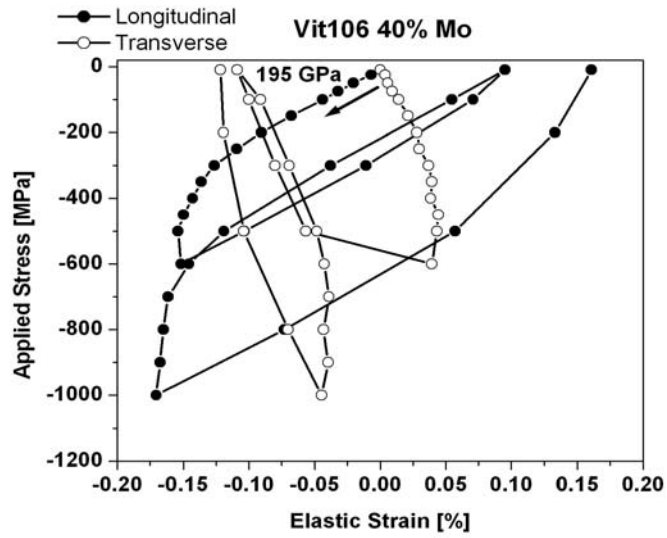


(a) Vit 106 BMG composite with 40% Ta

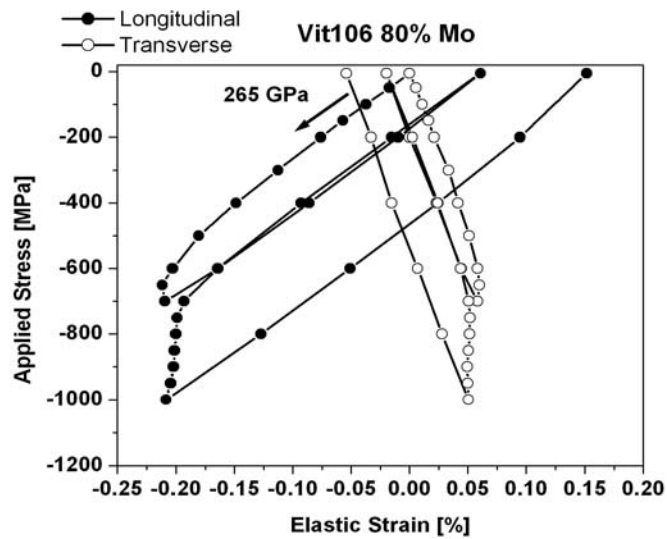


(b) Vit 106 BMG composite with 80% Ta

Fig. A.3 Applied stress vs. elastic strain data of Ta reinforced BMG composites from neutron diffraction. Both longitudinal and transverse strains are plotted.



(a) Vit 106 BMG composite with 40% Mo



(b) Vit 106 BMG composite with 80% Mo

Fig. A.4 Applied stress vs. elastic strain data of Mo reinforced BMG composites from neutron diffraction. Both longitudinal and transverse strains are plotted.

Appendix B

Validity of Calculating Three-Dimensional Phase Volume Fraction from a Two-Dimensional SEM Image

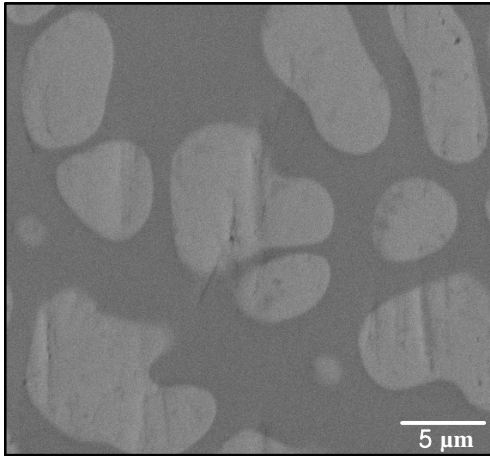


Fig. B.1 SEM image of an *in-situ* β phase composite: White area represents the BCC crystalline (β) phase while the black area is the amorphous matrix. Despite the dendritic nature of the BCC second phase, it is often observed in sphere-like or ellipsoidal shapes in many regions of two-dimensional images.

The complicated three-dimensional (3-D) geometry of dendrites makes the volume fraction analysis challenging, especially if the only data available is in the form of two-dimensional (2-D) slices from SEM images. Here, the observed area fraction can vary depending on the cutting angle and direction to obtain the 2-D images. For example, the area fraction of a sphere within a cube may be 79% ($\pi / 4$) if the cut is along the center, while its volume fraction is always 52%. However, this problem can be resolved if one analyzes many 2-D cuts so that there is an equal probability of making the cut anywhere between the edge and the center.

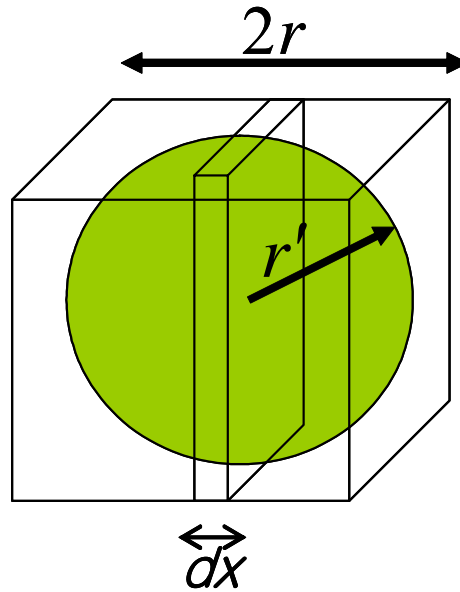


Fig. B.2 Sphere-cube model for second phase area and volume fraction calculation: The sphere inside of the cube represents the BCC crystalline phase inside the amorphous matrix, and radius of the sphere, r' is an arbitrary value between 0 and r . The cube is the reference volume over which integration is performed, and the thin slice with a thickness dx is the integral element.

The sphere-cube model is drawn in Fig. B.2, based on the sphere-like shape of most BCC dendrites observed in SEM images. In this model, the sphere size is treated as a variable, and the probability of cutting the sphere is all equal from the edge to the center. First of all, sphere-to-cube volume ratio is calculated:

$$\frac{V_{sphere}}{V_{cube}} = \frac{\frac{4}{3} \pi r'^3}{(2r)^3} = \frac{\pi}{6} \left(\frac{r'}{r} \right)^3 \quad (\text{B.1})$$

The next step is to calculate circle-to-square 2-D area ratio. Since cutting is a random process, it is important to find out the average value of the circle area.

$$\bar{A}(x) = \frac{\int_{-r}^r A(x) dx}{\int_{-r}^r dx} = \frac{\int_0^r \pi (r'^2 - x^2) dx}{\int_0^r dx} \quad (\text{B.2})$$

$$\bar{A}(x) = \frac{1}{r} \left[\pi r'^2 x - \frac{\pi}{3} x^3 \right]_0^{r'} = \frac{1}{r} \frac{2}{3} \pi r'^3 \quad (\text{B.3})$$

Then, the area fraction is given as:

$$\frac{\bar{A}_{circle}}{A_{square}} = \frac{1}{r} \frac{2}{3} \pi r'^3 / 4r^2 = \frac{\pi}{6} \left(\frac{r'}{r} \right)^3 \quad (\text{B.4})$$

Equation (B.1) is equal to (B.4)

$$\frac{V_{sphere}}{V_{cube}} = \frac{\bar{A}_{circle}}{A_{square}} \quad (\text{B.5})$$

Therefore, as long as the 2-D analysis is performed over a reasonably large area to ensure the average value is captured, it is valid to estimate the 3-D volume fraction from a 2-D SEM image analysis. It is also worth noting that a more rigorous integration proved that the relation shown in equation (B.5) also holds true regardless of inclusion shape and number [1], which means that the spherical shape assumption for the dendrites is not required.

Appendix C

Finite Element Modeling of Heat Transfer in an Arc-melted Button

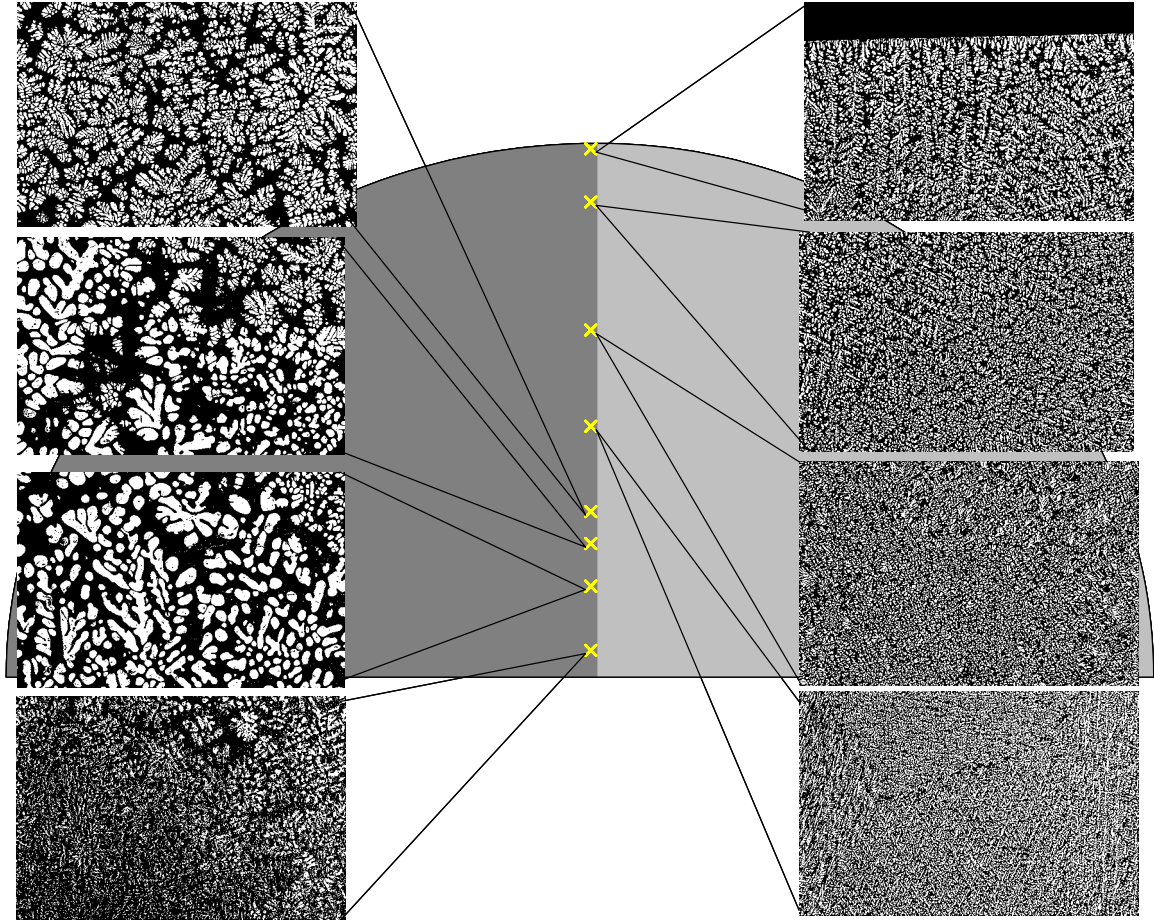


Fig. C.1 Backscattered SEM images of the microstructure of the arc-melted *in-situ* β phase button along its vertical axis. The radius of the sample is 7.8 mm, and dendrite size varies from 1 ~ 12 μm along the vertical axis. (Modified from Fig. 5.3, magnification: x 1,000)

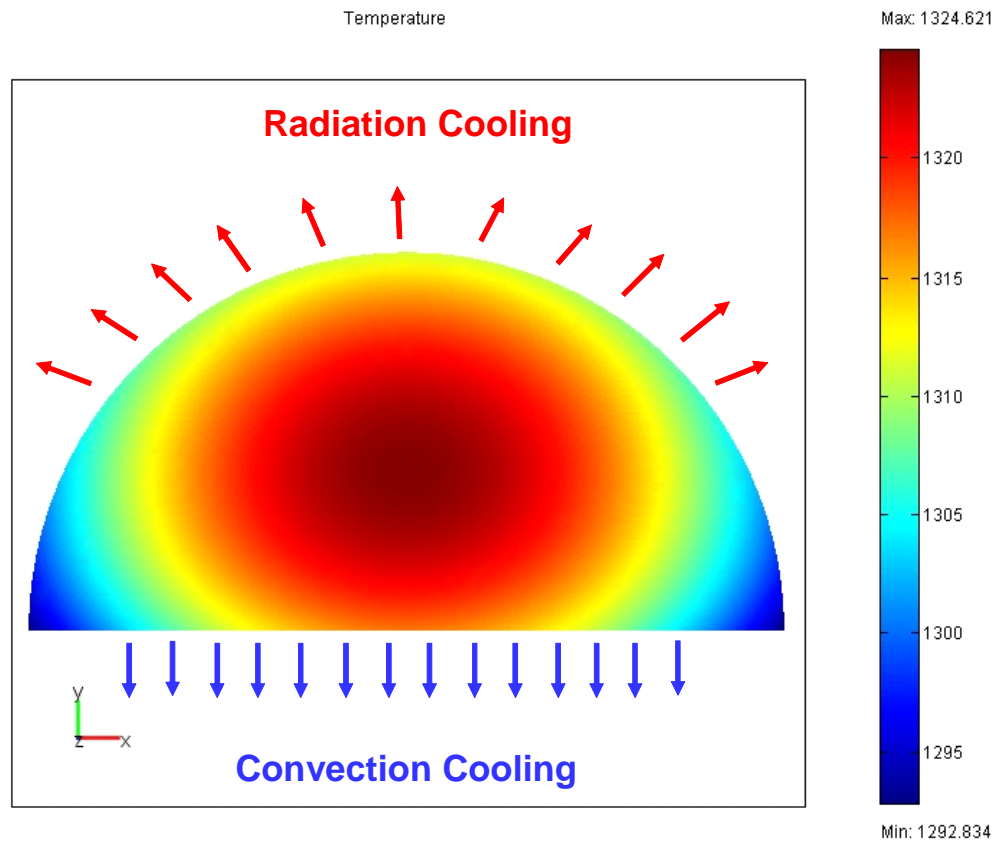


Fig. C.2 Temperature profile calculated by FEM around the dendrite forming temperature range: $1000^{\circ}\text{C} \sim 1050^{\circ}\text{C}$. (Here, temperature scale is given in Kelvin.) The modeling was done in collaboration with Marios Demetriou at Caltech [2].

As explained in Section 5.1.2, it was somewhat unexpected to observe the dendrite size becoming smaller going up to the top of the button, because it suggests the slowest cooling does not take place at the top surface during dendrite formation. The author had initially assumed a convective unidirectional cooling only from the bottom of the sample. However, Figs. 5.3-5.5 clearly show that the largest dendrites occur in the lower middle range. Another interesting observation is that the second phase in most regions shows an equiaxial shape. Although a more careful observation reveals locally elongated dendritic morphology mainly in the top and bottom areas, the overall trend illustrates isothermal cooling rather than a unidirectional one.

To interpret these counter-intuitive observations, Finite Element Modeling (by FEM Lab software) was employed, and it successfully described the real heat transfer conditions. Based on the previous knowledge on Vitreloy 1 and the cooling rate of the arc-melter, the overall convective heat transfer coefficient h_c , between water and molten button through Cu conduction, was determined to be around 100 W/(m²K) [2]. The data employed in this calculation includes the conductivity of the Cu plate and the thermal resistance between the Cu plate and water plus the thermal resistance between the Cu plate and the molten button as well.

Another important parameter is the cooling by radiation:

$$h_r = 4\varepsilon\sigma T^3 \quad (\text{C.1})$$

where, emissivity $\varepsilon = 0.3$ for Vit 1, Stefan-Boltzmann constant $\sigma = 5.67 \times 10^{-8}$ W/(m²K⁴),

$T = 1500$ K (liquidus of dendrite). Therefore,

$$h_r \approx 200 \text{ W/(m}^2\text{K)} \quad (\text{C.2})$$

$$h_c \approx 100 \text{ W/(m}^2\text{K)} \quad (\text{C.3})$$

The most important conclusion here is that cooling by radiation is as effective (if not more) as convective cooling at high temperatures. With these input data, the temperature profile was generated by 3-D FEM, and the result is shown in Fig. C.2. The starting temperature was 2000 K and Fig. C.2 exhibits the early stage of the cooling ($1000^{\circ}\text{C} \sim 1050^{\circ}\text{C}$) where dendrites are expected to form under heterogenous β phase nucleation condition. The solidus and liquidus for dendrites are estimated to be about 800°C and 1150°C , respectively, from the synchrotron *in-situ* heating experiments (see Section 5.3.) Materials parameters such as heat capacity are taken from Vitreloy 1 due to its compositional similarity with the amorphous matrix. The slowest cooling rate takes place in the middle range due to the fast cooling by radiation which it explains the bigger dendrite formation in the middle of the button. The fact that the largest dendrites were discovered a little lower than the exact center suggests that cooling by radiation was more effective than convective cooling at that temperature range. However, the temperature scale varies by only 20°C in most of the sampling volume, which means there is no significant temperature gradient inside the button. It was monitored in the FEM simulations that the whole button cooled down isothermally until the room temperature, even though a time specific profile such as that in Fig. C.2 reveals a small temperature gradient.

To further validate this modeling result, a scaling analysis was applied using the Biot number defined as:

$$\text{Bi} = \frac{h(V/A)}{k} = \frac{h R}{k 3} \quad (\text{C.4})$$

where, the overall heat transfer coefficient $h_{overall} \approx 100 \text{ W}/(\text{m}^2\text{K})$, thermal conductivity of Vit 1 $k_{vit1} = 18 \text{ W}/(\text{mK})$, mid-plane distance $R \approx 0.008 \text{ m}$. Therefore,

$$Bi \approx 0.02 \quad (\text{C.5})$$

Fig C.3 shows that a small Biot number (high k and low h) generates isothermal cooling since conduction within the solid is much faster than heat loss at the interface. The calculated Biot number $0.02 \ll 1$ confirms the isothermal cooling behavior predicted by the FEM modeling.

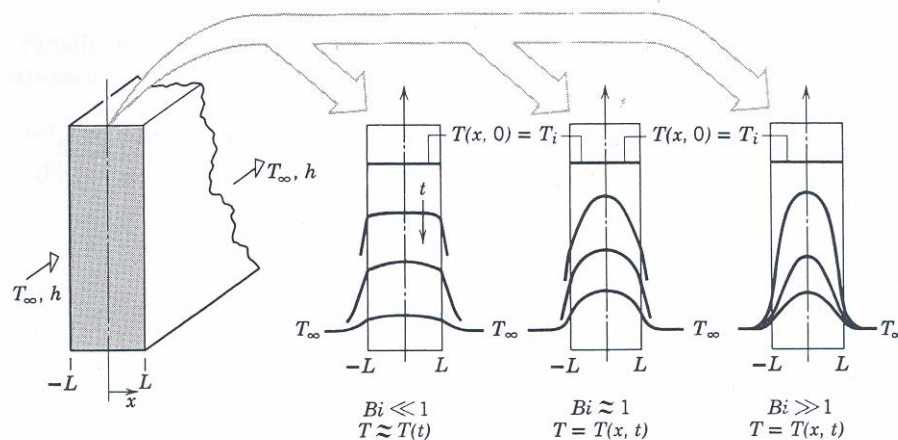


Fig. C.3 Transient temperature distribution for different Biot numbers in a plane wall symmetrically cooled by convection. Note that a small Biot number (high heat transfer rate inside the materials) induces isothermal cooling and a large Biot number (high heat transfer rate at the interface) causes significant temperature gradients within the solid. Reproduced from Frank P. Incropera and David P. De witt “Introduction to Heat Transfer” p. 231.

As shown above, the overall cooling rate does not change much within the button, while a large variation of the dendrite size should be driven by large differences in the cooling rate. One possible explanation of why the dendrite size varied much inside the

button while the temperature gradients are expected to be low would be the “recalescence”, i.e., the latent heat released during dendrite solidification. It has been known that recalescence events can lead to local temperature increases about 50~200°C [3-4]. In that case, this volumetric heat source cannot be ignored. Since the solidification process happens from the edge to the center, the continuous latent heat release process could induce a greater cooling rate difference by modifying the heat flux from the center to the surface. Unfortunately, the current state of the art in modeling is not sufficient to further quantify the exact temperature profile within the button during dendrite formation and growth.

In sum, it is concluded that the radiative cooling effect is quite significant around the dendrite forming period, and the whole button cools down mostly isothermally with a small temperature gradient. The observed big dendrite size distribution in spite of this expected small cooling rate difference suggests that dendrite formation is very sensitive to local heat transfer conditions, and additional temperature gradients may be added by the volumetric heat source which is generated through the solidification process.

References

- [1] S. Lee (2004). Unpublished research.
- [2] M. Demetriou (2004). Unpublished research on BMG heat transfer by finite element modeling.
- [3] S. Mukherjee (2005). Study of crystallization behavior, kinetics and thermodynamics of bulk metallic glasses using noncontact electrostatic levitation technique. Caltech Ph.D thesis.
- [4] M. Demetriou (2004). Unpublished research on recalescence by DSC.